Modeling and Simulation of Amorphous Materials

A dissertation presented to

the faculty of

the College of Arts and Sciences of Ohio University

In partial fulfillment

of the requirements for the degree

Doctor of Philosophy

Anup Pandey

April 2017

© 2017 Anup Pandey. All Rights Reserved.

This dissertation titled

Modeling and Simulation of Amorphous Materials

by

ANUP PANDEY

has been approved for

the Department of Physics and Astronomy

and the College of Arts and Sciences by

David A. Drabold

Distinguished Professor of Physics and Astronomy

Robert Frank

Dean, College of Arts and Sciences

Abstract

PANDEY, ANUP, Ph.D., April 2017, Physics and Astronomy

Modeling and Simulation of Amorphous Materials (129 pp.)

Director of Dissertation: David A. Drabold

The general and practical inversion of diffraction data – producing a computer model correctly representing the material explored – is an important unsolved problem for disordered materials. Such modeling should proceed by using our full knowledge base, both from experiment and theory. In this dissertation, we introduce a robust method, Force-Enhanced Atomic Refinement (FEAR), which jointly exploits the power of *ab initio* atomistic simulation along with the information carried by diffraction data. As a preliminary trial, the method has been implemented using empirical potentials for amorphous silicon (*a*-Si) and silica (SiO_2). The models obtained are comparable to the ones prepared by the conventional approaches as well as the experiments. Using *ab initio* interactions, the method is applied to two very different systems: amorphous silicon (*a*-Si) and two compositions of a solid electrolyte memory material silver-doped $GeSe_3$. It is shown that the method works well for both the materials. Besides that, the technique is easy to implement, is faster and yields results much improved over conventional simulation methods for the materials explored. It offers a means to add *a priori* information in first principles modeling of materials, and represents a significant step toward the computational design of non-crystalline materials using accurate interatomic interactions and experimental information. Moreover, the method has also been used to create a computer model of *a*-Si, using highly precise X-ray diffraction data. The model predicts properties that are close to the continuous random network models but with no *a priori* assumptions.

In addition, using the *ab initio* molecular dynamics simulations (AIMD) we explored the doping and transport in hydrogenated amorphous silicon *a*-Si:H with the most popular

impurities: boron and phosphorous. We investigated doping for these impurities and the role of H in the doping process. We revealed the network motion and H hopping induced by the thermal fluctuations significantly impacts conduction in this material. In the last section of the dissertation, we employed AIMD to model the structure of amorphous zinc oxide (a-ZnO) and trivalent elements (Al, Ga and In) doped a-ZnO. We studied the structure and electronic structure of these models as well as the effect of trivalent dopants in both the structure and electronic structure of a-ZnO.

To my parents, wife and entire family members.

ACKNOWLEDGMENTS

I would like to take a moment to thank everyone who has played an important role in a successful completion of my Ph.D.

Firstly, I would like to express deep gratitude to my advisor Prof. David A. Drabold. During this time, it was his overall guidance and support that helped me grow as a young researcher. It was his encouragement that helped me remain focused in my work. The knowledge and expertise that I have gained working under him will remain a valuable resource for the rest of my life.

I would like to thank our collaborator Prof. Parthapratim Biswas from the University of Southern Mississippi for his valuable suggestions in all the projects that we have done together. I would also like to thank Prof. Gang Chen for his helpful advice.

I thank my senior group members Dr. Binay Prasai and Dr. Yuing Li for their important suggestions. I would also like to thank my fellow group members and colleagues Kiran Prasai, Bishal Bhattarai, Dale Igram and Mayur Sundararajan for important discussions, comments and suggestions.

I would like to extend my acknowledgement to the Department of Physics and Astronomy, Ohio University, for providing me the opportunity to be a student and pursue my studies in this reputable institution. I would like to thank all the funding agencies for their financial support.

Finally, I would like to extend my gratitude to my family: my parents, my wife and my sisters who have always been on my side during this tough and long course of study. Without their constant support and encouragement it would have been impossible to achieve this goal.

Table of Contents

Page

Abstract 3

Dedication 5

Acknowledgments 6

List of Tables 10

List of Figures 11

1 Introduction 16
- 1.1 Background 16
- 1.2 Interatomic Interactions 19
  - 1.2.1 Empirical or Classical Interactions 19
  - 1.2.2 Quantum Mechanical Interactions 19
    - 1.2.2.1 Spanish Initiative for Electronic Simulations with Thousands of Atoms (SIESTA) 20
    - 1.2.2.2 Vienna Ab Initio Simulation Package (VASP) 20
- 1.3 Modelling Methods for Amorphous Materials 20
  - 1.3.1 Simulation Paradigm 21
  - 1.3.2 Information Paradigm 21
  - 1.3.3 Hybrid Scheme 21
- 1.4 Interpretation of Model Properties 21
  - 1.4.1 Electronic Properties 22
  - 1.4.2 Structural Properties 22
- 1.5 Amorphous Silicon (*a*-Si): The Major Material Under Study 24
- 1.6 Dissertation Outline 25

2 Electrical Activity of Boron and Phosphorous in Hydrogenated Amorphous Silicon 27
- 2.1 Introduction 27
- 2.2 Methodology and Models 28
- 2.3 Impurities on a Static Lattice 30
  - 2.3.1 Boron and Phosphorous Doped a-Si 32
  - 2.3.2 H Passivation in Hydrogenated B- and P-Doped a-Si 36
- 2.4 Dynamical Lattice 42
  - 2.4.1 Energy Gap and Kubo-Greenwood Formula 45
  - 2.4.2 Hydrogen Hopping and Coordination Number 47
- 2.5 Conclusion 50

3 Force-Enhanced Atomic Refinement (FEAR): Structural Modeling With Empirical Interactions in a Reverse Monte Carlo Approach 51
3.1 Introduction 51
3.2 Methodology: Basics of FEAR and Its Implementation 53
3.3 Results and Discussion 58
3.3.1 Amorphous Silica (a-SiO_2) 58
3.3.2 Modeling Amorphous Silicon (a-Si) 65
3.4 Conclusion 68

4 Inversion of Diffraction Data for Amorphous Materials 70
4.1 Background and Introduction 70
4.2 Methodology 72
4.2.1 *Ab Initio* Force-Enhanced Atomic Refinement (AIFEAR) 72
4.2.2 Amorphous Silicon (a-Si) 73
4.2.3 Chalcogenide Glasses: $(GeSe_3)_{1-x}Ag_x$ [x=0.05 and 0.077]) 73
4.3 Application of AIFEAR 74
4.3.0.1 Amorphous Silicon (a-Si) 74
4.3.0.2 Chalcogenide Glasses: $(GeSe_3)_{1-x}Ag_x$ [x=0.050 and 0.077]) 78
4.4 Conclusion 82

5 Realistic Inversion of Diffraction Data for an Amorphous Solid: The Case of Amorphous Silicon 84
5.1 Introduction 84
5.2 Methodology 86
5.3 Results and Discussion 88
5.3.1 Structural Analysis 89
5.3.2 Fluctuations in FEAR 92
5.3.3 Electronic Structure 94
5.3.4 Vibrational Properties 95
5.4 Conclusion 97

6 Density Functional Model of Amorphous Zinc Oxide (a-ZnO) and Aluminium (Al), Gallium (Ga) and Indium (In) Doped a-ZnO 99
6.1 Introduction 99
6.2 Computational Methods 100
6.3 Results and Discussion 101
6.3.1 Amorphous Zinc Oxide (a-ZnO) 102
6.3.2 Al-, Ga- and In-doped Amorphous ZnO: a-$X_{0.375}Z_{0.625}O$ (X= Al, Ga and In) 104
6.4 Conclusion 108

7 Conclusion and Future Work 109
7.1 Future Work 110

Appendix: A Brief Description on How to Use FEAR 128

List of Tables

Table Page

2.1 Static Boron Configurations. 34
2.2 Static Phosphorous Configurations. 35

3.1 Number of Force Calls and Average CPU Time in FEAR Compared With Classical and Quantum Melt-Quench Method [80, 81]. 61
3.2 Peak Positions of FEAR Model Compared With Other MD Models and Experiments (Expt.). 62
3.3 Bond-Angle Distributions From FEAR, MD and DR Models. 63
3.4 Ring Statistics of *a*-SiO_2 From FEAR Models. 64

4.1 Total Energy and Key Structural Properties of *a*-Si Models. The Energy per Atom is Expressed With Reference to the Energy of the WWW Model. 78

5.1 Total Energy and Key Structural Properties of *a*-Si Models. The Energy per Atom is Expressed With Reference to the Energy of the WWW Model. 90

6.1 Coordination Number for Zn and O Expressed in Percentage, Average Coordination Number and the DFT-GGA Energy for a-ZnO Model. The Coordination Numbers for Zn are Compared With the Other MD Model [132]. As Expected There Are a Few More Coordination Defects in the More Rapidly Quenched Model 2. 103
6.2 First Peak Position for Zn-Zn, Zn-O and O-O Partial Pair Correlation Functions of a-ZnO (Model 1) and a-$X_{0.375}Z_{0.625}O$ (X= Al, Ga and In) Models. 106

List of Figures

Figure | Page

2.1 Electronic density of states (EDOS) with Fermi level at 0 eV. Green represents the EDOS for 64-atom *a*-Si and blue is the EDOS for 70-atom *a*-Si:H. 29

2.2 Boron doped *a*-Si with various impurity concentrations. Models (1), (2), (4) and (7) are 1.6%, 3.1%, 7.8% and 12.5% B doped *a*-Si respectively with each B having configuration B(4Si) [four Si neighbors to B]. In models (3) and (5), B dimers are formed with configuration B(3Si,1B). Model (6) consists of B4 cluster with configuration B(1Si,3B). Details of these models are provided in Table I. The Fermi energy is at 0 eV for each curve in the figure. 30

2.3 Phosphorous doped *a*-Si with different impurity concentrations. Models (1), (2), (5) and (8) are 1.6%, 3.1%, 7.8% and 12.5% B doped *a*-Si respectively with each P having configuration P(4Si) . In models (3) and (7) P dimers are formed with configuration P(3Si,1P) and model (6) consists of P4 cluster denoted by P(1Si,3P). P is three-fold in configuration (4) with configuration P(3Si). Details of these models are provided in Table II. The Fermi energy is at 0 eV for all the EDOS in the figure. 31

2.4 H passivation in B doped *a*-Si.(a) H bonds with B forming metastable B(4Si,1H) structure, (b) Relaxation breaks a Si-B bond forming B(3Si,1H) and a Si DB, (c) Another H passivates the Si DB.(Dark Blue=Si; Light Blue=B; White=H). 31

2.5 Comparison of EDOS for different configurations in H passivation for B-doped *a*-Si. Green denotes the EDOS of B bonded with 3Si and 1H without Si dangling bond which is doped configuration. Red is the EDOS of B bonded with 3Si and 1H with Si dangling bond and is undoped configuration with a defect state in gap. The Fermi level is shifted to 0 eV in all the EDOS. 38

2.6 Bond center H forming structures B-Si-H-Si (top) and B-Si-Si-H-Si (bottom).(Dark Blue=Si; Light Blue=B; White=H) 39

2.7 (Blue left) EDOS for B-Si-H-Si BC structure after relaxation which is undoped. (blue right) EDOS for B-Si-Si-H-Si BC structure after relaxation which is undoped. Green is the EDOS of B-doped *a*-Si and is doped configuration. The Fermi level is shifted to 0 eV in all the EDOS. 39

2.8 H passivation in P doped *a*-Si.(a) H bonds with P forming metastable P(4Si,1H) structure, (b) Relaxation breaks a Si-P bond forming P(3Si,1H) and a Si DB, (c) Another H passivates the Si DB.(Dark Blue=Si; Green=P; White=H). . . . 40

2.9 Comparison of EDOS for different configurations in H passivation for P-doped *a*-Si. Blue is the EDOS of the final configuration in which P bonds with 3Si and 1H atoms with Si dangling bond. Red is the EDOS of the final configuration in which P bonds with 3Si and 1H without Si dangling bond. The Fermi energy is shifted to 0 eV in all the EDOS. 40

2.10 H passivation in P doped *a*-Si. (left) Top panel forming P-H-Si and bottom panel forming P-Si-H-Si structure. (right) After relaxation, P forms 3-fold bond nad H passivates Si DB producing non-doping configuration. (Blue=Si; Green=P; White=H) 42
2.11 EDOS for two H passivation case. (left) Initial P-H-Si structure after relaxation forms P(3Si) and Si(3Si,1H), (right) Initial P-Si-H-Si structure after relaxation forms P(3Si) and Si(3Si,1H). The Fermi level is shifted to 0 eV in all the EDOS. 43
2.12 Plot of highest three valence band and lowest three conduction band energy levels. (a) For B-doped and hydrogenated B-doped *a*-Si at 600 K, (b) for P-doped and hydrogenated *a*-Si at 600 K.(Green) HOMO level (Blue) LUMO level. Proximity of Green and Blue levels implies conduction is possible (the HOMO-LUMO gap is small). 44
2.13 Distance between Hydrogen and impurites (a)B-doped hydrogenated *a*-Si (b)P-doped hydrogenated *a*-Si. (Red=300 K; Green=600 K; Blue=800 K) . . . 46
2.14 Hydrogen hopping between bond centers and passivating the Si dangling bonds in hydrogenated B doped *a*-Si DB at various snapshot for 600 K thermal MD. . 47
2.15 (Lower half) Hydrogen coordination fluctuation (Upper half) enery-gap fluctuation (a)B-doped hydrogenated *a*-Si (b)P-doped hydrogenated *a*-Si. Zero coordination means H is in process of hopping. 48

3.1 A schematic diagram of the FEAR method. The principal computing loop is highlighted in grey. 53
3.2 Scaling of total CPU time (red circles) vs. system size in FEAR simulations. A least-square fit of the data with a quadratic polynomial is shown as a blue curve. 57
3.3 Partial pair-correlation data for *a*-SiO_2 models from FEAR simulations. The corresponding data (dashed blue curve) for a DR model from [85] are included for comparison. 58
3.4 Calculated total neutron static structure factor for 648- and 1536-atom *a*-SiO_2 models from FEAR simulations. Experimental data from [79] are shown as solid circles. 59
3.5 Total energy (of *a*-SiO_2) and the cost function χ^2 vs. RMC steps during FEAR simulations. The horizontal line corresponds to the energy of a DR model using the BKS potential for comparison. 59
3.6 Bond-angle distributions of a 1536-atom model of *a*-SiO_2 from FEAR calculations. The average and width of the distributions are listed in Table III. 60
3.7 Electronic density of states (EDOS) for a 192-atom model of *a*-SiO_2 obtained from FEAR simulations. The corresponding result from a DR model is included for a comparison. Fermi levels are indicated as vertical lines at 2.4 eV (DR) and 3.4 eV (FEAR). 60
3.8 A comparison of FEAR structure factor for a 216-atom model of *a*-Si with the experimental data from Ref. [32]. 65

3.9 Pair-correlation data (blue) for a 216-atom model of *a*-Si obtained from FEAR. The corresponding data (red) for a WWW model is also presented here for a comparison. 66
3.10 The variation of χ^2 and EDIP energy during FEAR simulations. The dashed line is the EDIP energy for a WWW model with an identical size and the number density. 66
3.11 (a) The bond-angle distribution for a 216-atom model of *a*-Si using FEAR (solid line) and a WWW model (dashed line). (b) The bond-angle distribution for a 216-atom '*a*-Si model' from RMC simulations using experimental structure factor only. The approximate semi-circular distribution is a characteristic feature of *unconstrained* RMC. 67
3.12 Density of electronic states of *a*-Si using VASP from FEAR (blue) and WWW (red) models. The corresponding Fermi levels are indicated as vertical lines at 6.1 eV (FEAR) and 5.7 eV (WWW). 67

4.1 Top: A 216-atom model of *a*-Si obtained from (a) RMC, (b) melt-quench and (c) *ab initio* FEAR simulations. Silicon atoms with a coordination number of 3, 4 and 5 are shown in green, blue and red colors, respectively. Center: The radial distribution function (RDF) for the (d) RMC, (e) melt-quench and (f) *ab initio* FEAR models. Bottom: The bond-angle distributions for the models as indicated in the figure. For animations showing the formation of three-dimensional network structure and the corresponding evolution of the radial and coordination-number distributions follow the youtube links provided in the application section. 75
4.2 Results for 216-atom *a*-Si: (a) The variation of cost function and total energy with the number of AIFEAR steps. (b) Electronic density of states (EDOS) for RMC, melt-quench and AIFEAR models with the Fermi level at 0 eV. (c) The bond-angle distribution from AIFEAR compared to that of WWW (see Table 1 for details). 76
4.3 The evolution of four-fold Si atoms during FEAR simulation for three different combinations of the number of accepted moves (M) and number of CG steps (N). (black) M=1000 and N=5, (red) M=1000 and N=20 and (green) M=6000 and N=5. 77
4.4 (a) Structure factors of $(GeSe_3)_{1-x}Ag_x$ [x=0.05] from *ab initio* FEAR. Experimental data, from neutron diffraction measurements, are shown for comparison [103]. Melt-quench data are from Pradel *et al.*[103] (b) The radial distribution function of $(GeSe_3)_{1-x}Ag_x$ [x=0.077] from *ab initio* FEAR and melt-quench simulations. Experimental RDF shown here are from Zeidler *et al.* [104]. 80
4.5 Total energy per atom and the cost function (χ^2) versus AIFEAR steps for two models with (a) 5% and (b) 7.7% Ag-doped $GeSe_3$. The melt-quench energy for the 7.7% Ag model is indicated for comparison. 81

4.6 Comparison of number of force calls in *ab initio* FEAR with melt-quench simulations for *a*-Si, and 5% and 7.7% Ag-doped $GeSe_3$. Note that the number of force calls in melt-quench simulations vary considerably for different systems. 82

5.1 Comparison of the simulated X-ray static structure factor (black) from FEAR with the experimental diffraction data (red circle) from Ref. [32]. A 216-atom model is used to produced the simulated structure factor. 87
5.2 The reduced pair-correlation function of *a*-Si obtained from a 216-atom model using FEAR (black) and WWW (blue) methods. The experimental data (red) shown above are the Fourier transform of the high-energy X-ray diffraction data from Ref. [32]. 87
5.3 The number of *n*-fold ring per atom (R_C) for the FEAR model (blue) compared to the WWW model of same size. 88
5.4 Total energy per atom and χ^2 versus FEAR steps for a 216-atom *a*-Si model. The green and black broken lines represent the energy per atom for the CG-only and WWW model, respectively. 92
5.5 Variation of the average coordination number for the final 500 steps of FEAR using two different input RDF data. The upper panel is for high-energy X-ray diffraction data from Laaziri *et al.* [32] and the lower panel is for the WWW radial distribution function (RDF) as an input data [116]. The broken horizontal line, in the upper panel, represents the average coordination number, 3.88, reported by Laaziri *et. al.* [32] 92
5.6 Variation of the highest occupied molecular orbital (HOMO)level and the lowest unoccupied molecular orbital (LUMO) level for the final 500 steps of FEAR. Note the annihilation of an electronic (gap state) defect near 600 steps. 93
5.7 Electronic density of states (EDOS) of *a*-Si obtained from FEAR (red), CG-only (green) and pure RMC (blue) models. The Fermi levels are located at 0 eV. 95
5.8 Inverse participation ratio (IPR) of 216-atom *a*-Si model for FEAR (black) and RMC (red) models near the gap. Fermi levels are shown by arrows of respective colors. 95
5.9 Vibrational density of states of *a*-Si, $g(\omega)$, from a 216-atom FEAR model (blue). The experimental vdos (red) obtained from Kamitakahara et al. [127] . 96
5.10 The specific heat capacity (C_V/T^3) for 216-atom *a*-Si FEAR model (black) compared to the experiment [130]. The inset shows the "Dulong-Petit" limit at higher temperature. 97

6.1 The total radial distribution function (RDF) for four a-ZnO models. Model 1 and Model 2 corresponds to the models obtained by two different quenching rates as described in the method section. Blue is for Model 1 and green is for Model 2. 100

6.2 Partial pair correlation functions for 128-atom models of a-ZnO. Blue is for Model 1 and red is for Model 2 as described in the method section. 102
6.3 (black) Electronic density of states of the 128-atom model a-ZnO (Model I) obtained using GGA-PBE density functional theory calculation. The green vertical lines represent the inverse participation ratio (IPR) used to measure the electronic state localization. Longer IPR implies strong localization. The Fermi level is at 0.28 eV. The PBE gap is 1.36 eV. 104
6.4 (a) Total pair correlation functions for 128-atom $In_{0.375}Z_{0.625}O$ model. (b) Partial pair correlation function of $In_{0.375}Z_{0.625}O$ model. 105
6.5 Electronic density of states for a-$X_{0.375}Z_{0.625}O$ (X= Al, Ga and In) models compared to that of a-ZnO. The Fermi levels are shown by vertical broken lines. 106

1 INTRODUCTION

1.1 Background

The study of materials through computer modeling has a pivotal role in modern day materials research. Like experimental devices, high-performance computers are considered as a complementary tool to the experiments in the study of material properties. In a study of complex materials, such as amorphous solids that have no long-range crystalline order, it is difficult to probe the structure by experiments alone. In such a case, computer models have proven to be a major contributor to revealing the local structure of amorphous materials.

The discovery of Bragg diffraction in the early 1900's has solved most of the problems pertaining to the crystal structure [1]. By exposing crystalline solids to X-rays and analyzing the diffraction peaks, the exact structure of crystals could be ascertained. The method is commonly known as 'X-ray Crystallography' and has been one of the profound success stories of science, even revealing the structure of proteins [2]. The situation is different for the non-crystalline materials. The absence of sharp peaks and the smooth structure factors of these materials are due to the presence of local ordering at varying length scales and no long range order. This one-dimensional structure factor is by itself, insufficient to dictate the correct three-dimensional structure of amorphous materials. Consequently, the development of new tools is essential in solving the structure of these materials.

A successful theoretical representation of amorphous materials is the *continuous random network* (CRN) proposed by Zachariasen in 1932 [3]. Each atom in the CRN is perfectly coordinated without any defects or voids, and the long range order is completely absent (no periodicity). Initial models of CRN were hand-made from metals and glasses [4, 5]. Although the first computer model of CRN was introduced by Guttman in

1980 [6], it had a scaling problem with a model size limited to only 60 atoms. In 1985, a simple bond-switching Monte Carlo algorithm was introduced by Wooten, Winer and Weaire that could model the CRN for an amorphous column IV semiconductor and is commonly known as 'WWW method' [7].

High quality tetrahedral networks of amorphous silicon and germanium were produced by the WWW method. The method was later applied to binary glasses by Mousseau and Barkema [8]. The original version of WWW method consisted a diamond starting configuration (crystal) which is then subjected to specified Monte Carlo moves related to bond switching. For any two bonded atoms P and Q, two neighbors X and Y of P and Q are chosen, respectively (X is not a neighbor of Q and Y is not a neighbor of P). Then the bonds P-X and Q-Y are broken (removed from the bond list of P and Q) and switched such that Y bonds to P and X bonds to Q, thereby exchanging the neighbors (added to the bond list of P and Q). This process maintains the four-fold coordination while introducing five- and seven-fold rings in a network, a characteristic feature of CRN. The Monte Carlo moves are accepted or rejected under the Metropolis scheme using a Keating potential (simple harmonic springs), which very crudely describes the interatomic interactions. The method has been modified for non crystalline starting configurations [9]. The WWW models are still considered to be the best models with lowest strain and bond distortions for *a*-Si.

The success of the WWW method is mainly due to two reasons. Firstly, it is a highly constrained method with the system being forced to remain four-fold coordinated and the bond-angle pushed towards θ_T=109.47°. Secondly, the bond-switching moves compliment these constraints. The method is *ad hoc*, in a sense that it uses constraints based on *a priori* experimental information and a Keating potential. This makes it limited only to a handful of systems.

Beginning in the mid-eighties, molecular dynamics (MD) simulations using empirical potentials [10] and *ab initio* interactions [11] were carried out in generating disordered structures by quenching a melted crystal structure. This method is commonly known as 'melt-quench' or 'cook and quench'. Although the 'melt-quench' method was successful in generating some glassy structures, it proved to be inadequate for amorphous materials with no or weak glass forming ability.

Contemporary with these computations, an alternative approach to invert experimental diffraction data, called reverse Monte Carlo (RMC), was introduced by McGreevy and Pusztai [12]. It was quickly discovered that RMC without any *a priori* information is inadequate to generate chemically realistic structures. The search continues for a robust method that could address the deficiencies associated with the modeling of amorphous materials.

Besides DFT simulation of amorphous materials, such as hydrogenated *a*-Si and amorphous zinc oxide, the focus of this thesis is a newly developed technique called force-enhanced atomic refinement (FEAR) that mutually exploits the power of *ab initio* atomistic simulation along with the information carried by diffraction data. The method is discussed in Chapter 3 and 4. As mentioned above, it is important to realize that the simulation-based approaches failed to reproduce the real process of material formation and have a serious size limitation. The data-driven approaches alone are unable to address the correct chemistry and incorporating constraints make the method *ad hoc*. Most of these deficiencies are tackled by FEAR. The *ab initio* interactions in FEAR dictate the correct local chemistry and the inversion of diffraction data help to explore the region of configuration space consistent with the data. Also, the partial use of relaxation and data inversion steps make the method computationally efficient. The efficacy of this new approach is illustrated by applying it to both poor and excellent glass forming materials. The method has been successful in generating amorphous structures which are close to the

CRN without using any *a priori* information in the modeling process. This opens up an avenue in the modeling of amorphous materials and provides a completely different rationale for CRN models.

1.2 Interatomic Interactions

The chemical interactions between the elements constituting the material is vital for obtaining a realistic model. These interactions can be broadly divided into the following groups.

1.2.1 Empirical or Classical Interactions

The classical or empirical interactions are phenomenological representations of energetics. These interactions may involve bond stretching, bond-bending, dihedral angle forces etc. and may include non-bonding terms: the electrostatic interactions, van der Waals interactions etc.

These potentials have a transferability problem but may be reliable in the study of the properties of those structures which were used to fit the potential. For disordered materials, it is difficult to predict the correct empirical potential because of the complex local structure in varying length scale. The method based on empirical potentials are computationally cheap and can be used in modelling larger systems.

1.2.2 Quantum Mechanical Interactions

The quantum interactions in a many body systems consist of the kinetic energy of each electron and nucleus, the interaction energy between each electron and the collection of atomic nuclei and the interaction energy between different electrons and the interactions between different nuclei. This determines the many-body Schrdinger equation.

After decoupling the nuclear degrees of freedom, the Schrodinger equation with many-electron wavefunctions (which is the function of 3N electronic coordinates for N

electrons system) is prohibitively complex. This problem was simplified by Kohn, Hohenberg and Sham [13, 14] by considering the electronic ground state energy of a many-electron systems as a functional of electron density $n(\mathbf{r})$. The approach is commonly known as the density functional theory (DFT). The detail of DFT can be found elsewhere [15].

The following two DFT packages are used to calculate the total energies, forces and electronic structures in the current work.

1.2.2.1 Spanish Initiative for Electronic Simulations with Thousands of Atoms (SIESTA)

SIESTA is a package used to carry out *ab initio* molecular dynamics simulations and electronic structure calculations of molecules and solids [16]. It uses the self-consistent Kohn-Sham (KS) [14] density functional method within the local density approximation (LDA) and generalised gradient approximation (GGA). The basis sets used are pseudo-atomic orbitals. The core electrons are addressed using norm-conserving pseudopotentials.

1.2.2.2 Vienna Ab Initio Simulation Package (VASP)

VASP is an another package to carry out *ab initio* quantum mechanical molecular dynamics simulations [17]. It solves the self-consistent KS equation using a plane wave basis. The electron-nuclei interactions are described by ultra-soft pseudopotentials [18] or by projector-augmented wave (PAW) [19] method. It can be implemented under LDA [20], GGA [21] and hybrid approaches [142].

1.3 Modelling Methods for Amorphous Materials

The computational methods can be broadly classified into following three groups.

1.3.1 Simulation Paradigm

The term was first coined by Drabold [23] and comprise traditional molecular dynamics (MD) or Monte Carlo (MC) techniques using some kind of interactions. The interactions can be both empirical (e.g. classical MD) or quantum mechanical (e.g. DFT-MD). The well known technique 'melt-quench' to model glassy and amorphous materials, where the system is melted at high temperature and then quenched to the desired temperature, falls under this category.

1.3.2 Information Paradigm

The term was again coined by Drabold [23] and consists of those methods that invert the experimental data (for example, produces a structural model)from the structure factor or pair correlation function, without any interactions. The structural model obtained by this method agrees well with the input *a priori* experimental information. The reverse Monte Carlo (RMC) [12] is an archetypal example of information paradigm.

1.3.3 Hybrid Scheme

The methods that fall under this group use both experimental data inversion and interactions. The interactions could be empirical or quantum mechanical. The techniques such as hybrid reverse Monte Carlo (HRMC) [24] is an example of the hybrid scheme using the empirical potential whereas the experimentally constrained molecular relaxation (ECMR) [25] is an example using the *ab initio* interactions. This is discussed in detail in Chapter 3 and 4.

1.4 Interpretation of Model Properties

The methods to analyse electronic and structural properties are presented briefly in this section.

1.4.1 Electronic Properties

The electronic properties or electronic structure of a model is analyzed by calculating the electronic density of states (EDOS). It is the number of single-particle states in a given energy range and can be written as [15]:

$$\rho_{EDOS}(E) = \frac{1}{N_f} \sum_{i=1}^{N_f} \delta(E - \varepsilon_i), \tag{1.1}$$

where N_f is the total number of occupied electronic states and ε_i is the energy eigenvalue of the electronic Hamiltonian. The information about an electronic gap and gap states are provided by the EDOS, which is an essential feature in understanding electron conduction in a material.

Structural disorder and defects lead to spatially localized electronic states near the band tail and band gap. The electronic localizations are measured by calculating the inverse participation ration (IPR), denoted by I, and is given by:

$$I(\psi_j) = \frac{\sum_{i=1}^{N} a_i^{j4}}{(\sum_{i=1}^{N} a_i^{j2})^2}, \tag{1.2}$$

where N is the number of atoms in a given system, and a_i^j are the components of the jth eigenvector ψ_j projected onto atomic s,p and d states. For highly localized states, $I \sim 1$ and for extended states, $I \sim 1/N$.

1.4.2 Structural Properties

The structure of amorphous materials dictates its properties. It is essential to obtain a representative model of the material to study other properties, such as electronic structure, vibrational properties, etc. Experimentally, the structures are probed by the neutrons or X-ray diffraction experiments in the form of a smooth function in reciprocal space known as the structure factor *S(q)*. Fourier transform of a structure factor gives another function

known as the radial distribution function (RDF) in real space and is denoted by *g(r)*. A brief description of these functions and their connection to the neutron or X-ray scattering function is presented below.

The number of atoms of type β in the spherical shell of radius r and thickness dr from the center atom α is given as [26, 27]:

$$dn_{\alpha\beta} = 4\pi r^2 \rho_\beta g_{\alpha\beta} dr, \tag{1.3}$$

where $\rho_\beta = N_\beta/V$ is the number of atoms of type β per unit volume. The $g_{\alpha\beta}$ is known as the partial radial distribution function or partial pair distribution function. It has a limiting behavior of $g_{\alpha\beta}(r \to 0) = 0$ and $g_{\alpha\beta}(r \to \infty) = 1$. The overall PDF is defined as [26, 27]:

$$G(r) = \sum_{\alpha,\beta} c_\alpha c_\beta b_\alpha b_\beta (g_{\alpha\beta}(r) - 1), \tag{1.4}$$

where $c_\alpha = N_\alpha/N$ is the number concentration and b_α is the scattering factor of atom type α. *G(r)* and the scattering function is given by:

$$i(q) = \rho \int_0^\infty 4\pi r^2 G(r) \frac{sinqr}{qr} dr = F(q), \tag{1.5}$$

and

$$G(r) = \frac{1}{2\pi\rho} \int_0^\infty 4\pi q^2 i(q) \frac{sinqr}{qr} dq \tag{1.6}$$

Then, the structure factor can be written as:

$$S(q) = i(q) + \left(\sum_\alpha c_\alpha c_\beta \right)^2 \tag{1.7}$$

which can be normalized to get:

$$S_{norm}(q) = 1 + \frac{i(q)}{\left(\sum_\alpha c_\alpha c_\beta \right)^2} \tag{1.8}$$

Finally, in terms of the total radial distribution function the structure factor can be written in simplified form as:

$$S_{norm}(q) = 1 + \int_0^\infty drr^2 \frac{sinqr}{qr}(g(r) - 1), \tag{1.9}$$

where $g(r)$ is given by:

$$g(r) = \frac{\sum_{\alpha,\beta} c_\alpha c_\beta b_\alpha b_\beta g_{\alpha\beta}(r)}{\left(\sum_\alpha c_\alpha c_\beta\right)^2}. \tag{1.10}$$

The RDF provides much information about the structure. The first peak position gives the nearest neighbor distance and the area under the first peak gives the average coordination number of the atom.

The structural properties are investigated using an open source analysis program I.S.A.A.C.S. [26].

1.5 Amorphous Silicon (*a*-Si): The Major Material Under Study

The technological importance and complexity of *a*-Si make it a superior example in a study of amorphous materials. The use of *a*-Si in microelectronics, thin-film transistors and photo-voltaic (PV) applications [28] has led to many studies in recent decades [29–34]. In a similar context, the effects of *n*-type and *p*-type dopants: boron and phosphorous in hydrogenated *a*-Si was studied using *ab initio* MD simulations. We explored the significant role played by dopants in the electrical activity of hydrogenated *a*-Si.

In addition, the over-constrained network makes the structure of *a*-Si difficult to model [7, 35]. The only method that produces really satisfactory models for *a*-Si is the Wooten-Weaire-Winer (WWW) [7] scheme, which is limited by unrealistic interactions and is also not a general technique. Also, there has been numerous attempts in modelling *a*-Si by MD 'melt-quench' techniques using both empirical and *ab initio*

interactions [10, 11]. However, these models have higher defect concentrations and are unable to address many experimentally observed features of *a*-Si. The direct inversion of experimental data also fails to produce the correct network structure. This has made *a*-Si persistently vexing problem in modelling. We have been successful in generating a realistic model of *a*-Si using our method FEAR, which has very few defects and can be considered very close to the CRN.

1.6 Dissertation Outline

By the aid of computer generated models, we have studied the properties of various amorphous materials. The density functional theory (DFT) simulations are used in the study of doping effects in hydrogenated amorphous silicon and preparing amorphous zinc oxide models. A novel modeling technique FEAR is introduced and its application to various amorphous materials are reported.

In Chapter 2, we present a detailed static and dynamical study of *n*- and *p*-type dopants such as Boron and Phosphorous in hydrogenated amorphous silicon *a*-Si:H by using the EDOS and electronic eigenstates fluctuations. We also investigated the role of hydrogen in a doped model.

In Chapter 3, we introduce a new method of modeling amorphous materials using the *empirical* potentials called force-enhanced atomic refinement (FEAR). As a preliminary implementation, the method is used to model two archetypal glass forming and non-glass forming materials, *a*-SiO_2 and *a*-Si respectively.

In Chapter 4, we report an upgrade in the FEAR method. The method is successfully implemented with *ab initio* or quantum mechanical interactions, which makes it general and flexible. The method is applied to model *a*-Si and complex ternary chalcogenide glasses, silver-doped germanium selenide ($GeSe_3$), with 5% and 7.7% silver concentrations. The structure of *a*-Si is improved significantly by the use of quantum

mechanical interactions and the WWW model pair-correlation function as an experimental data. The Ag-doped $GeSe_3$ models capture all the significant features of experimental structure factor, as well as successfully predicts other properties that are not incorporated in the modeling process. This opens up a new avenue in the modeling of disorder materials. The implementation of FEAR algorithm with *ab initio* interactions can be found in the Appendix.

In Chapter 5, as a slightly different application of FEAR, we investigated the realistic structure of amorphous silicon using high precision X-ray diffraction data and *ab initio* interactions. The FEAR model compares well with most of the experimentally observed features. It is, so far, the best *a*-Si model obtained by using the realistic interactions and compares well with the experimental structure factor.

In Chapter 6, amorphous zinc oxide (a-ZnO) and a-ZnO doped with trivalent elements (Al, Ga and In) models are prepared using the DFT simulations and by the 'Melt-quench' method. The network topology is investigated in detail for all the models and the electronic density of states are calculated. The effect of dopants in electronic structure are also reported.

2 Electrical Activity of Boron and Phosphorous in Hydrogenated Amorphous Silicon

The work presented in this chapter is published in **Pandey, A., Cai, B., Podraza, N., and Drabold, D. A. (2014). Electrical Activity of Boron and Phosphorus in Hydrogenated Amorphous Silicon.** *Physical Review Applied, 2*(**5**), **054005.**.

2.1 Introduction

Doping of semiconducting materials is the basis of all electronic or optoelectronic applications (such as microbolometers for IR imaging[36], thin film transistors for display control[28] and photovoltaic applications[28]). The experimental discovery that amorphous silicon hydride (a-Si:H) could be doped with Boron (p-type) and Phosphorous (n-type) was due to Spear and Lecomber in 1975[37], and opened the door to the applications listed above. A great deal of experimental work has been carried out on doped a-Si:H, including NMR experiments[43] that gave valuable clues about the doping process.

The topological and chemical disorder of the a-Si:H structure creates a myriad of possible configurations, with highly variable electronic signatures. The angular strains, bond length strains, H nearby in one of various doping sites etc. make the doping phenomenon complicated. Also the thermally-induced variation in the coordinates of the atoms in the a-Si matrix has many consequences. The picture of small oscillations and phonons needs to be carefully considered for topologically disordered systems[39]. It turns out that the electronic response from these fluctuations is very strong, most particularly around the optical gap, where electron states are localized[41]. From the Kubo formula, it is evident that these are also the states that play a critical role in transport. H also plays an essential role. No material of electronic utility is without H. H

is highly mobile at temperatures above room temperature[42], and as it hops its electrical activity can change, and thus it can also impact doping.

To summarize our work, we report a wide range of accessible configurations using accurate molecular dynamics calculations. We detail the strain effects that arise from placing P and B in realistic models of a-Si:H. We show that B is intrinsically highly strained, and P is far more ”substitutional”. We prove with current techniques that the old conjecture of Boyce and Ready[43] that H passivation is indeed a key reason for low doping efficiency, also discussed earlier by Fedders and Drabold[44] and by Cai and Drabold[45]. We show that the results are reproducible, similar results accrue for impurities substituted into similar sites. By starting with the Kubo-Greenwood formula, we show that the dynamics of the lattice and the H play an essential role, at least at higher temperatures (say 300K and above). We show that the under certain circumstances, conductivity is strongly enhanced by transient doping conformations.

The present work offers a partial treatment of the role of dynamics, primarily serving notice that the motion of the lattice as well as H hopping is important to understanding doping. We show that H is attracted to B sites, in response to strained bonds that occur there. Clearly this increases the probability for H occupying the neighborhood of B atoms, though we have not quantified this effect. Since we show that H passivates doping, this provides a qualitative explanation for the low doping efficiency of B in Si.

2.2 Methodology and Models

In our simulations, we have employed the Vienna *ab initio* Simulation Package (VASP), a quantum mechanical molecular dynamics package using a plane wave basis set and the local density approximation (LDA)[17]. The electron-ion interactions were described using the projector augmented-wave (PAW) method[19]. A 64-atom amorphous silicon cubic cell of side 10.854Å, generated by Barkema and Mousseau[51], then

annealed and relaxed by us, was used as a starting model for the calculations. Boron (B) and Phosphorous (P) atoms were introduced on a various tetrahedral Si sites in the network and then relaxed at constant volume using conjugate gradient method. Models were fabricated with concentrations 1.6%, 3.1%, 7.8% and 12.5% of B and P for a static study of doping. Hydrogen passivation in B- and P-doped systems was studied by introducing H atoms at various sites in the 1.6% B- and P-doped a-Si models. One calculation is carried out on a 216-atom model made by the same group[51].

Dynamical simulation was carried out on 3.2% B and P doped a-Si models and H atoms were introduced in bond centers (BC) at varying distances from the impurities. The data presented here is for 80 ps time evolution with a time step of 2 fs. For selected cases, we doubled this time to verify our results. These times are adequate to reveal important thermal processes, though not to offer a full sampling of the phase space.

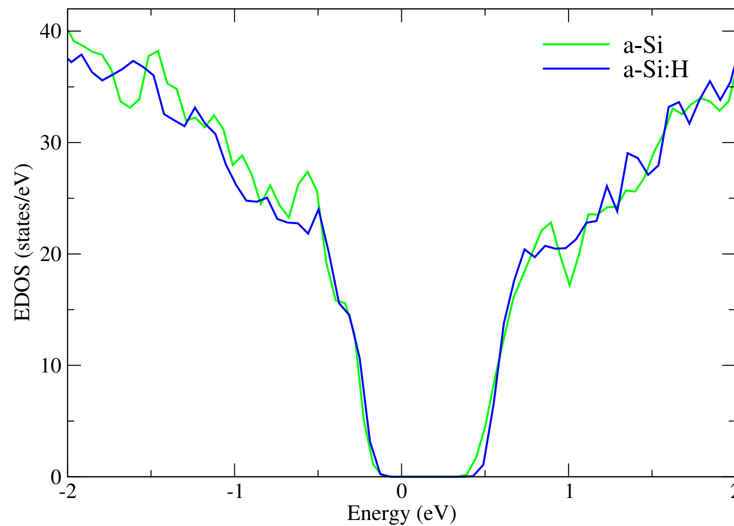

Figure 2.1: Electronic density of states (EDOS) with Fermi level at 0 eV. Green represents the EDOS for 64-atom *a*-Si and blue is the EDOS for 70-atom *a*-Si:H.

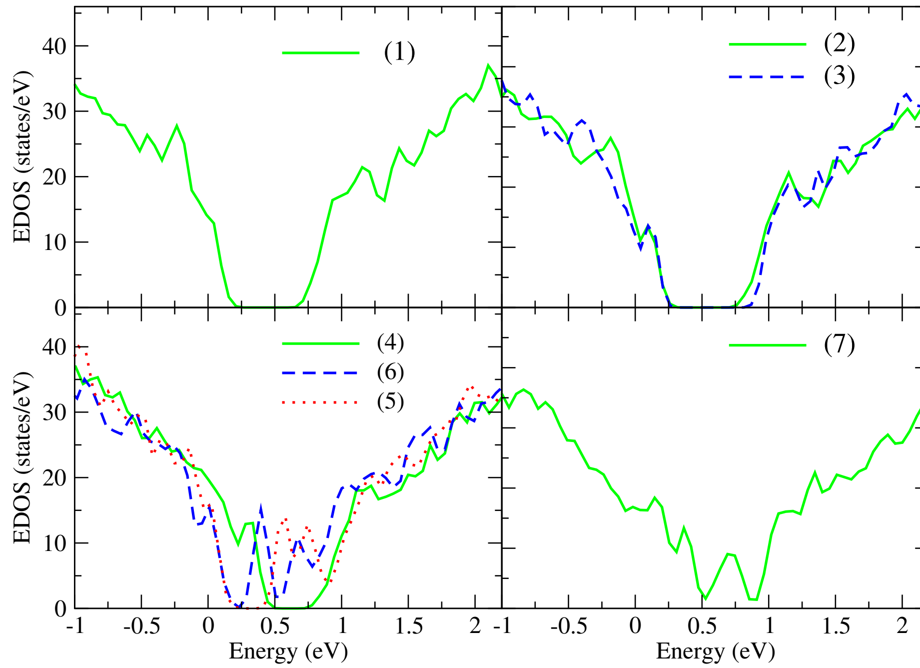

Figure 2.2: Boron doped *a*-Si with various impurity concentrations. Models (1), (2), (4) and (7) are 1.6%, 3.1%, 7.8% and 12.5% B doped *a*-Si respectively with each B having configuration B(4Si) [four Si neighbors to B]. In models (3) and (5), B dimers are formed with configuration B(3Si,1B). Model (6) consists of B4 cluster with configuration B(1Si,3B). Details of these models are provided in Table I. The Fermi energy is at 0 eV for each curve in the figure.

2.3 Impurities on a Static Lattice

The purpose of this section is to determine doping and non-doping configurations in B and P doped a-Si and also to understand the effect of hydrogen in doping. The electronic density of states (EDOS) is calculated for models doped with varying concentrations of B, P and hydrogen. Initially the EDOS of 64-atom a-Si (WWW model)[7] and 8.5% H doped a-Si, 70 atoms a-Si:H model is studied as shown in Figure 2.1. For both the models, there is a clear gap and the Fermi level is in the gap and we therefore interpret these models as representing a non-doped conformation.

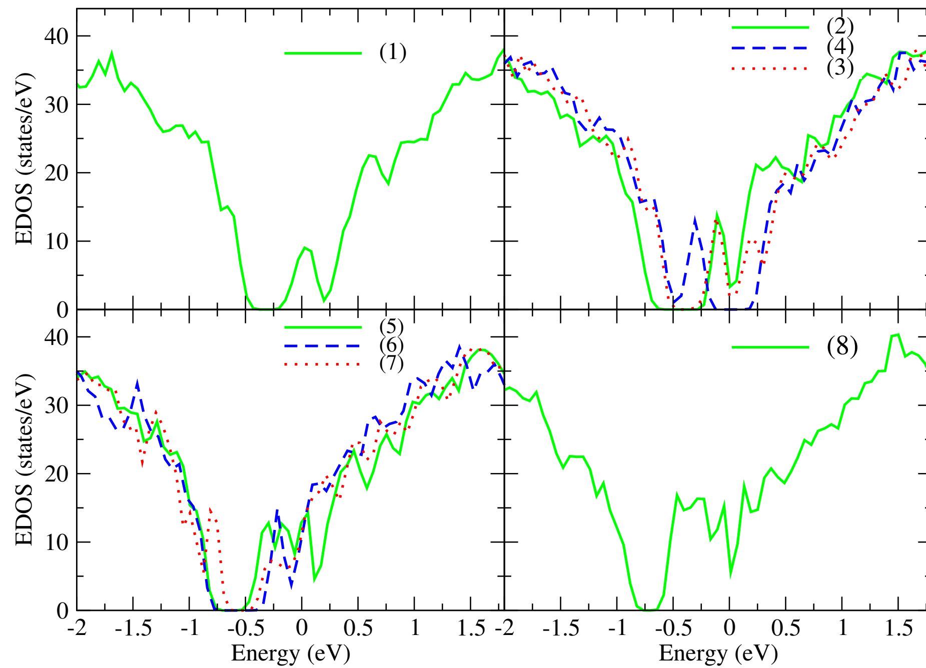

Figure 2.3: Phosphorous doped *a*-Si with different impurity concentrations. Models (1), (2), (5) and (8) are 1.6%, 3.1%, 7.8% and 12.5% B doped *a*-Si respectively with each P having configuration P(4Si) . In models (3) and (7) P dimers are formed with configuration P(3Si,1P) and model (6) consists of P4 cluster denoted by P(1Si,3P). P is three-fold in configuration (4) with configuration P(3Si). Details of these models are provided in Table II. The Fermi energy is at 0 eV for all the EDOS in the figure.

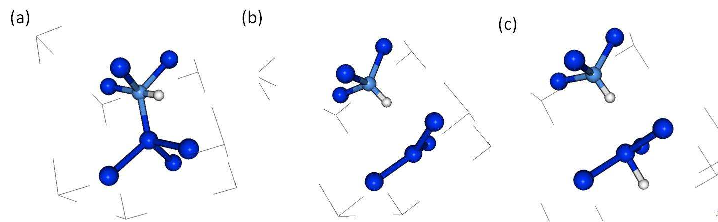

Figure 2.4: H passivation in B doped *a*-Si.(a) H bonds with B forming metastable B(4Si,1H) structure, (b) Relaxation breaks a Si-B bond forming B(3Si,1H) and a Si DB, (c) Another H passivates the Si DB.(Dark Blue=Si; Light Blue=B; White=H).

Further analysis was carried out with different concentrations of B and P doped on the 64-atom a-Si. Doping was studied initially by substituting impurities on highly tetrahedral Si sites. For the 1.6% doped system we investigated the H-passivation.

2.3.1 Boron and Phosphorous Doped a-Si

When impurities such as boron and phosphorous are introduced into a network of a-Si, the Fermi level may shift toward a band edge. We have studied seven different models of B-doped a-Si as shown in Fig.2.2. We calculated the electronic density of states (EDOS) for all the models with Fermi level shifted to zero in each case. The models are described in Table I.

In Fig.2.2, there are 4 panels that report the EDOS for seven different models as stated in the index of the panels. In models (1), (2), (4) and (7) of Fig.2.2 all B atoms are 'separate' in the sense that each boron is 4-fold coordinated with Si atoms which are denoted by B(4Si) and there is no B-B bond. All of these models represent a doped configuration with the gap cluttered with states for model (7). As the B concentration increases, more valence tail states are formed and the states move into the gap as can be seen in model (7).

In each case, there are three shorter bonds and one longer bond with the bonds highly strained. The average over the configurations for the four B-Si bonds are respectively 2.02 Å, 2.04 Å, 2.07 Å and 2.16 Å respectively. These bond lengths are highly strained compared to the mean bond length of Si-Si which is 2.34 Å[44], and in the spirit of our work on Urbach tails, can be thought of as inducing a strain field associated with the valence edge[48]. These strains create long bonds in the next nearest neighbor of B, with second nearest neighbor bond lengths near 2.5 Å. This effect is also observed in a large model of 215 Si atoms doped with a B atom at a perfectly tetrahedral Si site. It has been observed that the average bond length for the first nearest neighbor atom shell of B is 2.05

Å and the second nearest neighbor shell is 2.45 Å. From the third nearest neighbor shell there is no significant departure from the mean bond length of the a-Si network.

In model (3), the B is clustered, so that each B atom is bonded to another B atom and three other Si atoms and denoted by B(3Si,1B) forming B dimer. These conformations induce doping so long as B atoms are four-fold. However, when B clusters are formed, additional defect states appear near the conduction band tail, and they clutter the gap as can be seen for model (5) and model (6). The configuration for model (5) is comprised of B2 clusters (B dimer), in which B atoms are bonded with another B atom and three Si atoms and are denoted by B(3Si,1B). There are two such dimers in model (5). In model (6), B4 clusters are formed, which is one B bonding with three B atoms and one Si atom and is denoted by B(1Si,3B). These mid-gap states arise from defects which are mainly the under- and over-coordinated Si atoms. These configurations are shown in Table I.

As a summary of the static study of B-doped amorphous Si, the tetrahedral B dopes the a-Si network and shifts the Fermi level towards the valence band tail as expected from elementary considerations. Increasing the concentration of B introduces defect states in the gap which are mainly due to Si dangling bonds (DB) and floating bonds (FB), probably arising from the strained (short bonds) between B and Si.

Table 2.1: Static Boron Configurations.

Fig.2	Models n(B),n(Si)	B Clustering	Config.	Electrical Activity
1.	1B,63Si	Separate	B(4Si)	p doped
2.	2B,62Si	Separate	B(4Si)	p doped
3.	2B,62Si	B dimer	B(3Si,1B)	p doped
4.	5B,59Si	Separate	B(4Si)	p doped
5.	5B,59Si	B2 Cluster	B(3Si,1B)	p doped with defects
6.	5B,59Si	B4 Cluster	B(1Si,3B)	p doped with defects
7.	8B,56Si	Separate	B(4Si)	Many defect states

In the study of P doped a-Si, we have calculated the EDOS of eight different models in four panels as shown in Fig.2.3 with the Fermi energy shifted to zero. The EDOS of models (1), (2), (5) and (8) are for 1.6%, 3.1%, 7.8% and 12.5% P doped a-Si respectively. In these models, P atoms are substituted in perfectly tetrahedral Si atom sites, deep doner states are formed and the Fermi level shifts towards the conduction band tail and the systems are n-type doped.

The average bond length of P atoms formed with Si atoms (in tetrahedral sites) are 2.32 Å, 2.31 Å, 2.28 Å and 2.24 Å respectively. These are close to the average Si-Si bond length. There are eight different models presented in Fig.2.3. In models (1), (2), (5) and (8), P atoms are 'separate', which means each P atom is bonded to 4 Si atoms and there is no P-P bond. The configuration is denoted by P(4Si). In model (3), P2 dimer is formed in

which each P is bonded with another P atom and three Si atoms which is denoted by P(3Si,1P). In model (4), P is three fold which means each P is bonded to three Si atoms and is denoted by P(3Si). Model (4) consists of P4 cluster where each P forms bond with three other P atoms and a Si atom. The P4 cluster is denoted by P(1Si,3P). Model (7) comprises mixture of P2 dimer and P3 cluster. The configuration for the P2 dimer is denoted by P(3Si,P) and for P3 cluster it is P(2Si,2P). Our configurations are summarized in Table II.

Table 2.2: Static Phosphorous Configurations.

Fig.3.	Models n(P), n(Si)	P clustering	Config.	Electrical Activity
1.	1P,63Si	Separate	P(4Si)	*n* doped
2.	2P,62Si	Separate	P(4Si)	*n* doped
3.	2P,62Si	P dimer	P(3Si,1P)	*n* doped
4.	2P,62Si	Threefold P	P(3Si)	Undoped with defects
5.	5P,59Si	Separate	P(4Si)	n-doped
6.	5P,59Si	P4 cluster	P(1Si,3P)	*n* doped
7.	5P,59Si	P2/P3 cluster	P(3Si,1P), P(2Si,2P)	*n* doped
8.	8P,56Si	Separate	P(4Si)	Gap filled with tail states

It can be seen that as the concentration of P increases more defects states are formed near the conduction band edge (see model(8)) that eventually closes the gap. As long as

the P is tetrahedral, P dimers dope the system as can be seen in model (3) and model (7) with defect tail states. The configuration is undoped for three fold P shown in model (4). In model (6) and model (7), P clusters also dope the system if P is tetrahedral.

As a summary for the static study of P doped amorphous Si, tetrahedral sites dope the system by shifting the Fermi level towards the conduction band tail while three-fold P leads to non-doping configuration. Increasing the concentration of P produces more defect states in the gap as the network rearranges to produce more three-fold and five-fold Si atoms.

The most notable contrast between B and P doping is a large local strain around B, and a more substitutional character for P. This strain seems to be relevant to the work of Schiff concerning broad valence tails[46].

2.3.2 H Passivation in Hydrogenated B- and P-Doped a-Si

The efficiency of doping is highly influenced by the presence of hydrogen in a network. H passivates the dangling bonds present in the network and increase the doping efficiency whereas bond centre H near impurites poisons the doping and reduce doping efficiency. To study these properties H atoms are introduced in B and P doped a-Si and their effect in doping is studied in terms of the shift in Fermi energy level in EDOS.

To study the role of hydrogen in B and P doped a-Si, H atoms are introduced at various sites of the network thereby forming initial metastable structures. These structures are then relaxed to find a stable configuration. The effect on doping is studied by calculating the EDOS to observe the shift in Fermi level. We discuss first, H passivation in B-doped a-Si and then on P-doped system.

In Fig.2.4(a), H is initially attached to a B atom forming a metastable configuration B(4Si,1H), B forming bonds with 4 Si atoms and 1 H atom. After relaxation, H breaks a B-Si bond and forms B(3Si,1H), a B bonded with 3 Si and 1 H atom, structure with a Si

DB. This configuration is non doping as the Fermi level shifts into the gap with a defect state due to the creation of a Si DB (Fig.2.5). However, if another H passivates the Si DB, the Fermi level shows p-type activity. Thus, we can conclude that B(3Si,1H) with Si DB poisons doping and B(3Si,1H) without Si DB is an effective doping configuration which is consistent with other work[44, 45].

Next, we placed a hydrogen atom at a Si-Si bond center (BC) near B and studied its effect on doping. It is found that H is stable in BCs and in this configuration it suppresses the doping. We studied two different cases of H passivation, the first with H at a BC of a second nearest neighbor of B and second at third nearest neighbor of B atom (Fig.2.6). In the top panel of Fig.2.6(a), H is initially bonded to a Si neighbor of B and after relaxation H breaks the Si-Si bond and stays at the BC forming B-Si-H-Si structure (top panel of Fig.2.6(b)). The EDOS of this structure shows that the Fermi level shifts into the gap, thereby suppressing the doping (Fig.2.7(left)). A similar study was carried out for H initially bonded to the second nearest neighbor Si of B atom, and after relaxation it moves to the BC forming B-Si-Si-H-Si structure as shown in lower panel of Fig.2.6(a) and Fig.2.6(b). The EDOS of this structure shows that the Fermi level is shifted towards the gap suppressing doping (Fig.2.7 (right)). These results indicate that the BC H, sufficiently close to B atoms poisons the doping.

In all the above cases, B remains in a tetrahedral conformation after relaxation and there is no Si DB left in the network and no defect states in the gap. In reference[25], it is suggested that at low B concentration holes could be trapped at strained Si-Si bond centers[52]. The charge due to these trapped holes may be compensated by H atom trapped in the bond centers. In a-Si:H, B(4Si,1H) forms a stable configuration but when an electron is removed from the system, the Si-Si bond breaks and H occupies the BC position.

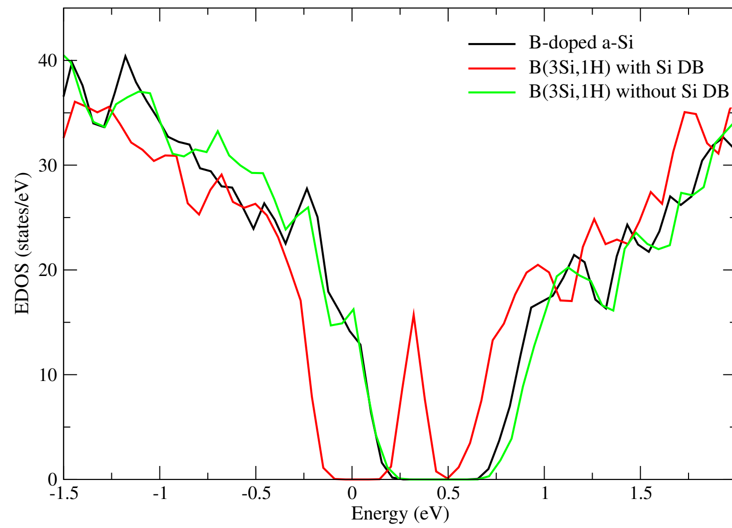

Figure 2.5: Comparison of EDOS for different configurations in H passivation for B-doped *a*-Si. Green denotes the EDOS of B bonded with 3Si and 1H without Si dangling bond which is doped configuration. Red is the EDOS of B bonded with 3Si and 1H with Si dangling bond and is undoped configuration with a defect state in gap. The Fermi level is shifted to 0 eV in all the EDOS.

In P-doped a-Si, H passivation is studied in a similar way as for the B-doped a-Si. H is initially bonded with P atom forming a P(4Si,1H) metastable structure. After relaxation, Si-P bond breaks and H sticks to P forming P(3Si,1H) structure with a Si DB. When another H is added to the system, the Si DB is passivated (Fig.2.8). The EDOS of these structures are shown in Fig.2.9. For P(3Si,1H) structure, the fermi level shifts in the gap with a defect state due to a Si DB, thereby poisoning the doping. When Si DB is passivated by another H, the configuration is doped. Thus, we conclude that P(3Si,1H) without Si DB is an effective doping configuration for H close to P atom.

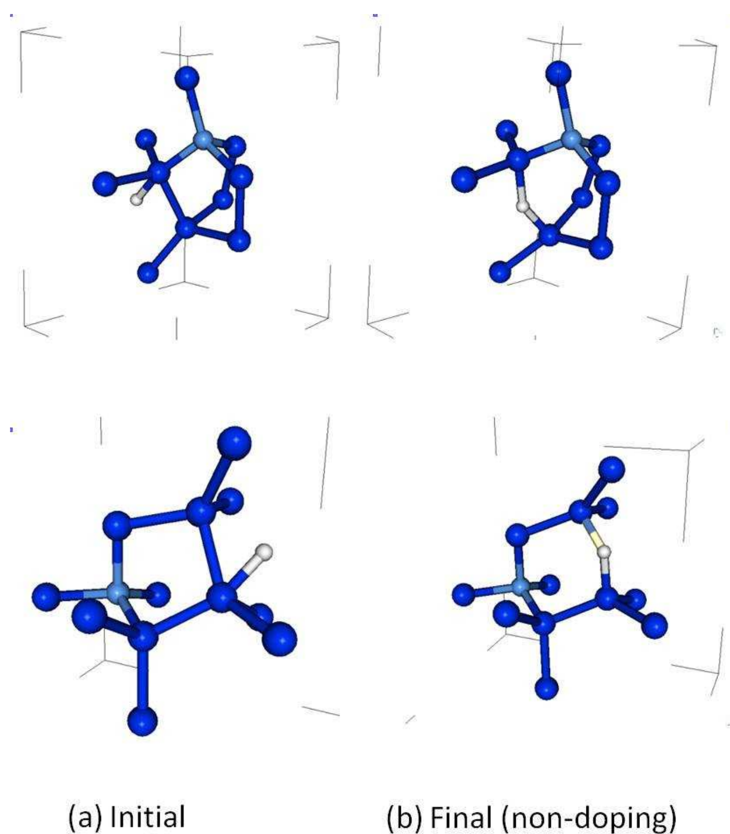

Figure 2.6: Bond center H forming structures B-Si-H-Si (top) and B-Si-Si-H-Si (bottom).(Dark Blue=Si; Light Blue=B; White=H)

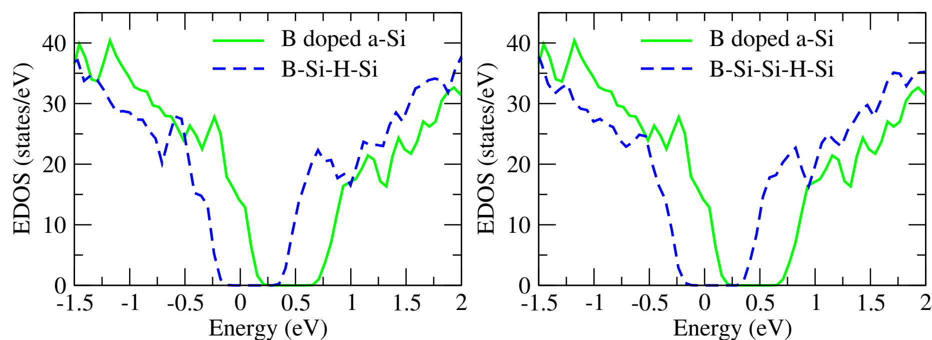

Figure 2.7: (Blue left) EDOS for B-Si-H-Si BC structure after relaxation which is undoped. (blue right) EDOS for B-Si-Si-H-Si BC structure after relaxation which is undoped. Green is the EDOS of B-doped *a*-Si and is doped configuration. The Fermi level is shifted to 0 eV in all the EDOS.

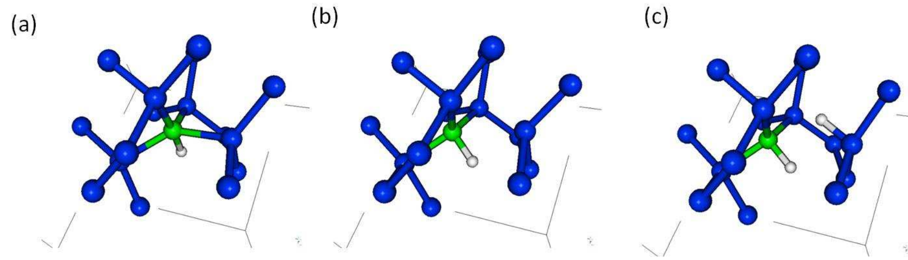

Figure 2.8: H passivation in P doped *a*-Si.(a) H bonds with P forming metastable P(4Si,1H) structure, (b) Relaxation breaks a Si-P bond forming P(3Si,1H) and a Si DB, (c) Another H passivates the Si DB.(Dark Blue=Si; Green=P; White=H).

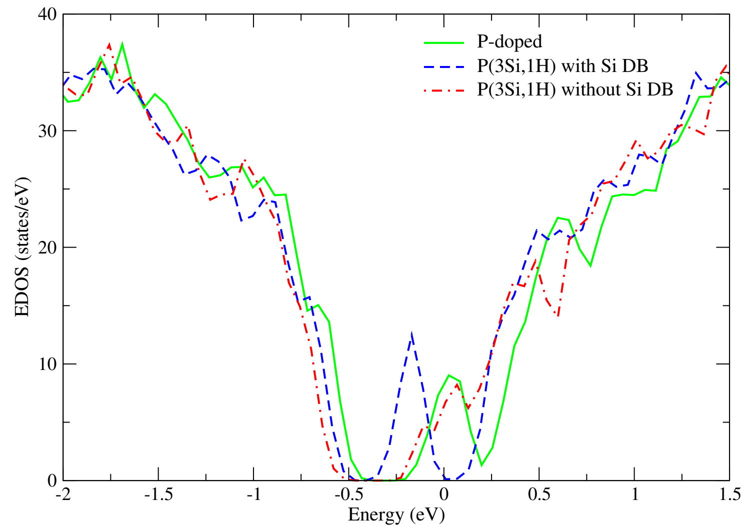

Figure 2.9: Comparison of EDOS for different configurations in H passivation for P-doped *a*-Si. Blue is the EDOS of the final configuration in which P bonds with 3Si and 1H atoms with Si dangling bond. Red is the EDOS of the final configuration in which P bonds with 3Si and 1H without Si dangling bond. The Fermi energy is shifted to 0 eV in all the EDOS.

We study two cases for H passivation in P doped a-Si. H is initially placed at the bond center (BC) of P-Si, forming P-H-Si structure and then relaxed. It is observed that P-H bond breaks, leaving P 3-fold and the H atom bonds with Si as shown in the top panel of Fig.2.10. In the EDOS of later configuration, the Fermi level shifts into the gap making

the system undoped (Fig.2.11 (left)). In another case, shown in the bottom panel of Fig.2.10, H is placed in the BC on first and second nearest neighbor Si atoms of P, at Si-Si BC and forming P-Si-H-Si structure, and then relaxed. The network reconstructs, P becomes 3-fold and H sticks to a Si DB. The EDOS displays the suppression of doping without defects states (Fig.2.11(right)).

In contrast to the H passivation in B doped a-Si, H does not prefer the bond center position in P doped a-Si. Instead it passivates Si DB. This result is consistent with NMR experiments which predicts that in P-doped a-Si:H about 40 % H are in the second nearest neighbor of P [43].

Thus, tetrahedral B and P dope the system but high concentration of B and P impurities introduce mid-gap states. Clusters of impurities also create defect states in the gap, leading to compensation effects. The low doping efficiency is partly due to H passivation. An a-Si network doped with B and P has higher number of under- and over-coordinated Si and H in such amorphous network passivates the Si DB (3-fold Si), thereby increasing the doping efficiency. It is found that B(3Si,1H), P(3Si,1H) and Si(3Si,1H) are effective doping states. The hydrogen atom prefers to stay at nearby bond center for B doped a-Si while in P doped a-Si it prefers to bond with Si dangling bond leaving P three fold.

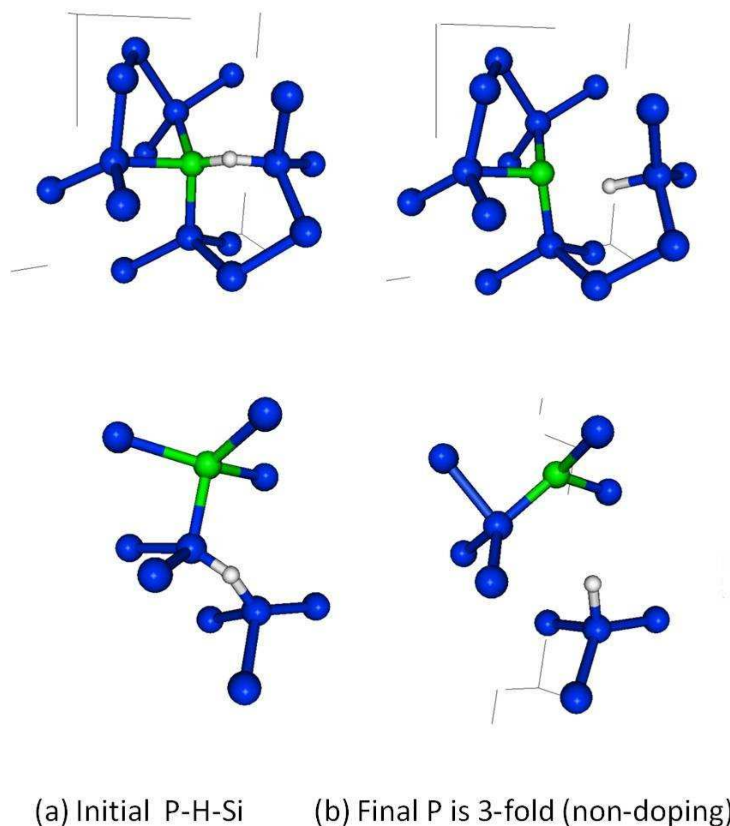

Figure 2.10: H passivation in P doped *a*-Si. (left) Top panel forming P-H-Si and bottom panel forming P-Si-H-Si structure. (right) After relaxation, P forms 3-fold bond nad H passivates Si DB producing non-doping configuration. (Blue=Si; Green=P; White=H)

2.4 Dynamical Lattice

We have performed thermal molecular dynamcis (MD) simulations of hydrogenated a-Si doped with B and P at different temperatures (300K, 400K, 600K, 800K and 1000K). Note that for temperatures above 600K, laboratory samples lose H, with commensurate changes in structure and conduction. We consider temperatures above this to observe rare events in the network dynamics, H hopping and electronic structure. We tracked the trajectories and bonding of all the atoms. We also studied the doping in these systems which, in certain cases are evolving or fluctuating with time.

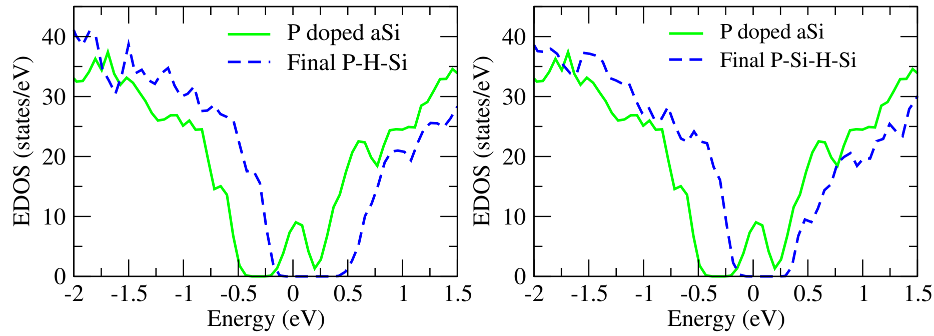

Figure 2.11: EDOS for two H passivation case. (left) Initial P-H-Si structure after relaxation forms P(3Si) and Si(3Si,1H), (right) Initial P-Si-H-Si structure after relaxation forms P(3Si) and Si(3Si,1H). The Fermi level is shifted to 0 eV in all the EDOS.

The dynamical variable chosen to probe this was the HOMO-LUMO gap, ξ, and the reason behind it is based on defining the doping in terms of the conductivity which depends on this dynamical variable (since the Kubo-Greenwood formula shows that conduction may be expected if there there are degenerate states at the Fermi level, following Mott and Davis[53]). We study the doping dynamics based on the concept of correlating this ξ with other dynamical variables such as fluctuations in structure or H-hopping. As we indicated in the Introduction, thermal motion and H hopping can have a significant role in modulating the electronic eigenvalues near the Fermi level. We also studied the change in coordination number of the hydrogen and its correlation with ξ. Of course the study of ξ and its time evolution does not completely treat the doping problem. Conduction is possible only if states are extended in the sense of Anderson[23, 54, 55]. Still, as we argue below from the Kubo-Greenwood formula, the condition for charge transport in the presence of (extended) occupied and unoccupied states nearly degenerate with the Fermi level.

This study can be related to the noise power fluctuation experiment by Parmen which states the fluctuations of resistance in doped a-Si:H is sensitive to a small number of

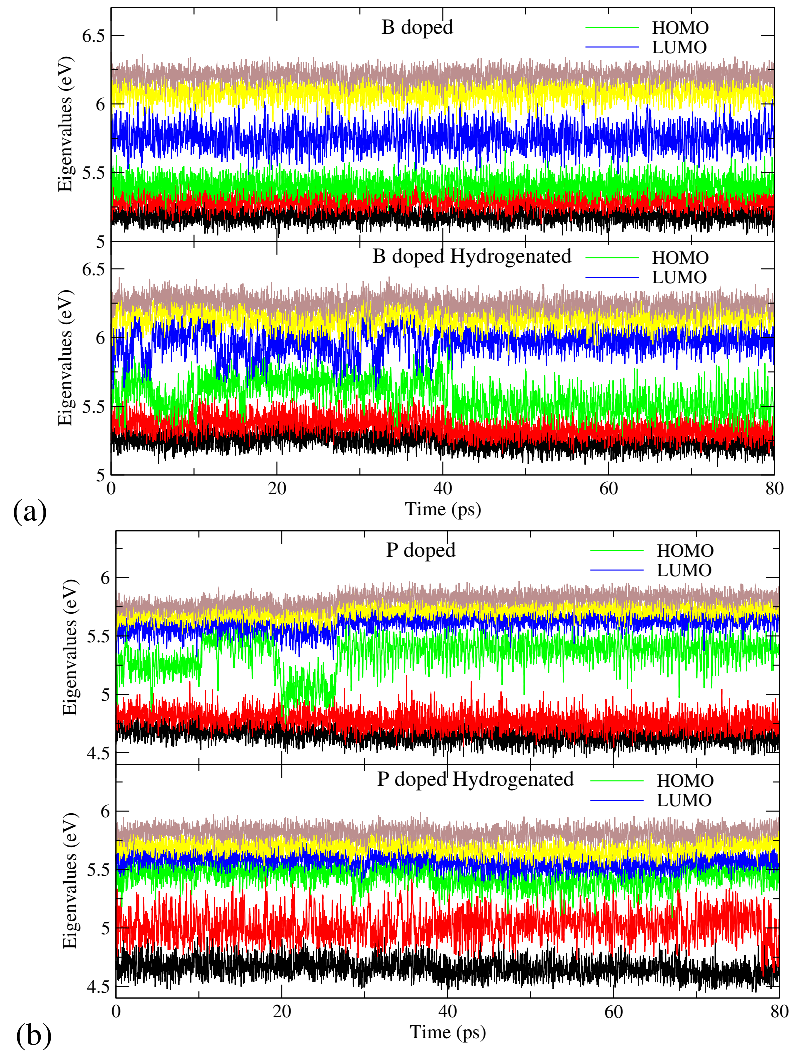

Figure 2.12: Plot of highest three valence band and lowest three conduction band energy levels. (a) For B-doped and hydrogenated B-doped *a*-Si at 600 K, (b) for P-doped and hydrogenated *a*-Si at 600 K.(Green) HOMO level (Blue) LUMO level. Proximity of Green and Blue levels implies conduction is possible (the HOMO-LUMO gap is small).

fluctuations and change with time. It was was observed that the motion of the bonded hydrogen was correlated with variations in the resistance[56]. We have presented here the dynamics of the doped a-Si:H and observe the fluctuation in the conductivity due to the motion on the hydrogen in the network.

2.4.1 Energy Gap and Kubo-Greenwood Formula

To develop this picture a bit further, it is worth reminding that the conductivity for disordered solid can be expressed from microscopic quantities (wave functions, eigenvalues etc) with the Kubo-Greenwood formula[57, 58]. For a very clear derivation and elementary applications, see Mott and Davis[53]. As it is usually interpreted, this result is applied to a static configuration of a lattice.

We have extended this idea elsewhere, by adopting an adiabatic picture, in which we thermally average the Kubo-Greenwood formula over a long constant temperature MD simulation to pick up thermal effects on carrier transport (for details see Ref [59]). In practice, this amount to a computing:

$$\sigma_{DC} = \frac{2\pi e^2 \hbar \Omega}{m^2} \overline{|D_{\epsilon_f}|^2 N^2(\epsilon_f)}. \tag{2.1}$$

Here, the bar indicates thermal or trajectory average, D_{ϵ_f} is a matrix element of $\partial/\partial x$ between single-particle (Kohn-Sham) states near the Fermi level, Ω is the cell volume, and $N(\epsilon_f)$ is the density of states. This expression emphasizes that DC conduction may occur when (i) the density of states at the Fermi level is non zero, and (ii) the momentum matrix element is also non-vanishing. It implies that conduction accrues for instantaneous configurations that support the conditions (i) and (ii).

In Fig.2.12, we reveal the fluctuations in energy eigenvalues for the highest three valence band and lowest three conduction band states. The upper panel of Fig.2.12(a) is for B doped a-Si without hydrogen and the lower panel is B doped a-Si with hydrogen. In B-doped a-Si, the HOMO-LUMO gap is small enough to consider the system to be conducting. Upon addition of H, there is thermal modulation of both HOMO and LUMO states which can be seen in the lower panel of Fig.2.12(a). At certain interval in the thermal simulation, the HOMO-LUMO levels overlap and it is the highly conducting

configuration according to KGF. The period for which the HOMO-LUMO gap (ξ) opens up is the non-doping configuration.

In P-doped a-Si, the HOMO level is shifted towards the LUMO level and the HOMO-LUMO gap is almost zero for most of the simulation time which can be seen in Fig.2.12(b). There is a small fluctuation in the HOMO level around 20ps to 30ps that changes the system to non-doping mode which is due to the change in the structure of P from 4-fold to 3-fold and 2-fold. We can say that 3-fold and 2-fold P are the undoped configuration. When H is added to the P-doped a-Si, the undoped configuration is completely removed and the system becomes n-type doped with HOMO and LUMO levels overlapped. This again demonstrates the n-type behavior of H in the network. The network rearranges to give the tetrahedral P (Fig.2.12(b)).

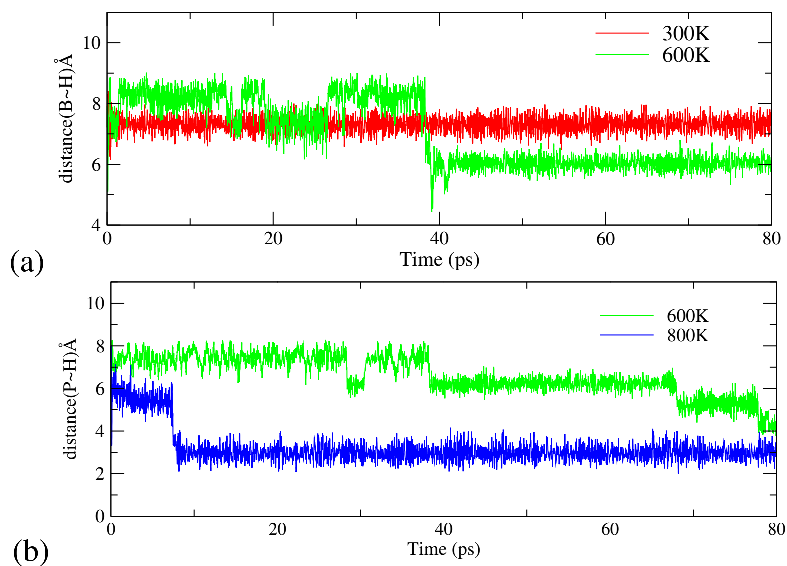

Figure 2.13: Distance between Hydrogen and impurites (a)B-doped hydrogenated *a*-Si (b)P-doped hydrogenated *a*-Si. (Red=300 K; Green=600 K; Blue=800 K)

2.4.2 Hydrogen Hopping and Coordination Number

We have added the n-type (P) and p-type (B) impurities in the network of a-Si by substitutional method and then carried out thermal simulation. Hydrogen atoms were added to determine the effect of H on the dynamics of doping and conduction. The H atom was placed at various Si-Si bond centers at varying distances from the impurities atoms in doped n-type (P-doped) and p-type (B-doped) a-Si models.

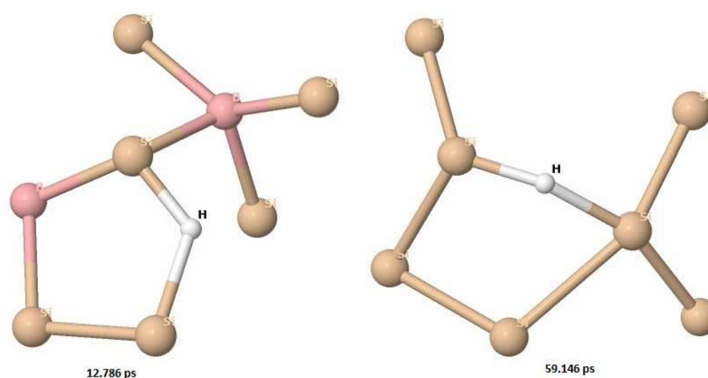

Figure 2.14: Hydrogen hopping between bond centers and passivating the Si dangling bonds in hydrogenated B doped *a*-Si DB at various snapshot for 600 K thermal MD.

The variation of distance of hydrogen from impurities for different temperatures is shown in Fig.2.13. The main purpose of this calculation is to determine a range (distance from B) for which the H is attracted. Our calculations show that the hydrogen in a network are attracted towards the impurity sites, doubtless to reduce strain in the region containing the dopant. In both B- and P-doped hydrogenated system, hydrogen tends to move towards the impurities. The motion is significant only at sufficiently high temperature. For 300K, in B-doped hydrogenated a-Si, it is seen that the motion of hydrogen is almost insignificant on the time scale of our simulation. The prominent movement towards the impurity is visible for P-doped hydrogenated a-Si (Fig.2.13(b)) where it can be clearly seen that for 600K and 800K the thermal energy is sufficient for H to move towards the P

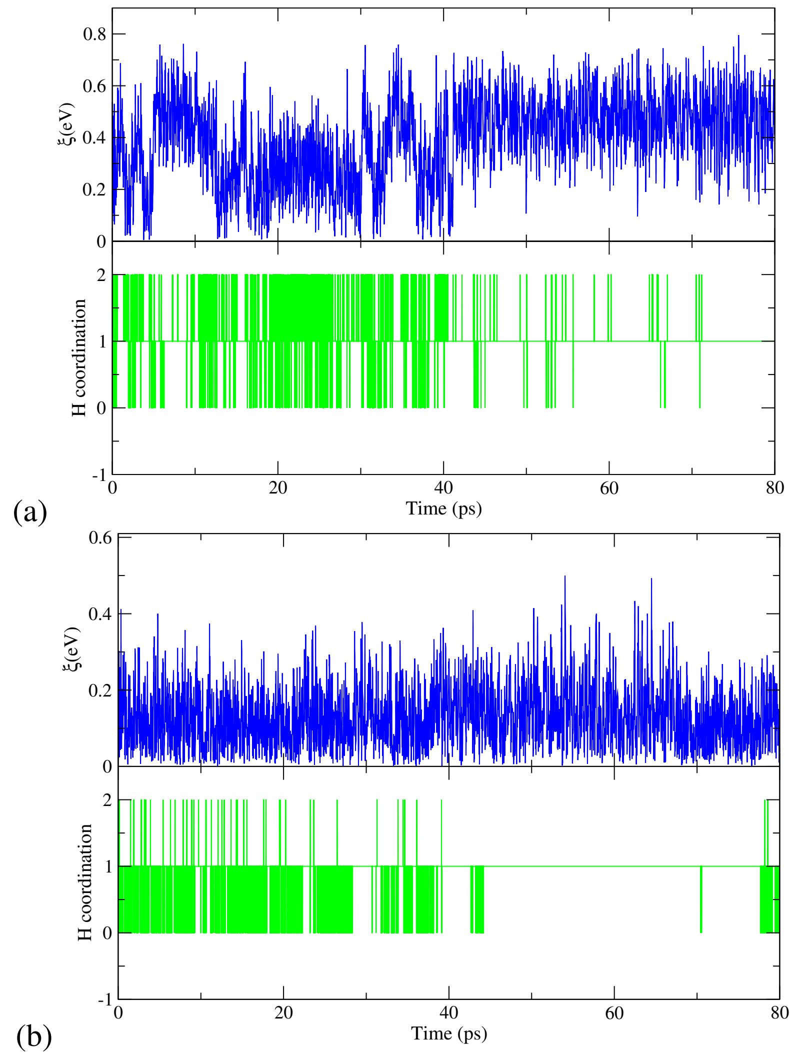

Figure 2.15: (Lower half) Hydrogen coordination fluctuation (Upper half) enery-gap fluctuation (a)B-doped hydrogenated *a*-Si (b)P-doped hydrogenated *a*-Si. Zero coordination means H is in process of hopping.

atoms. At 1000K, H atom sticks to the B (not shown here) which help us conclude that if the thermal energy is sufficient, then H atoms eventually move toward the impurity sites.

We performed a microscopic study on the motion of hydrogen in the system and the change in its coordination number. It is found that H in the network is mobile and its hopping changes the structure and dynamics of the network. By tracking the motion of the

hydrogen atoms, it has been observed that the H atom prefers to move towards the B or P sites by hopping through various bond sites, providing strong evidence that H atoms in a-Si network are highly mobile and have higher affinity for the impurities. Another important feature noticed in the study of hydrogen hopping is the significant decrease in the HOMO-LUMO gap (ξ) in the region where H-atom coordination changes rapidly from free to singly coordinated and then to two-fold as shown in Fig.2.14. The coordination cut-off distance for H-Si bond is taken as 1.65 Å for calculations.

In an undoped a-Si network H prefers to stay in the sites of highly distorted bonds and bond angles. When B and P are introduced in a perfectly tetrahedral sites in an a-Si network, they introduce strain (especially B). So, the region becomes distorted and H atoms introduced in such network has tendency to move towards those regions. From a different perspective, as H bonds more strongly with B than with Si (bond dissociation energy of B-H is 3.52 eV and Si-H is 3.10 eV)[60], in B doped a-Si, H moves towards B due to the strain and also prefers to bond with B rather than Si. This is consistent with NMR experiments which predicts that about 40 % H in p-doped a-Si:H are in the first nearest neighbor of B[43]. In contrast, H bonds similarly with P and Si (the bond dissociation energy of P-H is 3.08 eV and Si-H is 3.10 eV)[60] and seems consistent with the result of NMR that about 40 % H atoms in P-doped a-Si:H are in the second nearest neighbor shell of P[43].

Doping phenomena are influenced by the motion of hydrogen in the network. In Fig.2.14 which have shown the hopping of H atom from various bond centers to passivating the dangling bond at 12.78 ps, 24 ps, 59.146 ps and 79.64 ps snapshots for B-doped hydrogenated a-Si at 600K. This is consistent with the noise power fluctuations experiment by Kakalios and his group which suggest that the rearrangement of hydrogen bonding configurations which involves the collective motion of many hydrogen atoms changes the electronic properties of a-Si:H[56].

A goal of this work is to bring forth a new suggestion that the motion of H and its changing coordination in the network affects the doping significantly. This feature can be seen clearly in Fig.2.15(a) for B-doped hydrogenated a-Si at 600K between 10 ps to 40 ps time where the energy gap has decreased significantly. In hydrogenated P-doped a-Si Fig.2.15(b), although the coordination of H atom fluctuates in the beginning, at later times it forms a single bond with Si, thereby passivating the DB which is as expected from the doping point of view because in n-type doping both P and H assist doping and the energy-gap is small. The B atoms substituted in tetrahedral Si atom sites have consistent four fold coordination while the coordination of P changes from four to 3-fold and sometimes even 2-fold. We found that this change in coordination of P atoms has significant effect in doping process as the study of dynamics with P-atoms not substituted in the perfectly tetrahedral Si sites will result in an undoped system which is quite consistent with the experimental results.

2.5 Conclusion

Our calculations suggest that although Mott's view that non-tetrahedral impurities do not dope an a-Si network is correct, this is only the part of the story of low doping efficiency. H passivation and the special attraction of H to impurities is also a key to understanding low doping efficiency. B substituted into a tetrahedral Si site, creates a substantial strain in local bonding, which attracts H atoms and induced H passivation and doping suppression. In P-doped a-Si, bonds are less strained compared to B-doped a-Si and H passivation follows similarly.

It is shown in the work of Abtew and coworkers[39, 42] that H is highly mobile. This mobility can lead to fluctuations in HOMO-LUMO gap, (denoted by ξ in this paper) that also strongly affects the conductivity.

3 Force-Enhanced Atomic Refinement (FEAR): Structural Modeling With Empirical Interactions in a Reverse Monte Carlo Approach

The work shown in this chapter is published in **Pandey, A., Biswas, P., and Drabold, D. A. (2015). Force-enhanced atomic refinement: Structural modeling with interatomic forces in a reverse Monte Carlo approach applied to amorphous Si and SiO_2.** *Physical Review B, 92*(**15), 155205.**

3.1 Introduction

Conventional molecular-dynamics (MD) simulations of amorphous materials suffer from a usual difficulty of the high computational cost associated with simulating large models using quantum-mechanical methods, such as *ab initio* molecular dynamics (AIMD). Further, for amorphous solids with *weak* or no *glassy* behavior (e.g. *a*-Si and *a*-Ge), AIMD technique such as "melt-quench" performs poorly. Similarly, computational approaches to construct structural models of amorphous solids by inverting experimental data, along with the local chemical and geometrical ordering of the networks, often fail. An archetypal example is the Reverse Monte Carlo (RMC) method [61, 62], which constructs a three-dimensional model of a material by inverting experimental diffraction data. While RMC is very simple to implement and has been used to model a variety of disordered solids [63–65] (e.g. glasses, liquids, polymers, etc.) in the past, the very scalar nature of diffraction data dictates that the method cannot be used to uniquely determine the structure of amorphous solids using diffraction data only. Thus, development of new approaches are required to address these materials.

An ideal approach to computational modeling of complex amorphous materials should incorporate the state-of-the-art total-energy and force methods and the judicious

application of *a priori* information–experimental data pertaining to the material. When these schemes are suitably merged, the resulting structural models should reflect our full state of knowledge about the material. A number of hybrid approaches has been developed that successfully couple a total-energy functional (quantum-mechanical or otherwise) with *a priori* information some of them are reviewed below.

Compelling ‘uniformity’ as a constraint for the refinement of the atomistic-scale structures, was adopted by Goodwin and coworkers in their invaraint environment refinement technique [47]. A liquid-quench procedure, combined with a hybrid Reverse Monte Carlo (HRMC) approach, which incorporates both experimental and energy-based constraints has been employed by Opletal and coworkers in their study of amorphous carbon [24]. A similar approach via HRMC with bonded and non-bonded forces was used by Gereben and Pusztai to study liquid dimethyl trisulfide [66]. Likewise, by refining the initial interatomic empirical potential-energy function and fitting the input experimental structure-factor data, empirical potential structure refinement (EPSR) has been quite successful in predicting liquid structures [67]. Recently, an *electronic a priori* information has also been included in a modeling amorphous materials [68]. An alternative approach, experimentally constrained molecular relaxations (ECMR), which incorporates experimental information in first-principles modeling of materials in a ‘self-consistent’ manner was discussed in [25].

In this chapter, we report a structural modeling technique called force-enhanced atomic refinement (FEAR). Our method uses RMC to fit the input experimental data and parsimoniously employs interatomic forces obtained from (classical) total-energy functionals to restrict the search in the energetically-favorable region of the configuration space in a self-consistent manner. We have studied a-SiO_2 and a-Si using this approach.

Unlike other hybrid approaches [24, 66], where the total-energy of the system is coupled to RMC for accepting and rejecting atomic moves, the movement of the atoms in

FEAR, due to interatomic forces, is independent of the RMC moves. This enhances the efficiency of the method by reducing the total computational cost associated with force calls. The computational efficiency of the technique has been studied by comparing the number of force calls with other MD approaches.

The rest of this chapter is organized as follows. In section II, we describe the basics of the FEAR method and its implementation. Section III discusses the results for *a*-SiO_2 and *a*-Si. In section IV, we present the conclusions of our work.

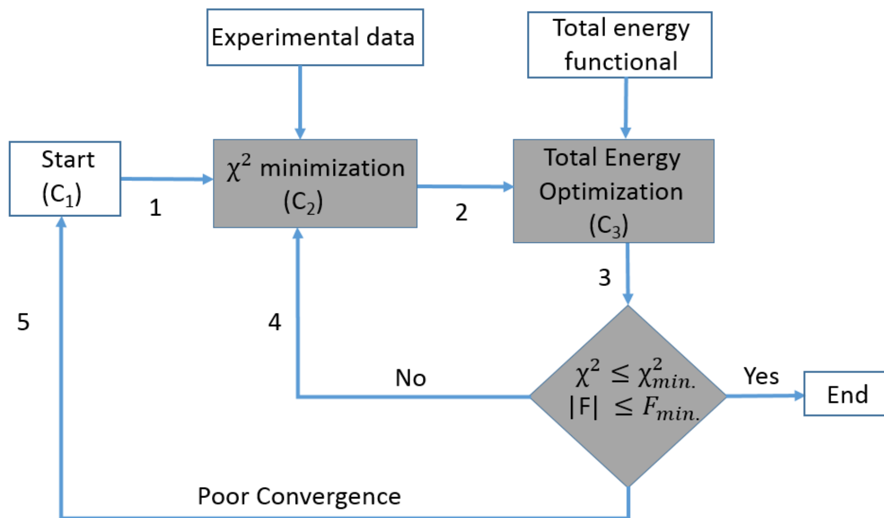

Figure 3.1: A schematic diagram of the FEAR method. The principal computing loop is highlighted in grey.

3.2 Methodology: Basics of FEAR and Its Implementation

A review of Reverse Monte Carlo (RMC) [24, 25, 61, 63, 64] and the related methods suggests that diffraction data alone is insufficient to determine the structure of complex amorphous solids. This is particularly so for amorphous semiconductors, where the presence of directional bonding cannot be inferred directly from one-dimensional diffraction data only. While the inclusion of structural constraints proves to be particularly

useful in RMC simulations [69], they do introduce additional complexities in the search space. For multi-component systems, this can be a serious impediment and, in some cases, may render the problem intractable even with gradient information. The choice of appropriate constraints itself can be highly nontrivial. Owing to the hierarchical nature of the geometrical/structural constraints in complex disordered systems, it is generally beneficial to include lower-order constraints first, which are followed by higher-order constraints of increasing complexity and information content. However, the presence of too many constraints can be detrimental to a problem due to the competition between the constraints. Such competing constraints can adversely affect the efficiency of a search procedure by introducing complex rugged structure in the multi-dimensional configuration space, which makes it difficult for the optimizer to evolve and, thus, to determine the optimal solution space for structural determination. Further, the correct structural solutions often crucially depend on the strength of the constraints (i.e. weight factors), which are generally obtained heuristically after several trial runs in optimizations based on stochastic search algorithms. Thus, the determination of structure of complex disordered solids from a set of experimental data and structural/geometrical constraints continues to pose a challenging problem in condensed-matter sciences.

In the present approach, we intend to avoid some of these difficulties by introducing the following steps: i) optimization of a total-energy and penalty functionals in separate subspace; ii) inclusion of gradient information to optimize the total-energy functional; iii) incorporation of special atomic displacements to enhance the convergence of total energy during subspace optimization by moving a set of atoms associated with strained local configurations. Step I essentially eliminates the need for weight factors that are necessary for optimization of an augmented ‘effective energy’ functional. Instead, subspace optimizations proceed in tandem with each other and, thereby, establish a ‘coupling’ between steps I and II. Unfavorable configurations, which are generated in step I, are

either corrected or rejected in step II and vice versa. We emphasize that the approach is highly flexible; the exact implementation of the method can vary and may depend on the degree of accuracy and the efficiency one needs to achieve in optimizing models with several hundreds atoms. While a number of sophisticated algorithms can be employed for subspace optimizations (such as deterministic conjugate-gradient [70] type approaches to stochastic exchange-replica Monte Carlo [71] and evolutionary search procedures [72]), for the sake of simplicity and exploring the efficacy of this approach at its basic level, we confine ourselves to the steepest-descent method and Reverse Monte Carlo approach for optimizing the total energy and experimental structure-factor data, respectively. We show that even at this elementary level of implementation, the method is profitable and holds the promise for further development using the state-of-the-art multi-objective optimization (MOO) techniques developed in recent years. Thus, in the FEAR approach, the statement of the problem can be written as:

$$\min_{\{q\}} P(\{q\}), \quad P \equiv \chi^2 \otimes \Phi, \tag{3.1}$$

where Φ, χ^2, and $\{q\}$ stand for a total-energy functional, a penalty function involving experimental structure factor, and 3N-dimensional configurational coordinates, respectively. Following McGreevy and others [61, 65], we can write,

$$\chi^2 = \sum_i \left[\frac{F_E(k_i) - F_C(k_i)}{\sigma(k_i)} \right]^2, \tag{3.2}$$

where $F_{E/C}(k_i)$ is the experimental/computational structure factor, and $\sigma(k_i)$ is the error associated with the experimental data for wave vector k_i.

To illustrate our method, we have chosen two canonical examples of amorphous systems: amorphous silica (a-SiO_2) and amorphous silicon (a-Si). The former is a classic glass-former, and can be readily obtained by quenching molten models at high temperature. The latter is preferably modeled via event-based approaches, such as Winer-Wooten-Weire (WWW) [7] and activation-relaxation techniques [31]. Both

systems have been studied extensively in the literature, which provides a wealth of information for comparing experimental data with computational results for various physical quantities. Here, we choose to employ the environment-dependent interatomic potential (EDIP) by Justo et al. [73] for modeling a-Si. For a-SiO_2, we choose the potential proposed by Beest et al. (BKS) and their parameters [74]. The functional form of the BKS potential is given by,

$$\phi_{i\alpha,j\beta} = \frac{Q_\alpha Q_\beta}{r_{i\alpha,j\beta}} + A_{\alpha\beta} \exp(-B_{\alpha\beta}\, r_{i\alpha,j\beta}) - \frac{C_{\alpha\beta}}{r^6_{i\alpha,j\beta}}, \tag{3.3}$$

where $\phi_{i\alpha,j\beta}$ is the interaction energy between two atoms of species α and β at sites i and j, respectively. The parameters Q, A, B and C depend on atomic species and can be found in [75].

The presence of the electrostatic interaction in Eq. 3.3 stipulates that the Ewald summation [76] should be used in the calculation of the total energy and forces. However, as shown by Wolf et al. [77] in a recent communication, a pairwise sum can be constructed in real space by ensuring charge neutrality of the system such that the sum produces results very similar to that obtained from the Ewald summation. We have adopted this real-space approach to calculate the total energy and forces via Wolf's summation. Following these authors, the expression for the electrostatic force between two species α and β at sites i and j can be written as:

$$\begin{aligned} F^{i\alpha,j\beta} = Q_\alpha Q_\beta \Bigg\{ & \frac{\operatorname{erfc}(\kappa r_{i\alpha,j\beta})}{r^2_{i\alpha,j\beta}} + \frac{2\kappa}{\pi^{1/2}} \frac{\exp(-\kappa^2 r^2_{i\alpha,j\beta})}{r_{i\alpha,j\beta}} \\ & - \frac{\operatorname{erfc}(\kappa R_c)}{R_c^2} - \frac{2\kappa}{\pi^{1/2}} \frac{\exp(-\kappa^2 R_c^2)}{R_c} \Bigg\}, \quad \text{for} \quad r_{i\alpha,j\beta} \le R_c. \end{aligned} \tag{3.4}$$

The damping coefficient (κ) and the cutoff radius (R_c) play an important role in the calculation by including contributions from the reciprocal and real spaces. Since these parameters are not independent of each other, care must be taken to choose an appropriate set of values for accurate calculations of total energy and forces. Following Fennell and Gezelter [78], we have used a value of 0.2 and 9 Å for κ and R_c, respectively.

Figure 3.1 presents a schematic diagram of the FEAR method showing the principal steps of our calculations. Starting with an initial random configuration $\mathbb{C}_1$, the method proceeds via χ^2 minimization to generate a new configuration $\mathbb{C}_2$ by enforcing experimental structure factor using conventional Reverse Monte Carlo (RMC) simulations. The output from this step is then fed to the next step for optimization of total energy via a gradient-descent approach. The structure of the resulting configuration $\mathbb{C}_3$ is then examined for continuation or termination. This self-consistent iterative scheme continues until the convergence criteria for each subspace optimization are met or a maximum number of iteration is reached. The total-energy optimization and the χ^2-fitting of the structure factor constitute the principal components of the method, and are indicated in Fig. 3.1 by the loop: $2 \rightarrow 3 \rightarrow 4 \rightarrow 2$. In the next section, we apply this method to a-SiO_2 and a-Si, and discuss the results in details.

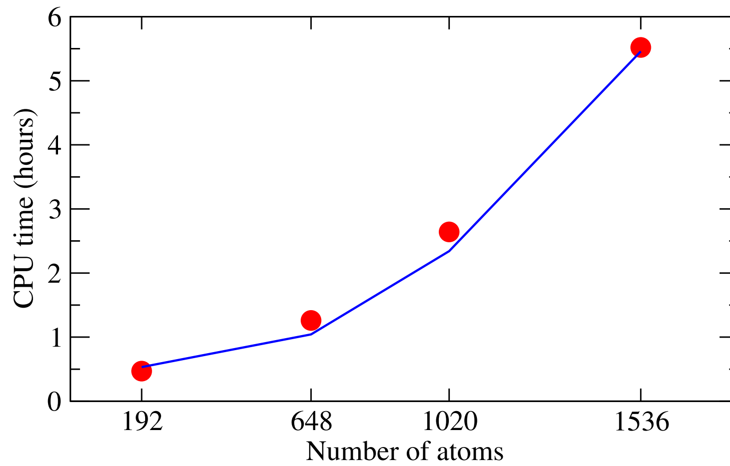

Figure 3.2: Scaling of total CPU time (red circles) vs. system size in FEAR simulations. A least-square fit of the data with a quadratic polynomial is shown as a blue curve.

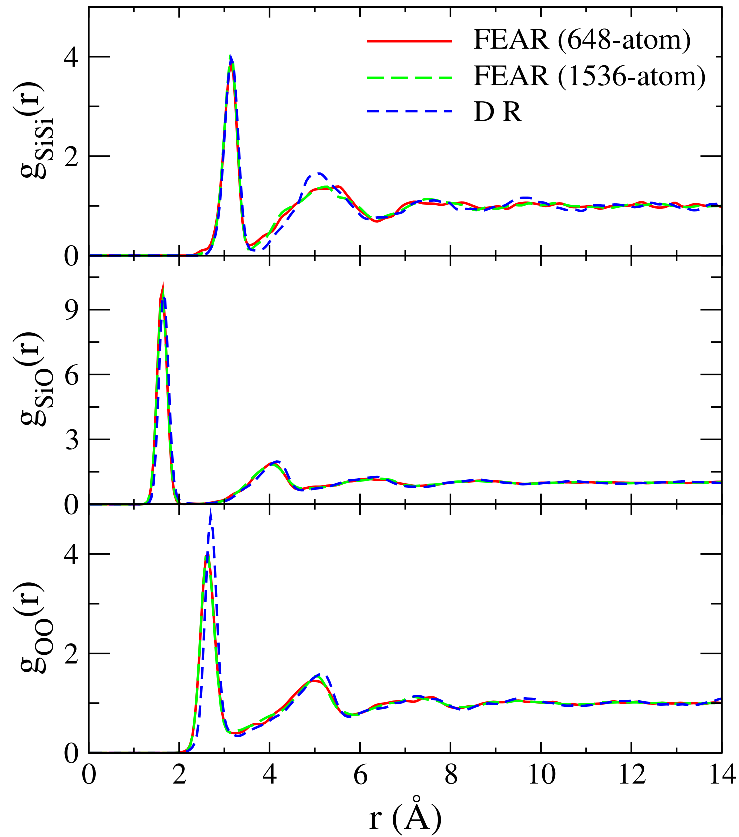

Figure 3.3: Partial pair-correlation data for a-SiO_2 models from FEAR simulations. The corresponding data (dashed blue curve) for a DR model from [85] are included for comparison.

3.3 Results and Discussion

3.3.1 Amorphous Silica (a-SiO_2)

In this subsection, we present results for a-SiO_2 from FEAR simulations. To this end, we use total neutron static structure factor from [79] which is then coupled with the total-energy BKS functional to generate a-SiO_2 models consisting of 192, 648, 1020 and 1536 atoms. Starting with a random configuration with an experimental density of 2.20 $g\,cm^{-3}$ for a-SiO_2, the structure factor of the model is fitted with the corresponding experimental data via RMC simulations. After 100 successful RMC moves, the total

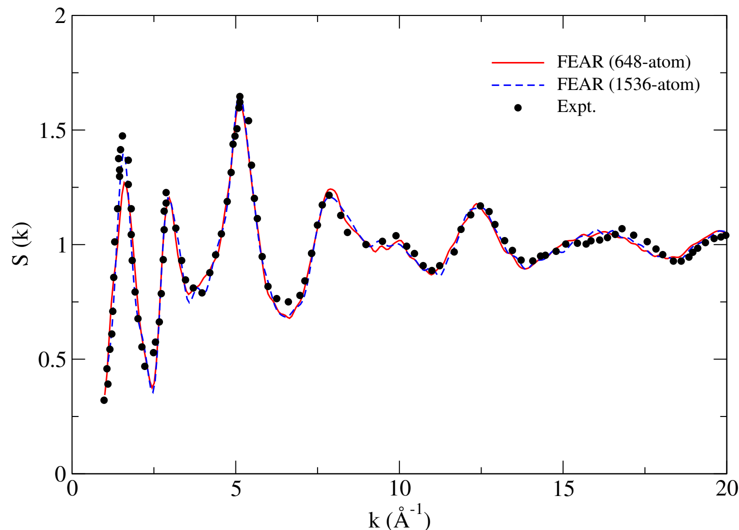

Figure 3.4: Calculated total neutron static structure factor for 648- and 1536-atom a-SiO_2 models from FEAR simulations. Experimental data from [79] are shown as solid circles.

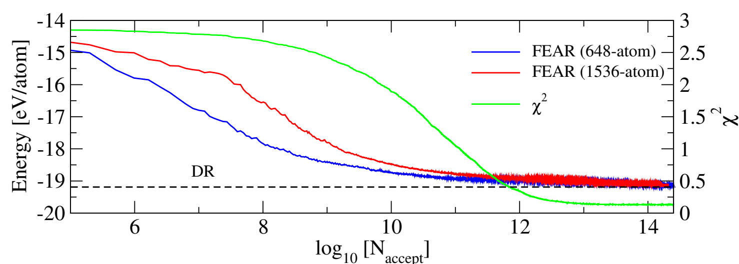

Figure 3.5: Total energy (of a-SiO_2) and the cost function χ^2 vs. RMC steps during FEAR simulations. The horizontal line corresponds to the energy of a DR model using the BKS potential for comparison.

energy and forces on the atoms are calculated (using a single force call) and the atoms are displaced along the direction of forces. This 2-step process is then repeated until the convergence criteria for χ^2 and the total energy are satisfied. Analysis of χ^2 and total energy suggest that approximately 3×10^4 force calls are sufficient for FEAR to converge

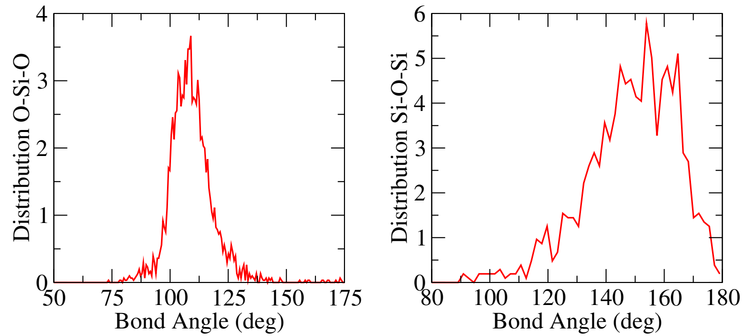

Figure 3.6: Bond-angle distributions of a 1536-atom model of a-SiO_2 from FEAR calculations. The average and width of the distributions are listed in Table III.

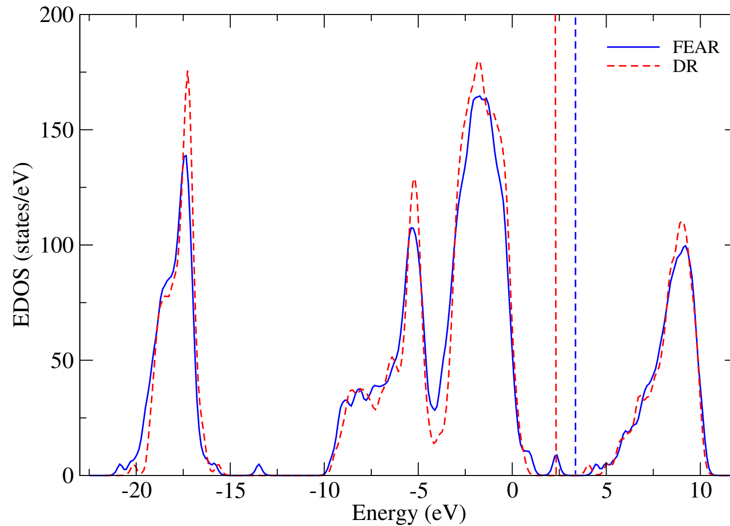

Figure 3.7: Electronic density of states (EDOS) for a 192-atom model of a-SiO_2 obtained from FEAR simulations. The corresponding result from a DR model is included for a comparison. Fermi levels are indicated as vertical lines at 2.4 eV (DR) and 3.4 eV (FEAR).

to a reasonable accuracy of $\delta\chi^2 \approx 10^{-4}$ and δF$\approx$ 0.02 eV/Å for system sizes we have studied so far.

To estimate the overall computational cost of the method, we have calculated the total CPU time for several system sizes, and compared the results with those obtained from

classical and *ab initio* MD simulations reported in [80, 81]. In Fig.3.2, we have plotted the CPU time for N = 192, 648, 1020 and 1536 atoms. While both RMC and force calculations can be implemented in an order-N manner (see note [82]), we made no attempts to obtain such improved scaling at this time in an effort to examine the usefulness of this approach in this exploratory study. Thus, the CPU time for a run has been observed to scale quadratically with the system size. This is indicated in Fig. 3.2 by a least-square fit of the data using a quadratic polynomial. Despite this quadratic scaling of CPU time, a notable feature of the method is the parsimonious use of gradient information for structural optimization. FEAR makes significantly fewer force calls than conventional classical/*ab initio* MD or other gradient-based methods. A comparison of the number of force calls relaxation between FEAR and melt-quench MD (classical and *ab initio*)[80, 81] can be found in Table 3.1.

Table 3.1: Number of Force Calls and Average CPU Time in FEAR Compared With Classical and Quantum Melt-Quench Method [80, 81].

	192-atom	648-atom	1020-atom	1536-atom	CPMD (Ref[80])	Classical MD (Ref[81])
Number of force calls	3×10^4	3×10^4	3×10^4	3×10^4	27×10^4	6×10^4
CPU time (hours)	0.47	1.26	2.64	5.52		

The partial pair-correlations data for the FEAR models are shown in Table 3.2. The peak positions and bond lengths are comparable with the results from other MD models and experiments. The average coordination numbers of Si and O for the model with 1536 atoms are found to be 3.98 and 1.99, respectively. The presence of a few 3-fold (3.2 %) and 5-fold (0.45 %) silicon and isolated (2.7 %) oxygen atoms can be attributed to the BKS potential that lacks the three-body term[74]. None of the FEAR models shows any chemical disorder or heteropolar bonding.

Table 3.2: Peak Positions of FEAR Model Compared With Other MD Models and Experiments (Expt.).

Peak position (Å)			
atom-atom	FEAR	MD (Ref[80])	Expt.(Ref[83])
Si-Si	3.15	3.10	
Si-O	1.62	1.62	1.610± 0.050
O-O	2.64	2.64	2.632± 0.089

The total structure factor $S(k)$ is compared to the neutron diffraction experiments from Ref. [79], and is shown in Fig. 3.4. The origin of the peaks in $S(k)$ can be inferred from partial structure factors. The second peak in Fig. 3.4 arises from Si–Si and O–O correlations with a partial cancellation from the Si–O anti-correlations. The third and fourth peaks receive contributions of Si–Si, Si–O and O–O correlations. The first peak for both the models is small compared to the experiment which can be attributed to finite-size effects in the intermediate range order [84].

In Fig. 3.5, we have shown the variation of the cost function (χ^2) and BKS energy per atom during FEAR simulations. The horizontal line in the plot corresponds to the BKS energy for a 648-atom model obtained from the decorate-and-relax approach described

elsewhere [85]. The BKS energy, for both 1536- and 648-atom models, is close to -19.15 eV/atom, which is comparable to -19.18 eV/atom from the corresponding DR model. The use of atomic forces or gradient information improves the quality of structure.

The bond-angle distributions for the model with 1536 atoms are plotted in Fig. 3.6. The distribution of ∠O-Si-O shows that the silicon-centered O-Si-O angles are tetrahedral in character with an average value of 109.5° and a full width (at half maximum) of 15.6°. These values are consistent with the experimental data reported by Mozzi and Warren [86]. The corresponding values for ∠Si-O-Si are found to be 154.3° and 27.8°, respectively. The average value of ∠Si-O-S is about 6.4% higher than the experimental value of 144°, and the value obtained from other theoretical models [80, 84]. This deviation, however, is not surprising, and is generally attributed to the lack of 3-body interaction in the BKS potential [87]. Since Si-O-S angles involve two neighboring tetrahedra connected via a bridging oxygen atom at a common vertex, it is difficult for the BKS potential to produce this delicate geometrical arrangement accurately via 2-body interactions only. A full comparison of FEAR results with experimental data and other theoretical models are provided in Table 3.3.

Table 3.3: Bond-Angle Distributions From FEAR, MD and DR Models.

Bond Angle (deg)				
	FEAR	MD ([80])	Expt. ([86])	DR ([79]
O-Si-O	109.5 (15.6)	109.6 (10)	109.5	109.5 (9)
Si-O-Si	154.3 (27.8)	142.0 (25)	144 (38)	140 (25)

Table 3.4 presents the number of irreducible ring statistics for the models with 192, 648, and 1536 atoms using the I.S.A.A.C.S program [26]. The presence of only even-member rings implies the absence of chemical disorder in the network.

Table 3.4: Ring Statistics of a-SiO_2 From FEAR Models.

Ring size (n)	4	6	8	10	12	14	16	18
192-atom	0	7	9	26	17	28	16	12
648-atom	5	12	36	57	80	109	53	42
1536-atom	6	24	108	167	195	215	148	96

The structures obtained from FEAR have been relaxed using the density-functional code (VASP) using a local-density approximation (LDA) and the LDA energies have been found to be comparable with those obtained from the DR model[85]. The electronic density of states (EDOS) for a 192-atom a-SiO_2 is shown in Fig.3.7. The EDOS is comparable with the results obtained by Sarnthein and co-workers [81] and hence with the X-ray photoemission spectra (XPS)[88] in the sense that the states are well reproduced. There are three distinct regions of occupied states. The states about -18 eV are oxygen 2s states, while the one between -10 eV and -4 eV are the bonding states between Si sp^3 hybrids and O 2p orbitals. The highest occupied states in valence band about -4 eV are the O 2p states and the lowest unoccupied states of conduction band comprise of anti-bonding states. However, the band gap of 3.96 eV is underestimated compared to 4.8 eV of that

obtained from MD calculation [81] and the experimental value of 9.0 eV [89]. This is to be expected from LDA DFT calculations.

Finally, to verify the reproducibility of the method, we have generated 20 configurations of 192- and 648-atom models, and 10 configurations of 1020- and 1536-atom models from different random starting configurations. Approximately, 90% of final configurations have been observed to have almost identical structural and electronic properties. The configuration fluctuations of various physical observables are found to be within the statistical limits, which ensure the reproducibility and consistency of the FEAR method.

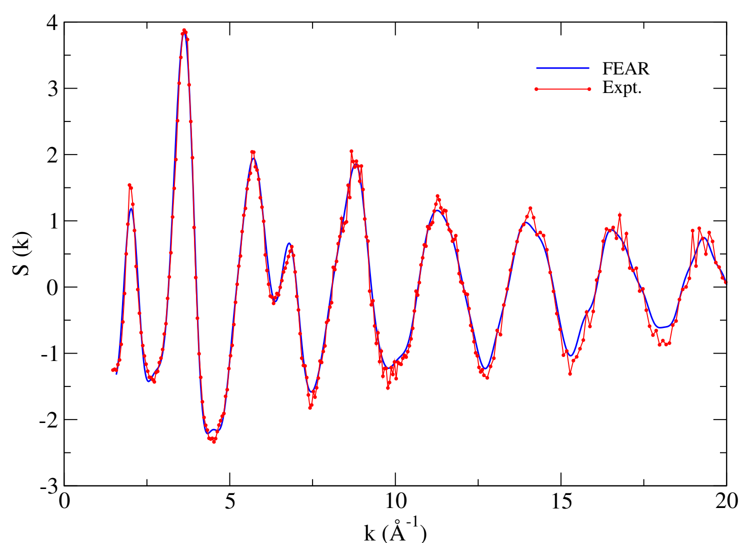

Figure 3.8: A comparison of FEAR structure factor for a 216-atom model of *a*-Si with the experimental data from Ref. [32].

3.3.2 Modeling Amorphous Silicon (*a*-Si)

We have also employed FEAR to model structure of *a*-Si starting from a random configuration with 216 atoms. The results of our calculations are plotted in Figs. 3.8-3.12. Figure 3.8 shows the structure factor obtained from a 216-atom FEAR model of *a*-Si

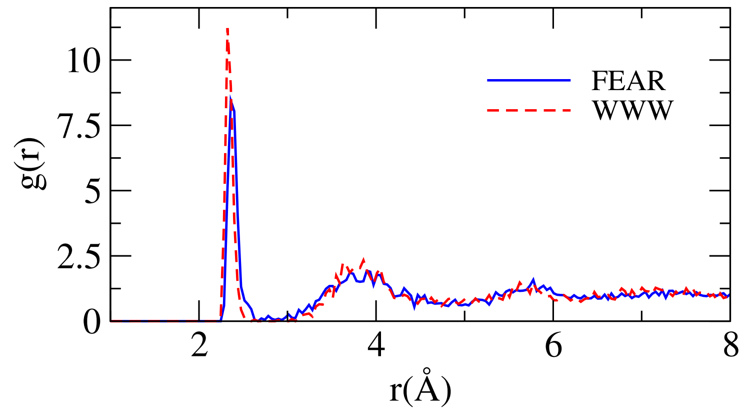

Figure 3.9: Pair-correlation data (blue) for a 216-atom model of *a*-Si obtained from FEAR. The corresponding data (red) for a WWW model is also presented here for a comparison.

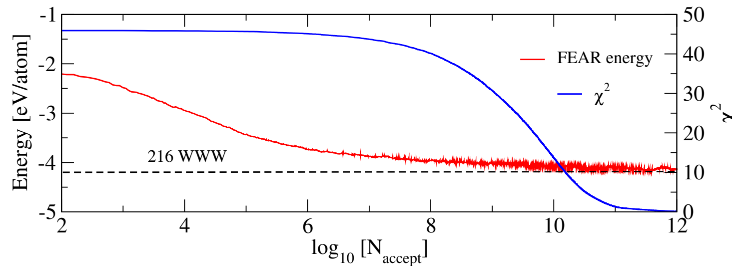

Figure 3.10: The variation of χ^2 and EDIP energy during FEAR simulations. The dashed line is the EDIP energy for a WWW model with an identical size and the number density.

along with the experimental X-ray diffraction data from [32]. It is evident from Fig. 3.8 that the structure factor agrees very well with the experimental data except for a few points near the first peak. This is also reflected in the correlation data in real space in Fig. 3.9, where the pair-correlation function of the FEAR model is compared with the same from a WWW model.

The cost function χ^2 and the total EDIP energy is shown in Fig. 3.10. The energy is compared to the 216-atom *a*-Si WWW model which is 4.199 eV (shown by dashed line). This shows that in FEAR, the energy is minimized together with the structural refinement.

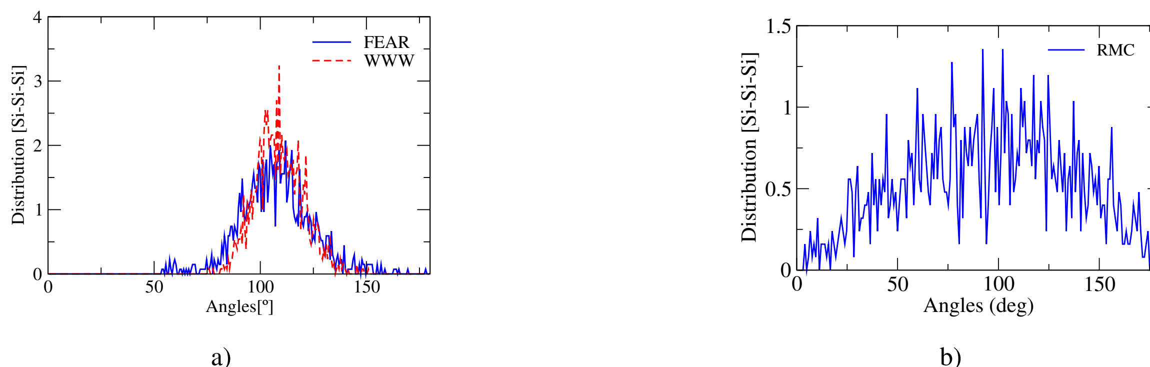

Figure 3.11: (a) The bond-angle distribution for a 216-atom model of *a*-Si using FEAR (solid line) and a WWW model (dashed line). (b) The bond-angle distribution for a 216-atom '*a*-Si model' from RMC simulations using experimental structure factor only. The approximate semi-circular distribution is a characteristic feature of *unconstrained* RMC.

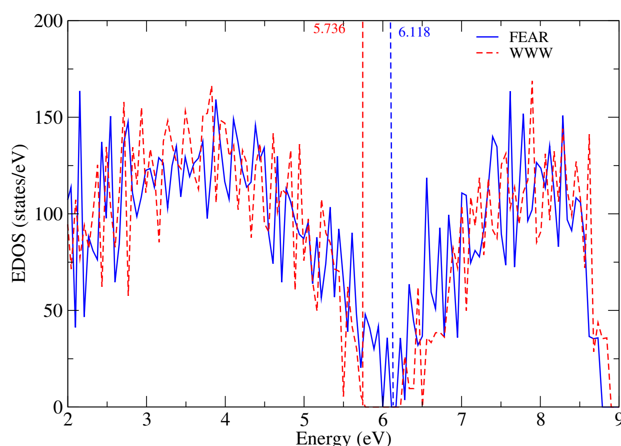

Figure 3.12: Density of electronic states of *a*-Si using VASP from FEAR (blue) and WWW (red) models. The corresponding Fermi levels are indicated as vertical lines at 6.1 eV (FEAR) and 5.7 eV (WWW).

The bond-angle distribution is shown in Fig.4.5a where the tetrahedral geometry is retained compared to the WWW model of identical number of atoms. The corresponding bond-angle distribution using RMC is shown in Fig.4.5b where the peaks are highly underestimated and the distribution is broad without tetrahedral peak. We relaxed the

structure obtained from FEAR using VASP and found the energy minimum to be -5.18 eV/atom compared to -5.23 eV/atom of the VASP relaxed WWW model. This shows that the LDA energies are comparable. In Fig.3.12, the electronic density of states for the FEAR model is compared with the same from a VASP-relaxed WWW model. The Fermi energies are shown by the vertical dashed lines. As compared to RMC and constrained RMC [62], the EDOS is in better agreement with optical measurements. The FEAR model exhibits the presence of several defect states within the gap, which mostly arise from coordination defects. This is expected in view of the fact that approximately 10% of total Si atoms have a coordination number, which is different from 4. This coordination number is better compared to the constrained RMC (88%)[62] and MD Quench from melt using EDIP and Tersoff potentials [90, 91]. The EDIP for Si overestimates the five-fold bond in Si which is evident in our FEAR calculation with almost 8% 5-fold Si present in the network [90]. These floating bonds, clutter the gap and form defects states that closes the gap. The presence of these defect states, and the use of the LDA that is known to underestimate the optical gap, explains the small gap in the electronic density of states.

3.4 Conclusion

In this chapter, we have studied an approach, called force-enhanced atomic refinement (FEAR), to model complex amorphous solids by combining experimental structure factor with periodic usages of gradient information from a total-energy functional. The approach consists of employing experimental scattering data to generate an ensemble of possible structural solutions via Reverse Monte Carlo simulations, which is followed by further refinement of the RMC solutions using gradient information from a total-energy functional. Since conventional RMC cannot describe a 3-dimensional structure uniquely, and its constrained counterpart with additional structural information often transforms the original unconstrained problem to a difficult multi-objective

optimization program, the emphasis on the present approach has been to develop a method that retains the simplicity of RMC and yet overcomes the problem of non-uniqueness in structural determination via the economical use of a total-energy functional and forces. The approach can be viewed as a 'predictor-corrector' method for structural refinement. Atomistic configurations predicted by RMC are corrected at regular interval via the optimal usage of gradient information or forces from a total-energy functional. This enables FEAR to track solutions in the manifold of the solution space that jointly satisfies experimental structure-factor data and the total energy of the system. In this exploratory study, we have demonstrated using two archetypal examples of amorphous solids (*a*-Si and *a*-SiO_2) that the method performs on a par with the traditional MD simulations or other gradient-based relaxation approaches even at an elementary level of its implementation.

We have successfully implemented FEAR to model *a*-SiO_2 and *a*-Si. Structural and electronic properties of the FEAR models are produced as accurately as possible within the limit of the potentials and experimental input data.

4 Inversion of Diffraction Data for Amorphous Materials

The work presented in this chapter is published in **Pandey, A., Biswas, P., and Drabold, D. A. (2016). Inversion of diffraction data for amorphous materials. Scientific Reports, 6, 33731.**

4.1 Background and Introduction

On the eve of the First World War, William Lawrence Bragg and his father, William Henry Bragg, exposed crystalline solids to X-rays and discovered what we now call "Bragg diffraction", strong reflection at particular incident angles and wavelengths. These "Bragg peaks" were sharply defined and, when analyzed with a wave theory of the X-rays, led to clear evidence of order in the crystalline state[1]. By analyzing the diffraction angles at which the peaks appeared and the wavelength of the X-rays, the full structure of the crystal could be ascertained. In the language of modern solid state physics, the X-ray structure factor of a single crystal consists of a sequence of sharp spikes, which are broadened in a minor way by thermal effects. The information obtained from this palisade of delta functions, arising from a crystal, is sufficient for the determination of atomic structure of crystal uniquely. The rapid development of X-ray Crystallography in the past several decades had made it possible to successfully determine the structure of complex protein molecules, with more than 10^5 atoms, leading to the formation of a new branch of protein crystallography in structural biology[2].

In contrast with crystals, amorphous materials and liquids have structure factors that are smooth, and thus contain far less specific information about structure. The lack of sharp peaks principally originates from the presence of local atomic ordering in varying length scales, and no long-range order in the amorphous state. The resulting structure factor is one-dimensional and is effectively a sum rule that must be satisfied by the three-dimensional amorphous solids. This presents a far more difficult problem of

structural determination of amorphous solids that requires the development of new tools and reasoning to obtain realistic structural models. A natural approach to address the problem is to carry out computer simulations, either employing molecular dynamics or Monte Carlo, with suitable interatomic potentials. We have called this approach the "simulation paradigm"[23] elsewhere. By contrast, the other limit is to attempt to invert the diffraction data by "Reverse Monte Carlo" (RMC) or otherwise without using any interatomic potential but information only [62, 65]. This we have called the "information paradigm"[23]. The information paradigm in its purest form produces models reproducing the data using a random process. These models tend to be maximally disordered and chemically unrealistic. The information paradigm is closely related to the challenge of Materials by Design[92, 93], for which one imposes external constraints to incorporate additional information on a model to enable a set of preferred physical properties that are of technological utility.

Neither paradigm is ideal, or even adequate. The simulation paradigm is plagued by severe size and time-scale limitations that misrepresent the real process of forming a glass, not to mention imperfect interatomic interactions. Despite the development of hardware and software technology for distributed-shared-memory computing, the lack of appropriate force-fields or interatomic interactions has been a major obstacle in computer simulations of complex multinary glasses. For amorphous materials with no or weak *glass-forming* ability, either approach is rather desperate, and leads to the formation of unrealistic models with too many structural defects in the networks. In this paper we introduce *ab initio Force Enhanced Atomic Refinement* (AIFEAR). A preliminary trial of the algorithm using only empirical potentials is discussed in Chapter 3[94].

Others have undertaken related approaches [24, 25, 47, 67, 68, 95–97] as discussed in Chapter 3. These methods have all contributed significantly to the field, yet they have limitations such as employing empirical potentials of limited reliability[24, 94], or

unacceptable convergence properties[25]. A general and successful framework for inverting solid state diffraction data does not exist. AIFEAR is a major step toward this important goal.

4.2 Methodology

In this section, we discuss the AIFEAR method in detail. We present the AIFEAR, RMC and melt-quench methods adopted for amorphous silicon (a-Si) and silver-doped germanium selenide systems.

4.2.1 *Ab Initio* Force-Enhanced Atomic Refinement (AIFEAR)

If $V(X_1 \ldots X_n)$ is the energy functional for atomic coordinates $\{X_i\}$ and χ^2 measures the discrepancy between diffraction experiment and theory, we seek to find a set of atomic coordinates $\{X_i\}$ with the property that V=minimum and χ^2 is within experimental error. In other words, AIFEAR jointly minimizes the configurational energy V and[12, 65]

$$\chi^2 = \sum_i \left[\frac{F_E(k_i) - F_M(k_i)}{\sigma(k_i)} \right]^2, \tag{4.1}$$

where $F_{E/M}(k_i)$ is the experimental/model structure factor, and $\sigma(k_i)$ is the error associated with the experimental data for wave vector k_i. To undertake this program, (i) we begin with a random model, (ii) invoke M RMC accepted moves followed by N conjugate-gradient steps to optimize the total energy. We have found $M = 1000$ and $N = 10$ to be satisfactory for the materials of this paper. The process (ii) is repeated until the desired accuracy of $\delta\chi^2 \approx 0.1$ and, a force tolerance of $\delta f \approx 0.02$ eV/Å is attained. All that is required are RMC and total-energy codes and an appropriate driver program connecting them.

AIFEAR avoids the problem of relative weighting of V and χ^2 in a penalty or target energy functional as in hybrid approaches developed elsewhere [24][98]. If the density of the material is unknown, it is straightforward to carry out the simulation at zero pressure

(with variable cell geometries) in the CG loop, and simply pass the modified supercell vectors back to the RMC loop.

4.2.2 Amorphous Silicon (*a*-Si)

We began by preparing three 216-atom models of *a*-Si using (1) RMC, (2) melt-quench, and (3) AIFEAR. Initially, conventional RMC (i.e. without any constraint) was performed using the RMCProfile software [27] for a *random* starting configuration of 216-atom *a*-Si with a cubic box of side 16.281 Å corresponding to the density 2.33 g.cm^{-3} [99]. The maximum step length of the RMC moves for Si atoms is chosen to be 0.05 Å. In a parallel simulation, the same starting configuration is taken through a process of melt-quench using the density-functional code SIESTA [16] with single-ζ basis under Harris functional scheme [16] within the local density approximation. The total-energy and force calculations are restricted to the Γ point of the supercell Brillouin zone. After melting at 2300 K, the liquid structure was quenched to 300 K at a rate of 240 K/ps. Each step was followed by the equilibration of the system for 2000 time steps. Finally, the configuration is subjected to *ab initio* FEAR simulations with the same Hamiltonian and "data". The diffraction data from Ref. [7] were employed in RMC and AIFEAR. To ensure the reproducibility of the method, we have modeled 10 *a*-Si models starting from random configurations and the models yielded 4-fold coordination exceeding 96%.

4.2.3 Chalcogenide Glasses: $(GeSe_3)_{1-x}Ag_x$ [x=0.05 and 0.077])

We employ the same scheme as for *a*-Si, but with *ab initio* interactions from the plane-wave DFT code VASP[100–102], using projected augmented plane waves (PAW) [19] with Perdew-Burke-Ernzerhof (PBE) exchange-correlation functional [21] and a plane-wave cutoff of 312.3 eV. All calculations were carried out at Γ point. For 5% and 7.7% Ag doped systems, 135 and 108 atoms were taken in a unit cell of length 15.923 Å and 15.230 Å, respectively. These values correspond to the densities of 4.38 g.cm^{-3} and

4.04 g.cm^{-3} for the models with 5% and 7.7% Ag, respectively. For $x = 0.050$, both the structure-factor data and density of 4.38 g.cm^{-3} are taken from the work of Piarristeguy *et al.* [103]. For $x = 0.077$, we have used the the pair distribution function (PDF) data provided by Zeidler and Salmon[104], and a density of 4.04 g.cm^{-3} was obtained from a zero-pressure conjugate gradient relaxation using VASP. For completeness, we have also studied a melt-quench models.

The 5% Ag-doped $GeSe_3Ag$ *ab initio* FEAR models are compared to the melt-quench model of the identical system of Piarristeguy and co-workers [103]. The melt-quench model of 7.7% Ag-doped $GeSe_3$ model is prepared by melting the same starting configuration at 1400 K for 10,000 steps followed by a quenching to 300 K at the rate of 100 K/ps, and then by equilibrating at 300 K for another 5000 steps. To estimate the density of the equilibrated system, the volume of the simulation cell was relaxed. A final relaxation at zero pressure was employed, which yielded a density of 4.04 g.cm^{-3}. Throughout the calculations, we have used a time step of 1.5 fs.

4.3 Application of AIFEAR

The method is applied to two very different systems: amorphous silicon and two compositions of a solid electrolyte memory material silver-doped $GeSe_3$.

4.3.0.1 Amorphous Silicon (*a*-Si)

To illustrate the efficacy of this new approach, we begin with a persistently vexing problem: the structure of amorphous Si is particularly difficult because the network is over-constrained[35, 105] and it is not a glass former. Structural and electronic experiments reveal that coordination defects in good quality material have a concentration less than a part in 1000. As such, a satisfactory model should have at most a few percent (or less) defects. Inversion methods like RMC and *ab initio* melt-quench both produce

unsatisfactory models with far too many coordination and strain defects compared to experiments.

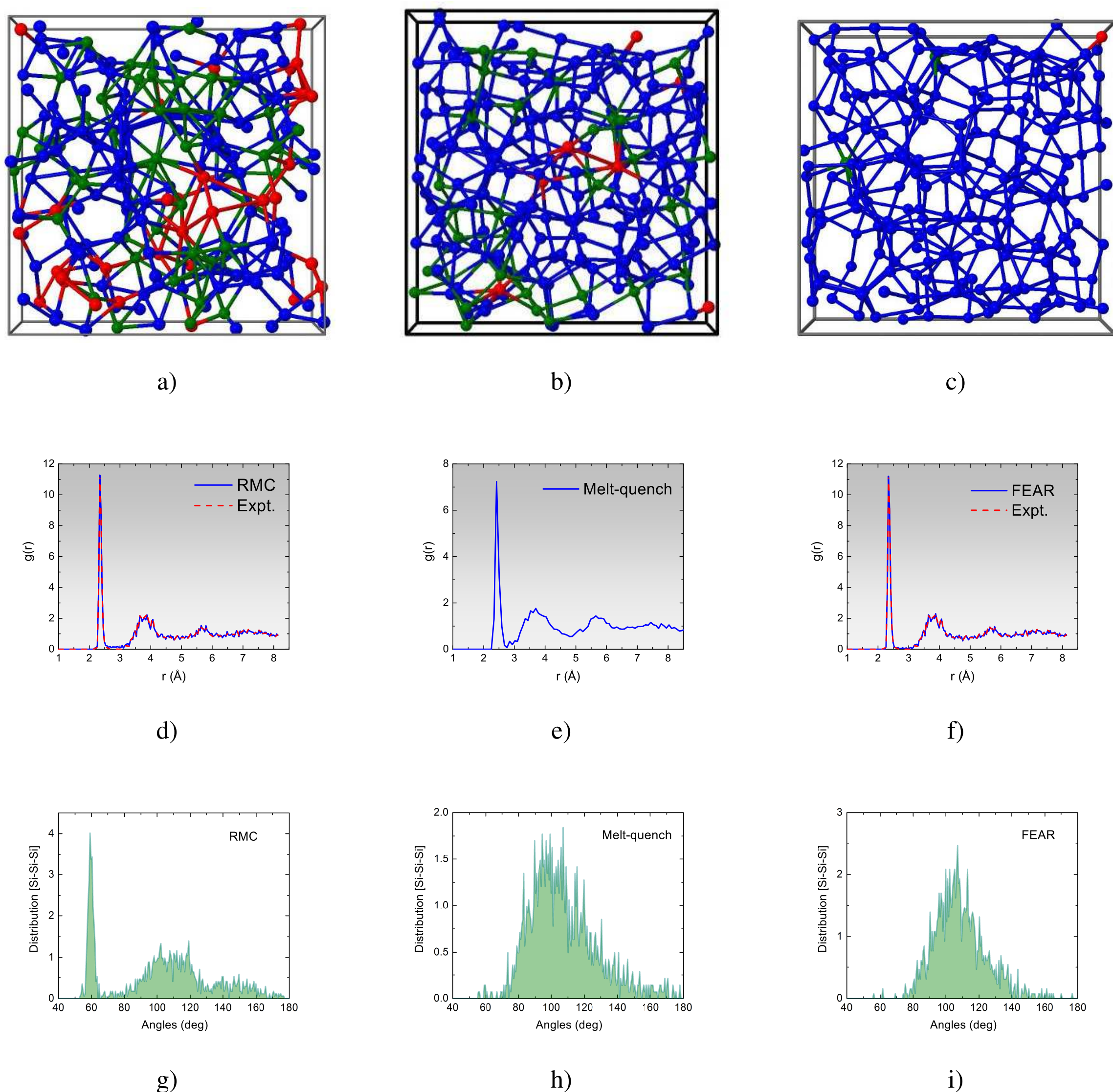

Figure 4.1: Top: A 216-atom model of *a*-Si obtained from (a) RMC, (b) melt-quench and (c) *ab initio* FEAR simulations. Silicon atoms with a coordination number of 3, 4 and 5 are shown in green, blue and red colors, respectively. Center: The radial distribution function (RDF) for the (d) RMC, (e) melt-quench and (f) *ab initio* FEAR models. Bottom: The bond-angle distributions for the models as indicated in the figure. For animations showing the formation of three-dimensional network structure and the corresponding evolution of the radial and coordination-number distributions follow the youtube links provided in the application section.

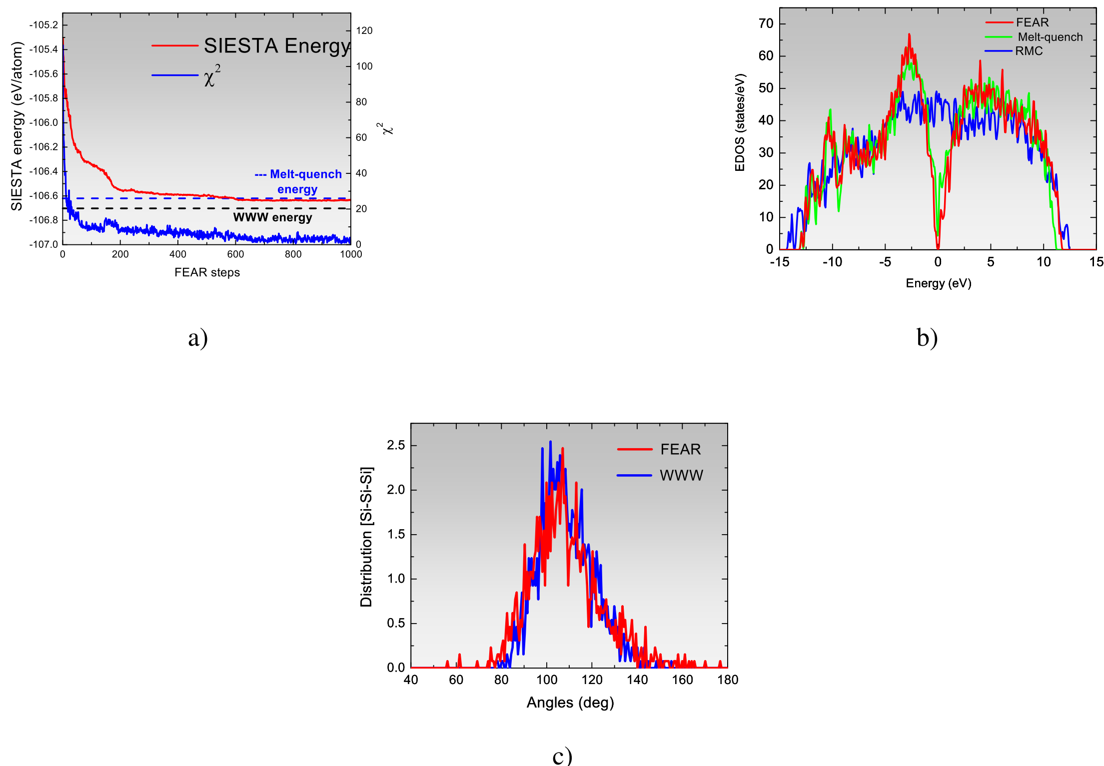

Figure 4.2: Results for 216-atom *a*-Si: (a) The variation of cost function and total energy with the number of AIFEAR steps. (b) Electronic density of states (EDOS) for RMC, melt-quench and AIFEAR models with the Fermi level at 0 eV. (c) The bond-angle distribution from AIFEAR compared to that of WWW (see Table 1 for details).

The structural properties of *a*-Si, obtained from these models, are summarized in Fig. 4.1. Details of convergence and comparison to the best available WWW model is provided in Fig. 4.2.

RMC produces a highly unrealistic model, far from the accepted tetrahedral network topology, as seen in Fig.4.1. Melt-quench, while better, still produces far too many coordination defects. By contrast, AIFEAR produces a nearly perfect structure, with 99.07% fourfold coordination, and a bond-angle distribution close to that of from a WWW model. In comparing the bond-angle distributions (from AIFEAR with that of

from WWW), one must take into account the fact that *ab initio* interactions tend to produce a slightly wider bond-angle distribution than the artificial WWW (Keating spring) interactions. The AIFEAR model has energy 0.03 eV/atom higher than the WWW model compared to 0.08 eV/atom for the melt-quench and 3.84 eV/atom for the RMC models. It suggests that the AIFEAR model is energetically stable compared to remaining two models.

We wish to emphasize that the starting configuration used in AIFEAR was *random*, so that one can logically infer that a combination of atomic-radial-correlation data and DFT interactions leads to an almost perfect tetrahedral network as illustrated in Fig. 4.1. Table 1 lists the key structural properties of the model, along with the total energy per atom.

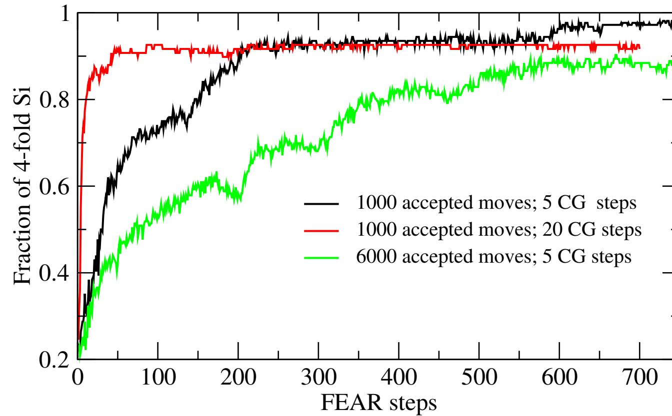

Figure 4.3: The evolution of four-fold Si atoms during FEAR simulation for three different combinations of the number of accepted moves (M) and number of CG steps (N). (black) M=1000 and N=5, (red) M=1000 and N=20 and (green) M=6000 and N=5.

To illustrate the choice of M and N steps on the convergence of the structure, we have plotted the evolution of the four-fold coordinated Si atoms in FEAR for various combinations of M and N. The convergence for three different combinations are shown in Fig.4.3. The structure is abruptly trapped into a local minimum for a higher value of CG

steps (N=20). The higher number of RMC accepted moves (M=6000) generates a structure with a large number of defects. For the efficient use of algorithm, we suggest the optimum value for M as anything between 100 and 2000 and for N any value between 3 to 10. Although, there is no significant change in the structure by a choice within this range, a short quick run with the extreme values will help user guess the appropriate ones.

An animation of the convergence of AIFEAR showing the formation of a nearly perfect tetrahedral network as the simulation proceeds with the disappearance of coordination defects can be found in a link: *https://youtu.be/B6Y2lv75V6s*. The evolution of radial distribution function and coordination number during AIFEAR can be visualized in the links: *https://youtu.be/M0HERVDMMN4* and *https://youtu.be/hl1H_wBgo54*.

Table 4.1: Total Energy and Key Structural Properties of *a*-Si Models. The Energy per Atom is Expressed With Reference to the Energy of the WWW Model.

	RMC	Melt-quench	AIFEAR	WWW
4-fold Si (%)	27	80	99.07	100
SIESTA energy (eV/atom)	3.84	0.08	0.03	0.00
Average bond angle (RMS deviation)	101.57° (31.12°)	107.04° (20.16°)	108.80° (14.55°)	108.97° (11.93°)

4.3.0.2 Chalcogenide Glasses: $(GeSe_3)_{1-x}Ag_x$ [x=0.050 and 0.077])

For a challenging and timely example, we have also studied the solid electrolyte material $Ag_x(GeSe_3)_{1-x}$. This is a chemically complex system with important applications

to conducting bridge computer FLASH memory devices, which are of considerable fundamental and technological interest.

The melt-quench model (in Fig. 4.4a) shows significant discrepancies with experiments: the first sharp diffraction peak (FSDP) near 1 $Å^{-1}$ is absent, and there are significant inconsistencies in the structure factor at high k values. The FSDP is an indicator of medium range order, a signature of structural correlations between the tetrahedral GeSe structural building blocks of the glass. By contrast, the AIFEAR model captures all the basic characteristics of the structure factor, including the FSDP (in fact, it slightly *overfits* the FSDP). We show that the method has similar utility in either real or k space, using $S(k)$ for the first composition and $g(r)$ for the second. Figure 4.4 shows the structure factors and radial distribution functions obtained from AIFEAR and melt-quench simulations, and compares with the experimental data from neutron diffraction measurements [103, 104].

The GeSeAg systems are of basic interest as solid electrolytes. One of the most interesting questions pertains to the dynamics of Ag atoms, which are sufficiently rapid that they can be tracked even in first-principles molecular-dynamics simulations [107]. The fast Ag dynamics have led to the invention of conducting bridge Random Access Memory [108, 109]. As this dynamics appears to be of trap-release form [107], the structure, including features like medium range order, and associated energetics may be expected to play a key role in the silver hopping. The 7.7% Ag composition is near to a remarkable and abrupt ionic mobility transition [110, 111]. Dynamical simulations are currently underway to determine the role of the structure in this dynamics.

The following features of $Ag_x(GeSe_3)_{1-x}$ glasses have been observed in the AIFEAR model: 1) The Ge-Se correlation is not affected by an increase in Ag content: $Ge(Se_{1/2})_4$ tetrahedra remain the fundamental structural units in the network. 2) Ge-Ge correlations, greatly affected by Ag doping, are revealed by the shift in Ge-Ge nearest-neighbor

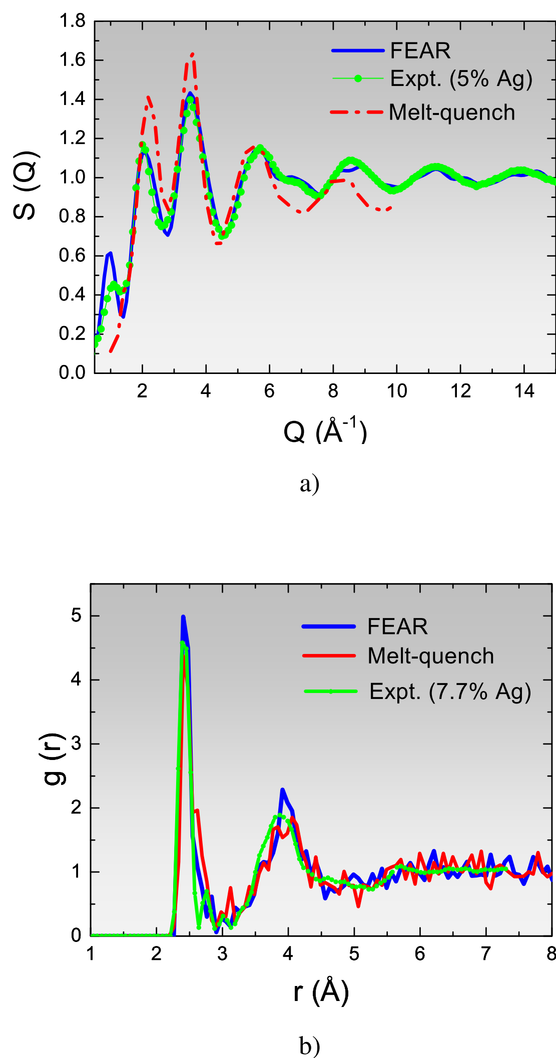

Figure 4.4: (a) Structure factors of $(GeSe_3)_{1-x}Ag_x$ [x=0.05] from *ab initio* FEAR. Experimental data, from neutron diffraction measurements, are shown for comparison [103]. Melt-quench data are from Pradel *et al.*[103] (b) The radial distribution function of $(GeSe_3)_{1-x}Ag_x$ [x=0.077] from *ab initio* FEAR and melt-quench simulations. Experimental RDF shown here are from Zeidler *et al.* [104].

distance from 3.81 Å in Ag=0% [103] to 2.64 Å and 2.56 Å in Ag=5% and Ag=7.7% respectively, supporting the argument of Ag being the network modifier. 3) The Ag-Se correlation peak is near 2.66 Å for both the systems, which is consistent with the

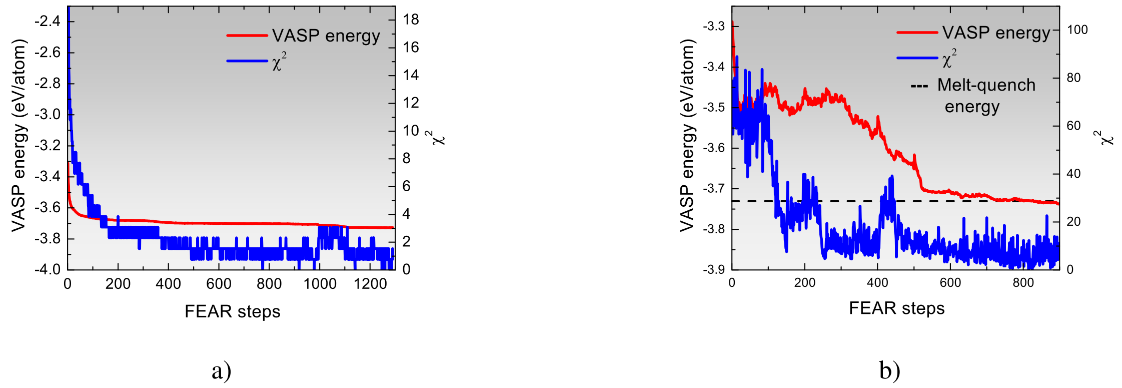

Figure 4.5: Total energy per atom and the cost function (χ^2) versus AIFEAR steps for two models with (a) 5% and (b) 7.7% Ag-doped $GeSe_3$. The melt-quench energy for the 7.7% Ag model is indicated for comparison.

experimental work of Zeidler [104] and others [103]. 4) The Se-Se coordination number for 5% and 7.7% Ag are 1.12 and 0.83 (0.81 from experimental data [104]), respectively. This is consistent with the observed phenomena of decrease in Se coordination with the increase in Ag concentration [103].

Beside retaining the important chemical features of the network, the AIFEAR model is superior to the melt-quench model by the manifestation of a prominent FSDP (cf. Fig. 4.4a), a signature of medium range order in these materials. Absence of the FSDP indicates the lack of structural correlations in the $Ge(Se_{1/2})_4$ tetrahedra, which is less prominent for low Ag concentration. Also, the energy of the AIFEAR model for x=0.077 is 0.02 eV/atom less than the melt-quench model (see Fig. 4.5b).

It is important and promising that in the GeSeAg systems, as in *a*-Si, AIFEAR is not a greedy optimization scheme, as it is evidently able to unstick itself (for example in Fig.4.5b) near 400 steps, there is a dramatic and temporary increase in χ^2, which then enabled the system to find a new topology which enabled further reduction of both χ^2 and E. A similar, if less dramatic, event is indicated in Fig.4.5a around step 1100). The

Monte-Carlo moves robustly explore the configuration space and are not so prone to getting trapped as MD simulations, and yet the chemistry is properly included in the *ab initio* relaxation loop.

We have included a comparison of the number of force calls in the various simulations in Fig. 4.6. It is evident from Fig. 4.6 that AIFEAR offers a significant computational advantage, with fewer force calls to the expensive *ab initio* codes.

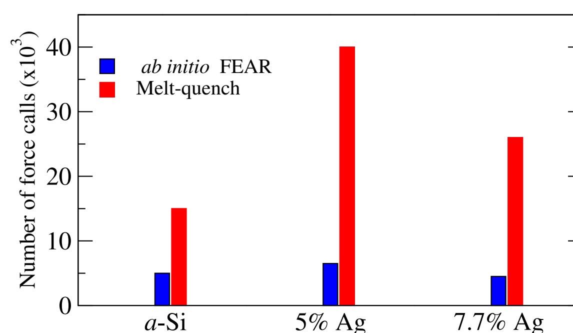

Figure 4.6: Comparison of number of force calls in *ab initio* FEAR with melt-quench simulations for *a*-Si, and 5% and 7.7% Ag-doped $GeSe_3$. Note that the number of force calls in melt-quench simulations vary considerably for different systems.

4.4 Conclusion

In conclusion, we have introduced a new and practical method that enables the joint exploitation of experimental information and the information inherent to *ab initio* total-energy calculations, and a powerful new approach, to the century-old problem of structural inversion of diffraction data. The method is simple and robust, and independent of the systems, the convergence of which has been readily obtained in two highly distinct systems, both known to be challenging and technologically useful. By direct calculation, we show the network topology implied by pair correlations and accurate total energies: an essentially fourfold tetrahedral network, structurally similar to WWW models, including

the bond-angle distribution. Using only the total structure factor (or pair-correlation) data and SIESTA/VASP, we obtain models of unprecedented accuracy for a difficult test case (*a*-Si) and a technologically important memory material ($GeSe_3Ag$). The inclusion of *a priori* experimental information emphasized here may also be developed into a scheme to include other information for materials optimization. It is easily utilized with any interatomic potentials, including promising current developments in "machine learning" [112]. The method is unbiased in the sense that it starts from a completely random configuration and explore the configuration space of a total-energy functional aided by additional experimental information to arrive at a stable amorphous state. Beside these attributes, it requires fewer force calls to the expensive *ab initio* interactions.

5 Realistic Inversion of Diffraction Data for an Amorphous Solid: The Case of Amorphous Silicon

The work shown in this chapter has been submitted to the Physical Review B and is published in an arxiv as: **Pandey, A., Biswas, P., Bhattarai, B., and Drabold, D. A. (2016). Realistic inversion of diffraction data for an amorphous solid: the case of amorphous silicon.** *arXiv preprint arXiv:1610.00065*.

5.1 Introduction

It has long been realized that the inversion of diffraction data – extracting a structural model based upon the data at hand – is a difficult problem of materials theory. It is worth noting that the success of inverting diffraction data for crystals has been one of the profound success stories of science, even revealing the structure of the Ribosome [113]. The situation is different for non-crystalline materials. Evidence from Reverse Monte Carlo (RMC) studies [12, 61, 62, 65] show that the information inherent to pair-correlations alone is not adequate to produce a model with chemically realistic coordination and ordering. This is not really surprising, as the structure factor $S(Q)$ or pair-correlation function $g(r)$ (PCF) is a smooth one-dimensional function, and its information entropy [114] is vastly higher (and information commensurately lower) than for a crystal, the latter PCF being a sequence of sharply localized functions. It seems clear that including chemical information, *in an unbiased mode*, should aid the structure determination substantially. Others have clearly described this challenge as the "nanostructure problem" [115], and noted the appeal of including an interatomic potential. We show here that such an approach is successful, by uniting the RMC code "RMCProfile" and including chemistry in a self-consistent manner using density functional theory, but not by invoking *ad hoc* constraints. We have named this method

"Force Enhanced Atomic Refinement" (FEAR). In this chapter, we focus on the classic and persistently vexing problem of amorphous silicon.

From a practical modeling perspective, the utilization of *a priori* information by constraining chemical order and preferred coordination has improved some of the most serious limitations of RMC [47, 68, 79, 117, 118]. These constraints are externally imposed and sensible though they might be, they introduce the investigators *bias* in the modeling. In other applications, more along the lines of "Materials by Design" the point is indeed to impose conditions that the model must obey – and see if a physical realization of the desired properties may be realized. The present work is focused on trying to best understand well explored specific samples of *a*-Si.

More in the spirit of our work, many hybrid schemes have been introduced, incorporating experimental data and a penalty function scheme [24, 66]. A short review on various methods is provided in Chapter 3 and 4. The first attempt to incorporate experimental information in a first-principle approach was experimentally constrained molecular relaxation (ECMR) [25, 69]. ECMR merely alternated full relaxations of fitting pair-correlations (via RMC) and energy minimization. When this process converged (as it did for the case of glassy $GeSe_2$), an excellent model resulted [25]. The problem was that this scheme often failed to converge. We therefore amended ECMR and introduced *ab initio* force-enhanced atomic refinement (*ab initio* FEAR) [116]. In effect we alternate between partially fitting the RDF (or structure factor) using RMC and carrying out partial relaxations using *ab initio* interactions, as we explain in detail in References [94, 116]. By carrying out the iteration in "bite-sized" bits rather than iterated full relaxations as in the original ECMR, we find that the method is robust, working for silver-doped chalcogenides with plane-wave DFT and for WWW *a*-Si with SIESTA and also for forms of amorphous carbon [119].

We should clarify that in our previous work on *a*-Si [116] we used the WWW RDF as input "experimental data", whereas in this work we have used high energy X-ray diffraction data from Laaziri et al. [32]. WWW models are a fixture of the modeling community (a continuous random network of ideal four-fold coordination and involving up to 100,000 atoms [31, 48], and represent an important benchmark that a new method must handle. It is reasonably interpreted as "ideal" a-Si, with minimum strain. While the RDF of WWW and Lazirri [32] are indeed fairly similar, there are key differences as noted by Roorda and coworkers [34]. Given the high quality and precision of the experiments, we have undertaken a FEAR inversion of their data in this work.

One key assumption that we forthrightly emphasize is that the dataset of Laaziri and coworkers may be represented by a small supercell model of silicon. This is obviously an approximation, as the material must surely include some voids and damaged regions from the ion bombardment procedure from which the material was made, and of course the X-ray diffraction includes these. While we think this is a reasonable approximation, it is clear that a very large scale simulation with thousands of atoms allowing for internal surfaces and other inhomogeneities would be desirable, possibly opening up the possibility of paracrystallites [120] and other longer length scale irregularities. It is not obvious whether the RDF by itself would provide information enough to open up voids. Such computations might be undertaken with transferable potentials devised from "machine earning"[112].

5.2 Methodology

More details about FEAR can be found in Chapter 3 and 4 and elsewhere [94, 116]. To summarize, in FEAR, a *random* starting configuration is subjected to partial RMC refinement followed by partial conjugate gradient (CG) relaxation according to a chemically realistic (say DFT interaction). The two steps are repeated until both the

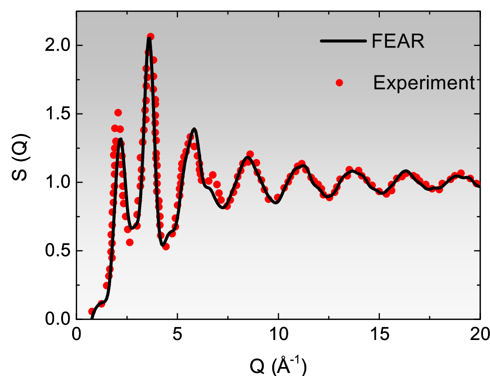

Figure 5.1: Comparison of the simulated X-ray static structure factor (black) from FEAR with the experimental diffraction data (red circle) from Ref. [32]. A 216-atom model is used to produced the simulated structure factor.

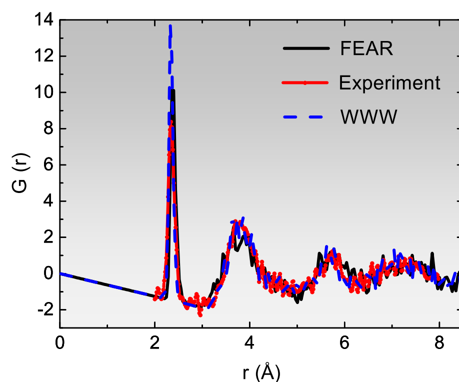

Figure 5.2: The reduced pair-correlation function of *a*-Si obtained from a 216-atom model using FEAR (black) and WWW (blue) methods. The experimental data (red) shown above are the Fourier transform of the high-energy X-ray diffraction data from Ref. [32].

structure and energy converge [94, 116]. In this work, we have carried out RMC for 500 accepted moves followed by 5 CG relaxations steps (we have tried other recipes such as 1000 and 10 moves, respectively, with similar results). This process is then repeated until convergence (namely finding coordinates both matching diffraction data and being at a

minimum of a DFT total energy). The RMC algorithm (in our case RMCProfile [27]) is used to invert the experimental data. We have so far only used diffraction data, though EXAFS and NMR are also natural datasets to attempt, and in principle multiple experimental datasets might be jointly fit while the CG relaxations enforce chemistry in the material. We employ a local-orbital basis DFT code (Siesta) [16] using the local density approximation (LDA). The cubic box edge length is 16.281 Å which corresponds with the experimental density of 2.33 gm/cm^3 (which, in the spirit of full reporting should be understood to be another *assumption*).

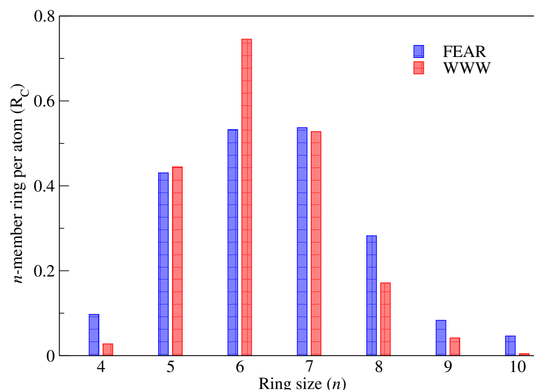

Figure 5.3: The number of *n*-fold ring per atom (R_C) for the FEAR model (blue) compared to the WWW model of same size.

5.3 Results and Discussion

In this section, we present results for *a*-Si obtained from FEAR. Since the FEAR method essentially consists of incorporating the pair-correlation data via reverse monte carlo simulations (RMC), followed by *ab initio* total-energy relaxations using the conjugate-gradient (CG) method, we also include the results from the CG-only model (e.g. from the initial random state) to evaluate the performance of FEAR with the CG method as a function of simulation time or steps. In particular, we address the structure

factor $S(Q)$, bond-angle distribution $P(\theta)$, electronic density of states (EDOS), the vibrational density of states (VDOS) and the vibrational specific heat of the FEAR models of a-Si. To examine the convergence of the method with respect to the total energy and the evolution of structure, we take a close look at the variation of the average coordination number and optical gap as a function of FEAR steps.

5.3.1 Structural Analysis

Figure 5.1 shows the structure factor of a-Si for the model configurations obtained from the FEAR along with the (annealed sample) structure-factor data of a-Si reported by Lazirri et al. [32]. Fitting was carried out in Q space. It is apparent that, while the CG-only model shows a consistent deviation from the experimental data, particularly at high Q values, the structure factor from the FEAR model compares very well with the experimental data. The only exceptions are a minor deviation of $S(Q)$ near Q=2.5 Å and 7 Å. A comparison of the $S(Q)$ data from the FEAR and CG-only models suggests that the former is superior to the latter as far as the two-body correlations of the models are concerned even though both the systems have been treated with identical *ab initio* interactions. This observation is also reflected on Fig. 5.2, where the reduced radial distribution function, $G(r) = 4\pi r n_0(g(r) - 1)$, obtained from FEAR, WWW, and X-ray diffraction experiments are plotted.

Since the pair-correlation data or structure factors of a model cannot determine a three-dimensional amorphous structure uniquely, it is necessary to examine the models further by going beyond two-body correlation functions. To this end, we have calculated the bond-angle distribution $P(\theta)$, and compared it with the results obtained from WWW, CG-only and the width of the transverse optical (TO) peak of the Raman spectrum of a-Si. Following Beeman et al. [35], we have assumed that the half-width at half-maximum (HWHM) of the Raman TO peak of a-Si is related to the average width of the bond-angle

Table 5.1: Total Energy and Key Structural Properties of *a*-Si Models. The Energy per Atom is Expressed With Reference to the Energy of the WWW Model.

	RMC	Only CG	FEAR	WWW
4-fold Si (%)	27	75	96	100
3-fold Si (%)	15	21	2	0
5-fold Si (%)	25	3	2	0
Energy (eV/atom)	3.84	0.09	0.06	0.00
Average bond angle (RMS deviation)	101.57° (31.12°)	107.31° (20.42°)	108.52° (15.59°)	108.97° (11.93°)
Average coordination number	4.27	3.83	4.00	4.00

distribution. Since a typical value of the width of the Raman TO peak in *a*-Si ranges from 33 to 50 cm^{-1}, this approximately translates into a value of 9-13°for the average bond-angle deviation. This value is not far from with the RMS angular deviation (HWHM) of 15.6°from the FEAR model. It is noteworthy that the FEAR model is

statistically free of very small (≤ 60°) or large (≥ 160°) angles, and that the bond-angle distribution closely matches with the same from the WWW model. In contrast, a considerable number of small and large angles, below 60° and above 160°, respectively, have appeared in the bond-angle distribution of the CG-only model and in the RMC-only model[116]. Thus, the FEAR method not only produces correct two-body correlations between atoms, but also a better *reduced* three-body correlations by judicious use of the input experimental data and the local chemical information of *a*-Si provided from the *ab initio* total-energy functional from SIESTA within the CG loop of the refinement process. We have compared the ring statistics for the FEAR model to that of the WWW model in Fig. 5.3. Three-member rings are absent in both FEAR and WWW model which is consistent with the absence of unphysical Si triangles in good quality models. The only notable difference between the WWW and FEAR model is the existence of fewer 6-member rings in the FEAR model.

In Table 6.1, we have listed the characteristic structural properties of the models along with the total energy per atom obtained from the density-functional code Siesta. The FEAR model has 96% four-fold coordination, with equal (2% fractions) of 3-fold and 5-fold Si. This is equal to the melt-quench model using environment-dependent interaction potential (96%) [90] and better than models obtained from other techniques [47, 62, 91]. The average coordination number of our model is 4 which deviates from that of the experimental annealed sample (3.88) [32]. For comparison we have presented average coordination for various models in Table 6.1. It appears that the models having fewer coordination defects have higher average coordination then the experimentally reported value.

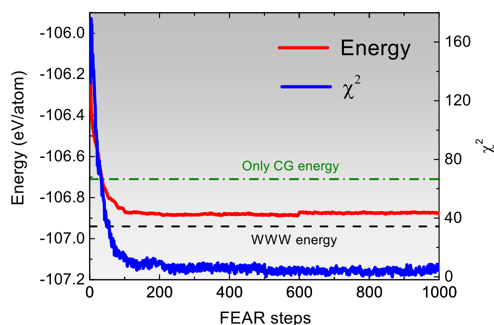

Figure 5.4: Total energy per atom and χ^2 versus FEAR steps for a 216-atom *a*-Si model. The green and black broken lines represent the energy per atom for the CG-only and WWW model, respectively.

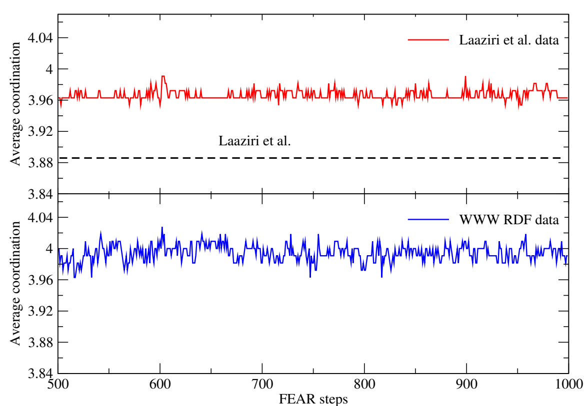

Figure 5.5: Variation of the average coordination number for the final 500 steps of FEAR using two different input RDF data. The upper panel is for high-energy X-ray diffraction data from Laaziri *et al.* [32] and the lower panel is for the WWW radial distribution function (RDF) as an input data [116]. The broken horizontal line, in the upper panel, represents the average coordination number, 3.88, reported by Laaziri *et. al.* [32]

5.3.2 Fluctuations in FEAR

The variation of the total energy (E) and χ^2 as FEAR proceeds is indicated in Fig.5.4. Figure 5.4 suggests that the initial structure formation takes place very rapidly in the first

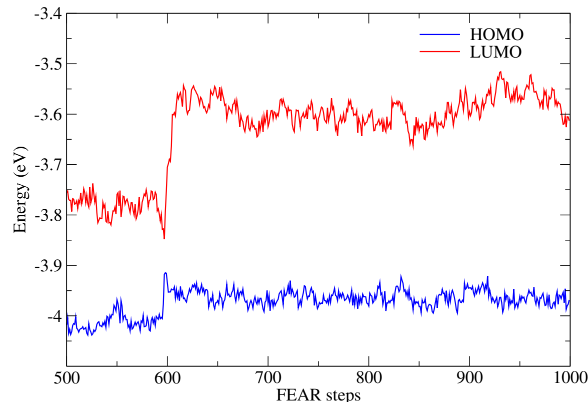

Figure 5.6: Variation of the highest occupied molecular orbital (HOMO)level and the lowest unoccupied molecular orbital (LUMO) level for the final 500 steps of FEAR. Note the annihilation of an electronic (gap state) defect near 600 steps.

few hundred steps with the simultaneous decrease of E and χ^2. We then reach a period of "saturation" in which there are tiny fluctuations in the energy and χ^2. We have reported a particular "snapshot" of a conformation, and discuss it above. However, the many conformations in the saturated part of the computation are equally meaningful. Fortunately they do not fluctuate much, reflecting the fact that the combination of experimental data and chemistry converge to a well-defined collection of configurations. We track the fluctuations in mean coordination in Fig. 5.5, excised from the last 500 steps of FEAR. For convenience we also show the results for a simulation with the WWW RDF, as we report in Ref. [116]. Using the RDF of WWW as input data forces the network to have fewer defects compared to the real experimental data. FEAR for the experimental sample fluctuates around 3.96, whereas the WWW fluctuates around 3.99.

In Fig. 5.6, we also track the fluctuations in the optical gap for the last 500 steps of FEAR, as crudely estimated as the energy splitting between the LUMO and HOMO levels. It is of considerable interest that for the last 500 FEAR steps, there is a substantial variation in the electronic density of states near the Fermi level even though the FEAR

process had already reached a "steady state" value for χ^2 and the total energy (compare Fig. 5.4). Observe too that while the HOMO level is fairly stationary, the LUMO meanders with relative impunity no doubt because it does not contribute to the total energy, being above the Fermi level. Thus, we see that FEAR effectively generates an ensemble of candidate structural models for a-Si which are essentially indistinguishable according to χ^2 and energy. Nevertheless, this affords another opportunity to use *a priori* information – we should select one of these models with the gap most like the experimental sample. To our knowledge, the electronic density of states is not well characterized for the sample, but if it was it would be natural to use it as an additional criterion to select the most experimentally realistic FEAR model. In effect if we had electronic information it would break the "structural degeneracy", emphasizing the information-based nature of our approach.

It is evident from Fig. 5.4 that the FEAR model has a lower energy than its CG-only counterpart. Table 6.1 lists the total-energy per atom w.r.t the energy of the WWW model, which is set at 0.0 eV for convenience. The energy for the FEAR model is found to be 0.06 eV/atom, which is approximately 50% lower than the CG-only model with a total-energy of 0.09 eV/atom. This is a reasonable number compared to other published work [121].

5.3.3 Electronic Structure

The electronic density of states (EDOS) of *a*-Si obtained from the FEAR, CG-only and RMC models are shown in Fig.5.7. For the 216-atom FEAR model, the quality of EDOS is significantly improved compared to that of CG relaxed model and the EDOS of the RMC model which is featureless. The significant number of defects states clutters the gap in FEAR, which is a prediction in this case, since the EDOS has not to our knowledge been measured for the sample we are studying. Electronic localization is studied using the

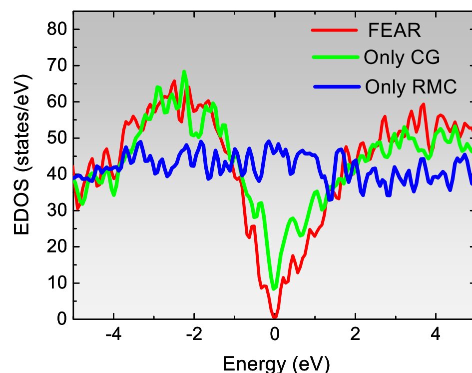

Figure 5.7: Electronic density of states (EDOS) of *a*-Si obtained from FEAR (red), CG-only (green) and pure RMC (blue) models. The Fermi levels are located at 0 eV.

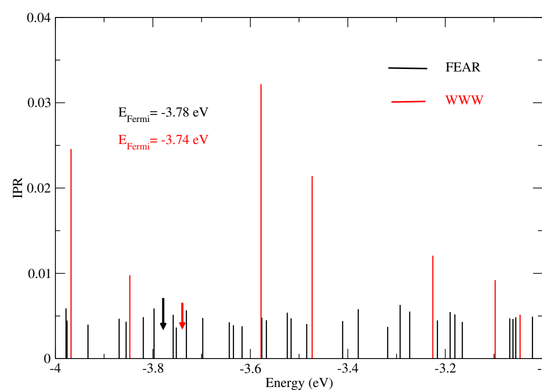

Figure 5.8: Inverse participation ratio (IPR) of 216-atom *a*-Si model for FEAR (black) and RMC (red) models near the gap. Fermi levels are shown by arrows of respective colors.

inverse participation ratio (IPR) [123] which is shown in Fig.5.8. Banding among the states in the gap leads to an expected delocalization[122].

5.3.4 Vibrational Properties

The vibrational density of states (VDOS) is computed by estimating the force constant matrix, from finite-difference calculations resulting from perturbing the atoms of

a well relaxed 216-atom FEAR model by 0.02 Å in six directions (± x-, ± y- and ± z-axis) and calculating the forces in all the remaining atoms for each perturbed configurations. The eigenvalues and eigenmodes are obtained by diagonalizing the dynamical matrix. The details can be found in a recent work of Bhattarai and Drabold [124]. The VDOS for 216-atom model FEAR model is shown in Fig.5.9. The calculated vdos is in rather good agreement with the experimental vdos obtained from inelastic neutron scattering [127]. The exception, probably a shortcoming of our Hamiltonian is a shift in the high frequency optical tail by ~35 cm^{-1}. This observation is consistent with the other empirical and *ab initio* molecular-dynamics simulations [125, 126].

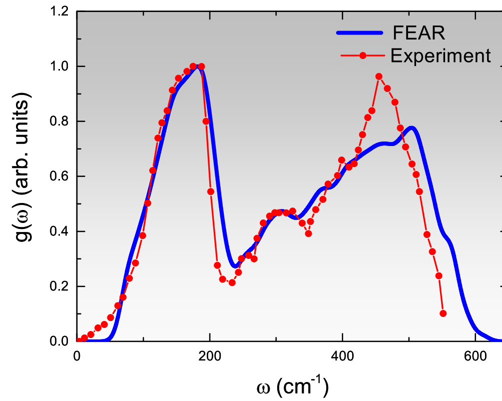

Figure 5.9: Vibrational density of states of *a*-Si, $g(\omega)$, from a 216-atom FEAR model (blue). The experimental vdos (red) obtained from Kamitakahara et al. [127]

The specific heat in the harmonic approximation is easily obtained from the density of states, $g(\omega)$. We note that wavelengths larger than our supercell size are not included in the obtained VDOS. We compute the specific heat $C_v(T)$ from the relation[128],[129],

$$C(T) = 3R \int_0^{E_{max}} \left(\frac{E}{k_B T}\right)^2 \frac{e^{E/k_B T}}{\left(e^{E k_B T} - 1\right)^2} g(E) dE \tag{5.1}$$

Here, the VDOS ($g(E)$) is normalized to unity.

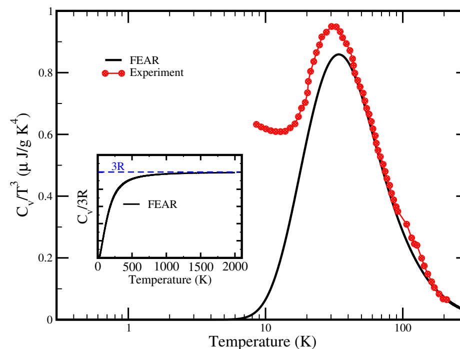

Figure 5.10: The specific heat capacity (C_V/T^3) for 216-atom *a*-Si FEAR model (black) compared to the experiment [130]. The inset shows the "Dulong-Petit" limit at higher temperature.

In Fig.5.10, we see that $C_V(T)$ for FEAR model is in a good agreement with experiment for $T > 40K$ [130]. The inset in Fig. 5.10 indicates the "3R" (Dulong-Petit) limit at high temperature. This is an additional indication that the FEAR model is reproducing features of a-Si beside those "built in" (from the experimental data), and is also an indication of consistency between these very different physical observables.

5.4 Conclusion

In this chapter, we have studied *a*-Si using a new approach FEAR. For the first time the experimental structure factor of *a*-Si [32] has been employed in FEAR along with *ab initio* interactions to generate a homogeneous model consistent with the data and at a plausible energy minimum according to reliable interatomic interactions. FEAR retains the simplicity and logic of RMC and successfully augments it with total-energy functional and forces to generate structures that are energetically stable, even exhibiting a satisfactory VDOS. The method can also be viewed as a new way to undertake first principles modeling of materials, when structural experiments are available.

By using an entirely information-based approach, educated by chemistry through the CG sub loops, we find highly plausible models derived from experimental data with

interesting similarities and differences with continuous random network models. Following this logic, the best that we can hope to achieve is a structural model jointly agreeing with all experiments, but critically, augmented with chemical information in an unbiased mode as we offer here.

6 Density Functional Model of Amorphous Zinc Oxide (a-ZnO) and Aluminium (Al), Gallium (Ga) and Indium (In) Doped a-ZnO

The work shown in this chapter has been accepted in the Journal of Non-Crystalline Solids and is published in an arxiv as: **Pandey, A., Scherich, H., and Drabold, D. A. (2016). Ab initio model of amorphous zinc oxide (a-ZnO) and a-$X_{0.375}Z_{0.625}O$ (X= Al, Ga and In).** *arXiv preprint arXiv:1610.00156.*.

6.1 Introduction

Crystalline ZnO has important application as a piezoelectric material and because of its property of being transparent in visible light [131]. It has a wide direct band gap (~ 3.37 eV at 300 K) which makes it a promising candidate for optoelectronic devices [131, 132]. Therefore, there has been a wealth of experimental work in crystalline ZnO. On the other hand, the study of amorphous ZnO is still in its nascent stage compared to its crystalline counterpart.

The amorphous transparent oxide materials have immense use in device technology [133]. Ionic amorphous oxide semiconductors like a-ZnO have high electron mobility (~ 5-40 cm^2/V s) compared to the covalent amorphous semiconductor like a-Si (~ 1 cm^2/V s) which make them a better candidate for device applications such as thin film transistors (TFTs) [134]. Experimentally, various techniques such as pulse laser deposition [135], molecular beam epitaxy [136], radio-frequency magnetron sputtering [137] etc. have been used to make a-ZnO and the structure obtained is highly dependent on the substrate material and temperature. There are advantages of a-ZnO over its crystalline counterpart. First, it is easier and more cost efficient to produce a large amorphous sheet compared to a large single crystal. Also, the a-ZnO has been prepared at low temperature

(~ 300 K) compared to crystalline ZnO (~ 800 K - 1100 K) [131]. On doping trivalent elements such as Al, Ga and In on a-ZnO mobility can be increased significantly [138].

In this chapter, we report the structure and electronic properties of amorphous phases of ZnO and a-ZnO doped with trivalent dopant atoms such as Indium (In), Gallium (Ga) and Aluminium (Al) using a plane wave basis density functional theory (DFT) code and comparisons with the experiments and other molecular dynamics (MD) simulations are made when possible. For the first time, accurate methods are used to compute the topological and chemical order of the materials and determine the electronic properties.

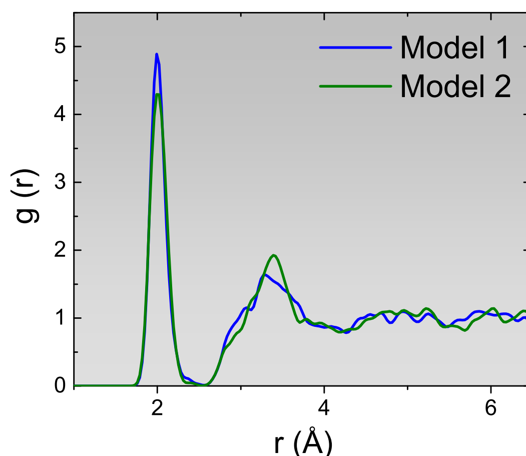

Figure 6.1: The total radial distribution function (RDF) for four a-ZnO models. Model 1 and Model 2 corresponds to the models obtained by two different quenching rates as described in the method section. Blue is for Model 1 and green is for Model 2.

6.2 Computational Methods

Density functional theory (DFT) calculations are performed using the plane-wave basis code VASP [100–102], using projected augmented plane waves (PAW) [19] with the Perdew-Burke-Ernzerhof (PBE) exchange-correlation functional [21] and a plane-wave

cutoff off energy of 300 eV. All calculations were carried out at Γ point. For a-ZnO, the system consists of 128 atoms in a cubic box of side 12.34 Å corresponding to the experimental density of 4.6 g/cm^3 [132]. A random initial configuration is equilibrated at 5000 K, is then cooled to 3000 K at 100 K/ps followed by an equilibration of 5 ps. The structure at 3000 K is cooled in steps to temperatures 2300 K, 1600 K and 300 K at the rate of 50 K/ps followed by 5 ps equilibration at each temperature. Finally, the structure at 300 K is quenched to 0 K at the rate of 25 K/ps which is again followed by equilibration of 5 ps. The structure is then relaxed using the conjugate gradient (CG) method. This model is termed Model 1. To contrast different quench rates, the configuration at 3000 K was also cooled to 300 K at a rate of 180 K/ps followed by the equilibration of 5 ps. Finally, the equilibrated structure is quenched to 0 K at a rate of 50 K/ps and then equilibrated for another 5 ps. The model is relaxed using CG method. We call this Model 2.

For a-$X_{0.375}Z_{0.625}O$ (X= Al, Ga and In), a random starting configuration of 128 atoms was melted at 5000 K followed by cooling to 3000 K at 100 K/ps and then equilibrated for 5 ps. A subsequent schedule of cooling is carried out at temperatures 2300 K, 1600 K and 300 K at a rate of 25 K/ps followed by the equilibration of 5 ps in each temperature. Finally, the structures are cooled to 0 K at the rate of 40 K/ps followed by an equilibration of 5 ps. The final structures are volume relaxed with the conjugate gradient method to tune the density. The cubical box lengths for Al-, Ga- and In-doped models after volume relaxations are 12.26 Å, 12.28 Å and 12.31 Å respectively, close to the assumed 12.34 Å.

6.3 Results and Discussion

In this section, we present the results for a-ZnO and Al-, Ga- and In-doped a-ZnO obtained from the *ab initio* molecular dynamics simulations using the 'melt-quench' technique. In particular, we investigate the structure and electronic properties by

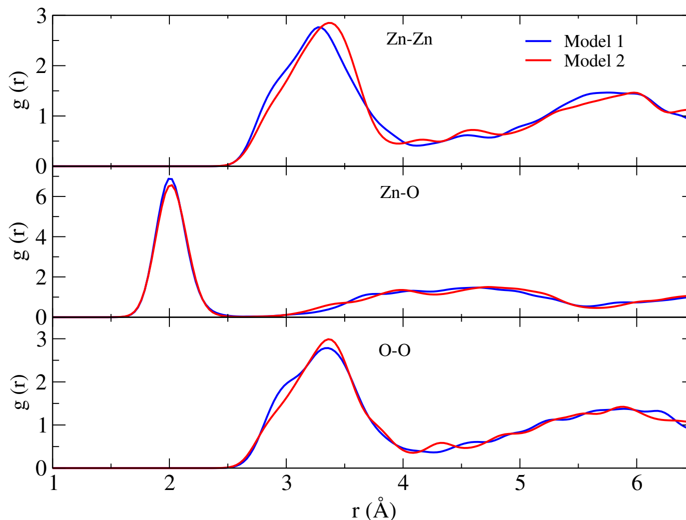

Figure 6.2: Partial pair correlation functions for 128-atom models of a-ZnO. Blue is for Model 1 and red is for Model 2 as described in the method section.

calculating the radial distribution functions (RDFs) and electronic density of states (EDOS).

6.3.1 Amorphous Zinc Oxide (a-ZnO)

Structural properties are investigated by the radial distribution functions (RDFs) and partial radial distribution functions. The total RDFs for Model 1 and Model 2 are shown in Fig.6.1. The partial pair correlation functions for Zn-Zn, Zn-O and O-O are shown in Fig.6.2. The partials for both models show similar features. For both Zn-Zn and O-O partials, the first peak is around 3.30 Å while for Zn-O the first peak position is at 2.00 Å as shown in Fig.6.2.

The network is chemically ordered. We calculated the coordination number for Zn and O. Most of the atoms are four-fold coordinated with above 75% four-fold coordinated Zn and O in both the models. Our models exhibit a higher fraction of four-fold Zn compared to the empirical molecular dynamics simulation model (~ 60%) [132]. The average coordination number for Zn (n_{Zn}) and O (n_O) and the 3-, 4- and 5-fold coordinated

Table 6.1: Coordination Number for Zn and O Expressed in Percentage, Average Coordination Number and the DFT-GGA Energy for a-ZnO Model. The Coordination Numbers for Zn are Compared With the Other MD Model [132]. As Expected There Are a Few More Coordination Defects in the More Rapidly Quenched Model 2.

	Model 1	Model 2	MD (Ref.([132])
Zn-Zn (%)	0	0	-
O-O (%)	0	0	-
Zn_3(%)	15.63	23.44	32.00
Zn_4(%)	81.25	75.00	60.00
Zn_5(%)	3.12	1.56	7.00
O_3(%)	15.63	25.00	-
O_4(%)	81.25	71.88	-
O_5(%)	3.12	3.12	-
n_{Zn}	3.88	3.78	-
n_O	3.88	3.78	-
Energy (eV/atom)	-4.36	-4.34	-

Zn and O, denoted by the respective subscript (Zn_3, O_3,...) is shown in Table 6.1. The DFT energy per atom for Model 1 is -4.36 eV/atom and for Model 2 is -4.34 eV/atom (Table 6.1). The energies of the two models are comparable.

The electronic structure is analysed by calculating the electronic density of states (EDOS) and inverse participation ratio (IPR) of the individual states. The EDOS is just taken to be the density of Kohn-Sham eigenvalues and the IPR is computed from the atom-projected Kohn-Sham eigenvectors. The EDOS is shown in Fig.6.3 (black) and the

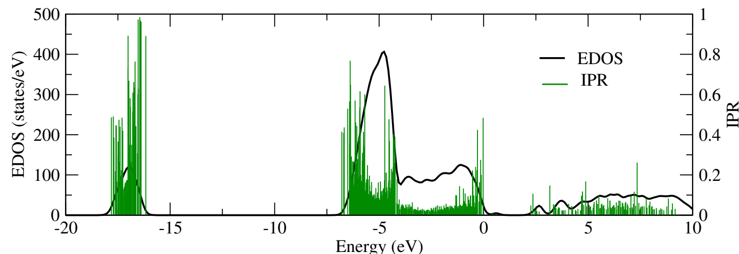

Figure 6.3: (black) Electronic density of states of the 128-atom model a-ZnO (Model I) obtained using GGA-PBE density functional theory calculation. The green vertical lines represent the inverse participation ratio (IPR) used to measure the electronic state localization. Longer IPR implies strong localization. The Fermi level is at 0.28 eV. The PBE gap is 1.36 eV.

green vertical lines represents the electronic state localization measured by IPR [140**?**]. The value of IPR is 1 for a highly localized state and 1/N for an extended state, where N is the number of atoms. IPR in Fig.6.3 shows that the localization of valence tail states is much larger than the conduction tail states. Thus, the mobility of *n*-type of carrier is expected to be much higher than the *p*-type. This feature supports the asymmetry in the localization of valence and conduction band tail states in amorphous metal oxide by Robertson [134]. Similar asymmetrical behavior in amorphous gallium nitride was shown by Cai and Drabold [141].

The band gap (gap between the highest occupied electronic state and the lowest unoccupied electronic state), is 1.36 eV which is slightly less than the experimental band gap of 1.60 eV between the valence band edge and Zn4s4p states [144]. The band gap is always underestimated in a DFT-GGA calculation which could be improved by using hybrid functional [142], GW approximation [143], etc.

6.3.2 Al-, Ga- and In-doped Amorphous ZnO: a-$X_{0.375}Z_{0.625}O$ (X= Al, Ga and In)

To investigate the effect of trivalent dopants on local coordination and electronic structure of a-ZnO, 37.5% of Zn is replaced by group III elements X (X= Al, Ga and In)

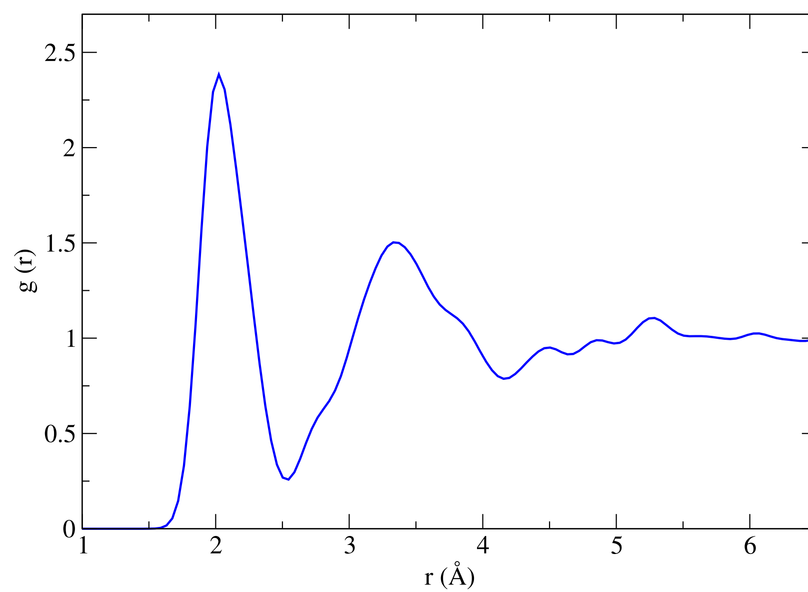

a)

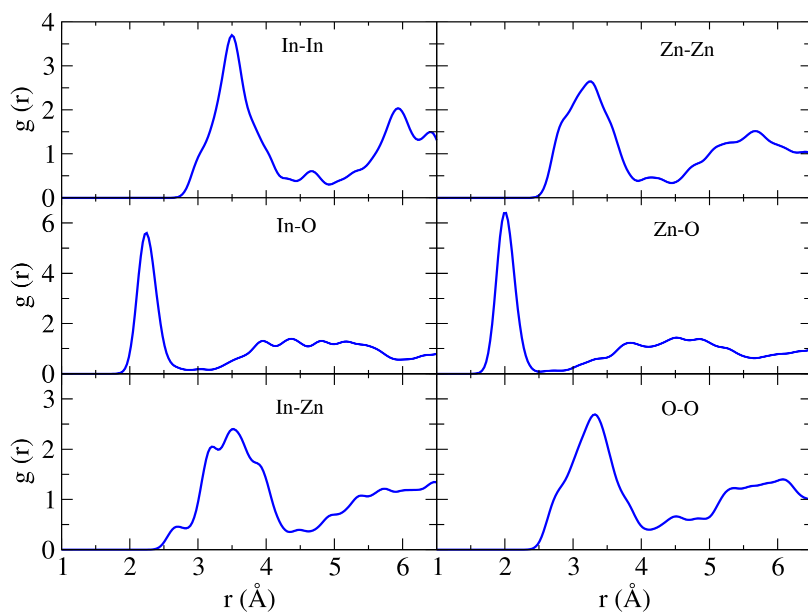

b)

Figure 6.4: (a) Total pair correlation functions for 128-atom $In_{0.375}Z_{0.625}O$ model. (b) Partial pair correlation function of $In_{0.375}Z_{0.625}O$ model.

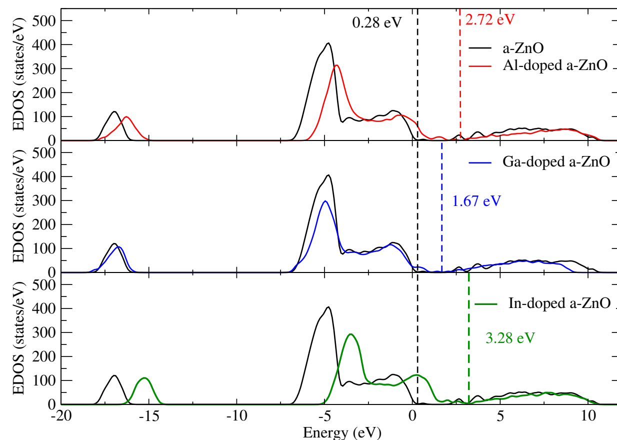

Figure 6.5: Electronic density of states for a-$X_{0.375}Z_{0.625}O$ (X= Al, Ga and In) models compared to that of a-ZnO. The Fermi levels are shown by vertical broken lines.

to model a-$X_{0.375}Z_{0.625}O$. The atomic percentage of dopants in all the models is 18.75%. The effect of dopants on structure and electronic properties are investigated by RDFs, partial pair correlation functions and electronic density of states.

Table 6.2: First Peak Position for Zn-Zn, Zn-O and O-O Partial Pair Correlation Functions of a-ZnO (Model 1) and a-$X_{0.375}Z_{0.625}O$ (X= Al, Ga and In) Models.

Peak position (Å)				
First peak	ZnO (Model1)	$Al_{0.375}Z_{0.625}O$	$Ga_{0.375}Z_{0.625}O$	$In_{0.375}Z_{0.625}O$
Zn-Zn	3.28	2.60	2.87	3.26
Zn-O	2.00	2.00	2.00	2.00
O-O	3.36	2.93	3.10	3.33

The total RDFs for In-doped a-ZnO is shown in Fig.6.4a. The Zn-O correlation is not affected by the presence of dopants while there is a slight decrease in the correlation peaks for Zn-Zn and O-O which is illustrated in Table 6.2. The peak positions are obtained from

the partial pair correlation functions shown in Fig.6.4b for In-doped a-ZnO and similar plots for Al-, and Ga-doped a-ZnO which is not shown here. The 4-fold Zn and O are reduced significantly in all three doped models. The Al and In bond only with O. In the Al-doped model, 95.83% and 4.17% Al forms 4-fold and 3-fold bond with O. In the In-doped model, 20.83%, 25.00%, 8.33%, 37.5% and 8.34% In form 6-, 5-, 4-, 3- and 2-fold bond with O atom. In the Ga-doped model, 58.33% and 33.33% Ga form 4-fold and 3-fold bond with O while 8.34% Ga form 3-fold with O and 1-fold with Zn. This suggest that the group III elements are more likely to form a bond with O while introduced to a a-ZnO.

The Zn-Zn and In-In distances in our model are around 3.26 Å and 3.50 Å which is close to 3.20-3.40 Å for Zn-Zn and 3.30-3.6 Å for In-In of classical MD model [145]. This compares well with the average metal-metal peak in x-ray diffraction measurements of IZO thin layers [146]. Also, the Zn-O and In-O distances in our model are around 2.00 Å and 2.20 Å compared to the 1.95 Å— and 2.20 Å respectively of the classical MD model [145]. These peak positions are consistent with the metal-oxygen peaks at 2.12-2-14 Å in the experiment [146].

The electronic density of states (EDOS) for a-$X_{0.375}Z_{0.625}O$ (X= Al, Ga and In) models is shown in Fig.6.5. Dopants lead to the creation of defect states. The localized states near the valence band edge induced by doping can be associated to the increase in undercoordinated O atoms in the network introduced by doping. The conduction band edge is unaltered by the addition of dopant elements. The extended nature of the conduction band is preserved by the addition of dopants which is in accordance with the conclusion by Hosono [138]. On the other hand, in crystalline ZnO doped by group III elements Al, Ga and In, the dopants form extra localized level in the conduction band, which modifies the conduction band and reduces the optical band gap [139].

6.4 Conclusion

In conclusion, we have created models of amorphous zinc oxide (a-ZnO) using a melt-quench method and studied their structural and electronic properties in detail. The electronic band gap of our model is 1.36 eV which is in reasonable agreement with the experimental band gap 1.60 eV. We have calculated the DFT energies for the two models of a-ZnO obtained by different quenching rate for comparison. The effect of trivalent dopants in the local structure and the electronic structure of a-ZnO is investigated in detail by preparing a-$X_{0.375}Z_{0.625}O$ (X= Al, Ga and In) models by melt-quench method. The dopants reduce the number of 4-fold coordinated Zn and O in the network and most of them prefer to bond with oxygen. The electronic gap is reduced by the presence of defect states by forming undercoordinated O states in the valence band edge while the conduction band edge is still extended.

7 Conclusion and Future Work

We have introduced a new and practical method, Force-Enhanced Atomic Refinement (FEAR), that jointly exploits the features inherent to the *ab initio* total-energy calculations and experimental information. The method is simple, robust, faster and independent of the systems. As a preliminary trial, using empirical interactions, FEAR successfully generated *a*-Si and *a*-SiO_2 models that are comparable to the ones obtained from other successful approaches. We have implemented the method with *ab initio* interactions to model two highly distinct systems: *a*-Si and two different compositions of Ag-doped $GeSe_3$. The former is an archetypal non-glass forming amorphous material while the latter ones are the chalcogenide glasses that are used for computer memory materials. The *a*-Si model is structurally comparable to the WWW models, both in terms of coordination number and bond angle. The $GeSe_3Ag$ models are better than the ones obtained from the traditional methods, such as melt-quench and RMC. An additional application of FEAR, the *a*-Si model obtained using experimental X-ray diffraction data is on a par with the existing models and represent a structure for a real sample. It was also discovered that the method requires a fewer number of force calls to the expensive *ab initio* interactions than the conventional melt-quench approach.

An *ab initio* molecular dynamics simulations (AIMD) was used to study the doping in *a*-Si:H. It was found that the non-tetrahedral impurities (B and P) create strain in the local bonding, which attracts H atoms and induce H passivation. Also, the fluctuations in HOMO-LUMO levels, induced by H hopping and network motion, affect the conductivity of this material. Likewise, a-ZnO and a-$X_{0.375}Z_{0.625}O$ (X= Al, Ga, and In) models were prepared by the melt-quench method using AIMD and their structures and electronic structures were investigated in detail. The electronic band gap of the a-ZnO model is 1.36 eV which is in a reasonable agreement with the experimental band gap 1.60 eV. The trivalent dopants (Al, Ga, and In) prefer to bond with O and reduce the number of 4-fold

coordinated Zn and O in the network. The electronic gap is reduced by the valence tail states introduced by undercoordinated O atoms.

7.1 Future Work

FEAR would be an alternative method to model those amorphous materials that are challenging using the conventional approaches of MD simulations and data inversion (e.g. amorphous phosphorous, selenium rich chalcogenide ($GeSe_9$), etc.). In the current work, only a single data set, either the structure factor or the pair correlation function, is used in FEAR. The method can be developed into a scheme to include multiple datasets or other information for materials optimization. The simplest thing would be to use the partial pair correlation functions in the modeling of multi-component complex materials. Incorporating NMR results and EXAFS data would be an another thing to try in FEAR. Due to the phase separation in silver-doped germanium selenide, larger theoretical models that could capture the phase separations are essential in the study of such materials. FEAR with an empirical potential would be an appropriate method to try modeling larger samples (containing thousands of atoms) of silver-doped chalcogenide materials.

References

[1] Bragg, W. H., and Bragg, W. L. (1913). The reflection of X-rays by crystals. *Proceedings of the Royal Society of London. Series A, Containing Papers of a Mathematical and Physical Character, 8*8(605), 428-438.

[2] Kendrew, J. C., Bodo, G., Dintzis, H. M., Parrish, R. G., Wyckoff, H., and Phillips, D. C. (1958). A three-dimensional model of the myoglobin molecule obtained by x-ray analysis. *Nature, 181*(4610), 662-666.

[3] Zachariasen, W. H. (1932). The atomic arrangement in glass. *Journal of the American Chemical Society, 54*(10), 3841-3851.

[4] Bell, R. J., and Dean, P. (1966). Properties of vitreous silica: analysis of random network models. *Nature, 212*,1354.

[5] Polk, D. E. (1971). Structural model for amorphous silicon and germanium. *Journal of Non-Crystalline Solids, 5*(5), 365-376.

[6] Guttman, L., Ching, W. Y., and Rath, J. (1980). Charge-density variation in a model of amorphous silicon. *Physical Review Letters, 44*(23), 1513.

[7] Wooten, F., Winer, K., and Weaire, D. (1985). Computer generation of structural models of amorphous Si and Ge. *Physical review letters, 54*(13), 1392.

[8] Mousseau, N., and Barkema, G. T. (2004). Binary continuous random networks. *Journal of Physics: Condensed Matter, 16*(44), S5183.

[9] Barkema, G. T., and Mousseau, N. (2000). High-quality continuous random networks. *Physical Review B, 62*(8), 4985.

[10] Stillinger, F. H., and Weber, T. A. (1985). Computer simulation of local order in condensed phases of silicon. *Physical review B, 31*(8), 5262.

[11] Car, R., and Parrinello, M. (1988). Structural, dymanical, and electronic properties of amorphous silicon: an ab initio molecular-dynamics study. *Physical review letters, 60*(3), 204.

[12] McGreevy, R. L., and Pusztai, L. (1988). Reverse Monte Carlo simulation: a new technique for the determination of disordered structures. *Molecular Simulation, 1*(6), 359-367.

[13] Hohenberg, P., and Kohn, W. (1964). Inhomogeneous electron gas. *Physical review, 136*(3B), B864.

[14] Kohn, W., and Sham, L. J. (1965). Self-consistent equations including exchange and correlation effects. *Physical review, 140*(4A), A1133.

[15] Martin, R. M. (2004). *Electronic structure: basic theory and practical methods*. Cambridge university press.

[16] Soler, J. M., Artacho, E., Gale, J. D., Garca, A., Junquera, J., Ordejn, P., and Snchez-Portal, D. (2002). The SIESTA method for ab initio order-N materials simulation. *Journal of Physics: Condensed Matter, 14*(11), 2745.

[17] Kresse, G., and Furthmller, J. (1996). Efficient iterative schemes for ab initio total-energy calculations using a plane-wave basis set. *Physical review B, 54*(16), 11169.

[18] Laasonen, K., Car, R., Lee, C., and Vanderbilt, D. (1991). Implementation of ultrasoft pseudopotentials in ab initio molecular dynamics. *Physical Review B, 43*(8), 6796.

[19] Kresse, G., and Joubert, D. (1999). From ultrasoft pseudopotentials to the projector augmented-wave method. *Physical Review B, 59*(3), 1758.

[20] Hafner, J. (2008). Abinitio simulations of materials using VASP: Densityfunctional theory and beyond. *Journal of computational chemistry, 29*(13), 2044-2078.

[21] Perdew, J. P., Burke, K., and Ernzerhof, M. (1996). Generalized gradient approximation made simple. *Physical review letters, 77*(18), 3865.

[22] Marsman, M., Paier, J., Stroppa, A., and Kresse, G. (2008). Hybrid functionals applied to extended systems. *Journal of Physics: Condensed Matter, 20*(6), 064201.

[23] Drabold, D. A. (2009). Topics in the theory of amorphous materials. *The European Physical Journal B, 68*(1), 1-21.

[24] Opletal, G., Petersen, T. C., McCulloch, D. G., Snook, I. K., and Yarovsky, I. (2005). The structure of disordered carbon solids studied using a hybrid reverse Monte Carlo algorithm. *Journal of Physics: Condensed Matter, 17*(17), 2605.

[25] Biswas, P., Atta-Fynn, R., and Drabold, D. (2004). The inclusion of experimental information in first principles modelling of materials. *Journal of Physics: Condensed Matter, 16*(44), S5173.

[26] Le Roux, S., and Petkov, V. (2010). ISAACSinteractive structure analysis of amorphous and crystalline systems. *Journal of Applied Crystallography, 43*(1), 181-185.

[27] Tucker, M. G., Keen, D. A., Dove, M. T., Goodwin, A. L., and Hui, Q. (2007). RMCProfile: reverse Monte Carlo for polycrystalline materials. *Journal of Physics: Condensed Matter, 19*(33), 335218.

[28] Street, R. A. (2005). *Hydrogenated amorphous silicon*. Cambridge University Press.

[29] Santos, I., Marqus, L. A., Pelaz, L., and Colombo, L. (2011). Elucidating the atomistic mechanisms driving self-diffusion of amorphous Si during annealing. *Physical Review B, 83*(15), 153201.

[30] Pan, Y., Inam, F., Zhang, M., and Drabold, D. A. (2008). Atomistic origin of Urbach tails in amorphous silicon. *Physical review letters, 100*(20), 206403.

[31] Barkema, G. T., and Mousseau, N. (1996). Event-based relaxation of continuous disordered systems. *Physical review letters, 77*(21), 4358.

[32] Laaziri, K., Kycia, S., Roorda, S., Chicoine, M., Robertson, J. L., Wang, J., and Moss, S. C. (1999). High resolution radial distribution function of pure amorphous silicon. *Physical review letters, 82*(17), 3460.

[33] Pandey, A., Cai, B., Podraza, N., and Drabold, D. A. (2014). Electrical Activity of Boron and Phosphorus in Hydrogenated Amorphous Silicon. *Physical Review Applied, 2*(5), 054005.

[34] Dagenais, P., Lewis, L. J., and Roorda, S. (2015). Understanding subtle changes in medium-range order in amorphous silicon. *Journal of Physics: Condensed Matter, 27*(29), 295801.

[35] Beeman, D., Tsu, R., and Thorpe, M. F. (1985). Structural information from the Raman spectrum of amorphous silicon. *Physical Review B, 32*(2), 874.

[36] Fieque, B., Tissot, J. L., Trouilleau, C., Crastes, A., and Legras, O. (2007). Uncooled microbolometer detector: Recent developments at Ulis. *Infrared Physics and Technology, 49*(3), 187-191.

[37] Spear, W. E., and Le Comber, P. G. (1975). Substitutional doping of amorphous silicon. *Solid state communications, 17*(9), 1193-1196.

[38] Ziman, J. M. (1979). *Models of disorder: the theoretical physics of homogeneously disordered systems*. CUP Archive.

[39] Drabold, D. A., Abtew, T. A., Inam, F., and Pan, Y. (2008). Network structure and dynamics of hydrogenated amorphous silicon. *Journal of Non-Crystalline Solids, 354*(19), 2149-2154.

[40] Fedders, P. A., and Drabold, D. A. (1996). Molecular-dynamics investigations of conformational fluctuations and low-energy vibrational excitations in a-Si: H. *Physical Review B, 53*(7), 3841.

[41] Atta-Fynn, R., Biswas, P., and Drabold, D. A. (2004). Electronphonon coupling is large for localized states. *Physical Review B, 69*(24), 245204.

[42] Abtew, T. A., Inam, F., and Drabold, D. A. (2007). Thermally stimulated H emission and diffusion in hydrogenated amorphous silicon. *EPL (Europhysics Letters), 79*(3), 36001.

[43] Boyce, J. B., and Ready, S. E. (1988). Nuclear-magnetic-double-resonance investigation of the dopant microstructure in hydrogenated amorphous silicon. *Physical Review B, 38*(16), 11008.

[44] Fedders, P. A., and Drabold, D. A. (1997). Theory of boron doping in a-Si: H. *Physical Review B, 56*(4), 1864.

[45] Cai, B., and Drabold, D. A. (2011). Theoretical studies of structure and doping of hydrogenated amorphous silicon. In *MRS Proceedings* (Vol. 1321, pp. mrss11-1321). Cambridge University Press.

[46] Liang, J., Schiff, E. A., Guha, S., Yan, B., and Yang, J. (2006). Hole mobility limit of amorphous silicon solar cells.

[47] Cliffe, M. J., Dove, M. T., Drabold, D. A., and Goodwin, A. L. (2010). Structure determination of disordered materials from diffraction data. *Physical review letters, 104*(12), 125501.

[48] Drabold, D. A., Li, Y., Cai, B., and Zhang, M. (2011). Urbach tails of amorphous silicon. *Physical Review B, 83*(4), 045201.

[49] Pan, Y., Inam, F., Zhang, M., and Drabold, D. A. (2008). Atomistic origin of Urbach tails in amorphous silicon. Physical review letters, 100(20), 206403.; Pan, Y., Zhang, M., and Drabold, D. A. (2008). Topological and topological-electronic correlations in amorphous silicon. *Journal of Non-Crystalline Solids, 354*(29), 3480-3485.

[50] Heyd, J., Scuseria, G. E., and Ernzerhof, M. (2003). Hybrid functionals based on a screened Coulomb potential. *The Journal of Chemical Physics, 118*(18), 8207-8215.

[51] Barkema, G. T., and Mousseau, N. (2000). High-quality continuous random networks. *Physical Review B, 62*(8), 4985.

[52] Santos, I., Castrillo, P., Windl, W., Drabold, D. A., Pelaz, L., and Marqus, L. A. (2010). Self-trapping in B-doped amorphous Si: Intrinsic origin of low acceptor efficiency. *Physical Review B, 81*(3), 033203.

[53] Mott, N. F., and Davis, E. A. (2012). *Electronic processes in non-crystalline materials*. OUP Oxford.

[54] Anderson, P. W. (1958). Absence of diffusion in certain random lattices. *Physical review, 109*(5), 1492.

[55] Dong, J., and Drabold, D. A. (1996). Band-tail states and the localized-to-extended transition in amorphous diamond. *Physical Review B, 54*(15), 10284.

[56] Parman, C. E., Israeloff, N. E., and Kakalios, J. (1992). Conductance-noise power fluctuations in hydrogenated amorphous silicon. *Physical review letters, 69*(7), 1097.

[57] Kubo, R. (1957). Statistical-mechanical theory of irreversible processes. I. General theory and simple applications to magnetic and conduction problems. *Journal of the Physical Society of Japan, 12*(6), 570-586.

[58] Greenwood, D. A. (1958). The Boltzmann equation in the theory of electrical conduction in metals. *Proceedings of the Physical Society, 71*(4), 585.

[59] Abtew, T. A., Zhang, M., and Drabold, D. A. (2007). Ab initio estimate of temperature dependence of electrical conductivity in a model amorphous material: Hydrogenated amorphous silicon. *Physical Review B, 76*(4), 045212.

[60] Lide, D. R. (Ed.). (2004). *CRC handbook of chemistry and physics* (Vol. 85). CRC press.

[61] Gereben, O., and Pusztai, L. (1994). Structure of amorphous semiconductors: Reverse Monte Carlo studies on a-C, a-Si, and a-Ge. *Physical Review B, 50*(19), 14136.

[62] Biswas, P., Atta-Fynn, R., and Drabold, D. A. (2004). Reverse Monte Carlo modeling of amorphous silicon. *Physical Review B, 69*(19), 195207.

[63] Keen, D. A., and Dove, M. T. (1999). Local structures of amorphous and crystalline phases of silica, SiO2, by neutron total scattering. *Journal of Physics: Condensed Matter, 11*(47), 9263.

[64] Kohara, S., and Suzuya, K. (2005). Intermediate-range order in vitreous SiO2 and GeO2. *Journal of Physics: Condensed Matter, 17*(5), S77.

[65] McGreevy, R. L. (2001). Reverse monte carlo modelling. *Journal of Physics: Condensed Matter, 13*(46), R877.

[66] Gereben, O., and Pusztai, L. (2012). RMC_POT: a computer code for reverse Monte Carlo modeling the structure of disordered systems containing molecules of arbitrary complexity. *Journal of computational chemistry, 33*(29), 2285-2291.

[67] Soper, A. K. (2001). Tests of the empirical potential structure refinement method and a new method of application to neutron diffraction data on water. *Molecular Physics, 99*(17), 1503-1516.

[68] Prasai, K., Biswas, P., and Drabold, D. A. (2015). Sculpting the band gap: a computational approach. *Scientific reports, 5*.

[69] Biswas, P., Tafen, D. N., Inam, F., Cai, B., and Drabold, D. A. (2009). Materials modeling by design: applications to amorphous solids. *Journal of Physics: Condensed Matter, 21*(8), 084207.

[70] J. Nocedal and S.J. Wright, *Numerical Optimization*, Springer Series in Operations Research, Springer 2006.

[71] Earl, D. J., and Deem, M. W. (2005). Parallel tempering: Theory, applications, and new perspectives. *Physical Chemistry Chemical Physics, 7*(23), 3910-3916.

[72] A. E. Eiben and J. E. Smith, *Introduction to Evolutionary Computing*, Natural Computing Series, Springer 2008.

[73] Justo, J. F., Bazant, M. Z., Kaxiras, E., Bulatov, V. V., and Yip, S. (1998). Interatomic potential for silicon defects and disordered phases. *Physical review B, 58*(5), 2539.

[74] Van Beest, B. W. H., Kramer, G. J., and Van Santen, R. A. (1990). Force fields for silicas and aluminophosphates based on ab initio calculations. *Physical Review Letters, 64*(16), 1955.

[75] Carre, A., Horbach, J., Ispas, S., and Kob, W. (2008). New fitting scheme to obtain effective potential from Car-Parrinello molecular-dynamics simulations: Application to silica. *EPL (Europhysics Letters), 82*(1), 17001.

[76] Essmann, U., Perera, L., Berkowitz, M. L., Darden, T., Lee, H., and Pedersen, L. G. (1995). A smooth particle mesh Ewald method. *The Journal of chemical physics, 103*(19), 8577-8593.

[77] Wolf, D., Keblinski, P., Phillpot, S. R., and Eggebrecht, J. (1999). Exact method for the simulation of Coulombic systems by spherically truncated, pairwise r-1 summation. *The Journal of chemical physics, 110*(17), 8254-8282.

[78] Fennell, C. J., and Gezelter, J. D. (2006). Is the Ewald summation still necessary? Pairwise alternatives to the accepted standard for long-range electrostatics. *The Journal of chemical physics, 124*(23), 234104.

[79] Tafen, D. N., and Drabold, D. A. (2005). Models and modeling schemes for binary IV-VI glasses. *Physical Review B, 71*(5), 054206.

[80] Vashishta, P., Kalia, R. K., Rino, J. P., and Ebbsj, I. (1990). Interaction potential for SiO_2: a molecular-dynamics study of structural correlations. *Physical Review B, 41*(17), 12197.

[81] Sarnthein, J., Pasquarello, A., and Car, R. (1995). Structural and Electronic Properties of Liquid and Amorphous SiO_2: An Ab Initio Molecular Dynamics Study. *Physical review letters, 74*(23), 4682.

[82] For *empirical* potentials with a finite cutoff R_c, the number of force evaluation is proportional to pN, where p is the average number of atoms within the interacting sphere of radius R_c and N is the total number of atoms in the system. The list of p atoms can be constructed periodically in an $O(N)$ manner by partitioning the entire volume into several cells, and generating a list of atoms in each cell. The $O(N)$ calculation of pair-correlation data can be achieved in a straightforward way.

[83] Mei, Q., Benmore, C. J., Sen, S., Sharma, R., and Yarger, J. L. (2008). Intermediate range order in vitreous silica from a partial structure factor analysis. *Physical Review B, 78*(14), 144204.

[84] Nakano, A., Kalia, R. K., and Vashishta, P. (1994). First sharp diffraction peak and intermediate-range order in amorphous silica: finite-size effects in molecular dynamics simulations. *Journal of non-crystalline solids, 171*(2), 157-163.

[85] Tafen, D. N. and Drabold, D. A. (2003). Realistic models of binary glasses from models of tetrahedral amorphous semiconductors. *Physical Review B, 68*(16), 165208.

[86] Mozzi, R. L., and Warren, B. E. (1969). The structure of vitreous silica. *Journal of Applied Crystallography, 2*(4), 164-172.

[87] Massobrio, C., Du, J., Bernasconi, M., and Salmon, P. S. (2015). *Molecular Dynamics Simulations of Disordered Materials*. Springer.

[88] Fischer, B., Pollak, R. A., DiStefano, T. H., and Grobman, W. D. (1977). Electronic structure of SiO_2, $Si_xGe_{1-x}O_2$, and GeO_2 from photoemission spectroscopy. *Physical Review B, 15*(6), 3193.

[89] Benoit, M., Ispas, S., Jund, P., and Jullien, R. (2000). Model of silica glass from combined classical and ab initio molecular-dynamics simulations. *The European Physical Journal B-Condensed Matter and Complex Systems, 13*(4), 631-636.

[90] Keblinski, P., Bazant, M. Z., Dash, R. K., and Treacy, M. M. (2002). Thermodynamic behavior of a model covalent material described by the environment-dependent interatomic potential. *Physical Review B, 66*(6), 064104.

[91] Ishimaru, M., Munetoh, S., and Motooka, T. (1997). Generation of amorphous silicon structures by rapid quenching: A molecular-dynamics study.*Physical Review B, 56*(23), 15133.

[92] Eberhart, M. E., and Clougherty, D. P. (2004). Looking for design in materials design. *Nature materials, 3*(10), 659-661.

[93] Carter, E. A. (2008). Challenges in modeling materials properties without experimental input. *Science, 321*(5890), 800-803.

[94] Pandey, A., Biswas, P., and Drabold, D. A. (2015). Force-enhanced atomic refinement: Structural modeling with interatomic forces in a reverse Monte Carlo approach applied to amorphous Si and SiO 2. *Physical Review B, 92*(15), 155205.

[95] Timilsina, R., and Biswas, P. (2013). A study of hydrogen microstructure in amorphous silicon via inversion of nuclear magnetic resonance spectra. *Journal of Physics: Condensed Matter, 25*(16), 165801.

[96] Meredig, B., and Wolverton, C. (2013). A hybrid computationalexperimental approach for automated crystal structure solution. *Nature materials, 12*(2), 123-127.

[97] Pickard, C. J., and Needs, R. J. (2011). Ab initio random structure searching. *Journal of Physics: Condensed Matter, 23*(5), 053201.

[98] Rieping, W., Habeck, M., and Nilges, M. (2005). Inferential structure determination. *Science, 309*(5732), 303-306.

[99] McGuire, G. E. (1988). *Semiconductor materials and process technology handbook*. William Andrew.

[100] Kresse, G., and Hafner, J. (1993). Ab initio molecular dynamics for liquid metals. *Physical Review B, 47*(1), 558.

[101] Kresse, G., and Furthmller, J. (1996). Efficient iterative schemes for ab initio total-energy calculations using a plane-wave basis set. *Physical review B, 54*(16), 11169.

[102] Kresse, G., and Furthmller, J. (1996). Efficiency of ab-initio total energy calculations for metals and semiconductors using a plane-wave basis set. *Computational Materials Science, 6*(1), 15-50.

[103] Piarristeguy, A. A., Cuello, G. J., FernandezMartinez, A., Cristiglio, V., Johnson, M., Ribes, M., and Pradel, A. (2012). Short range order and Ag diffusion threshold in $Ag_x(Ge_{0.25}Se_{0.75})_{100-x}$ glasses. *physica status solidi (b), 249*(10), 2028-2033.

[104] Zeidler, A., Salmon, P. S., Piarristeguy, A., Pradel, A., and Fischer, H. E. (2016). Structure of Glassy Ag-Ge-Se by Neutron Diffraction with Isotope Substitution. *Zeitschrift fur Physikalische Chemie, 230*(3), 417-432.

[105] Phillips, J. C., Bean, J. C., Wilson, B. A., and Ourmazd, A. (1987). Bragg diffraction by amorphous silicon. *Nature, 325*, 121-125.

[106] Mousseau, N., and Barkema, G. T. (1998). Traveling through potential energy landscapes of disordered materials: The activation-relaxation technique. *Physical Review E, 57*(2), 2419.

[107] Tafen, D. N., Drabold, D. A., and Mitkova, M. (2005). Silver transport in Ge_xSe_{1-x}: Ag materials: Ab initio simulation of a solid electrolyte. *Physical Review B, 72*(5), 054206.

[108] Kozicki, M. N., and West, W. C. Programmable metallization cell structure and method of making same, *US Patent 5,761*,115 (1998).

[109] Waser, R., and Aono, M. (2007). Nanoionics-based resistive switching memories. *Nature materials, 6*(11), 833-840.

[110] Kawasaki, M., Kawamura, J., Nakamura, Y., and Aniya, M. (1999). Ionic conductivity of $Ag_x(GeSe_3)_{1-x}(0 \leq x \leq 0.571)$ glasses. *Solid State Ionics, 123*(1), 259-269.

[111] Urena, M. A., Piarristeguy, A. A., Fontana, M., and Arcondo, B. (2005). Ionic conductivity (Ag+) in AgGeSe glasses.*Solid state ionics, 176*(5), 505-512.

[112] Nosengo, N (2016). The Material Code: Machine-learning techniques could revolutionize how materials science is done. *Nature, 533*, 22.

[113] Ramakrishnan, V. (2010). Unraveling the structure of the ribosome (Nobel Lecture). *Angewandte Chemie International Edition, 49*(26), 4355-4380.

[114] Jaynes, E. T. (1957). Information theory and statistical mechanics. *Physical review, 106*(4), 620.

[115] Proffen, T., and Billinge, S. J. L. (1999). PDFFIT, a program for full profile structural refinement of the atomic pair distribution function. *Journal of Applied Crystallography, 32*(3), 572-575.

[116] Pandey, A., Biswas, P., and Drabold, D. A. (2016). Inversion of diffraction data for amorphous materials. *Scientific Reports, 6*, 33731.

[117] Cliffe, M. J., Bartok, A. P., Kerber, R. N., Grey, C. P., Csanyi, G., and Goodwin, A. L. (2016). Structural Simplicity as a Constraint on the Structure of Amorphous Silicon. *arXiv preprint arXiv:1609.00668*.

[118] Prasai, K., Biswas, P., and Drabold, D. A. (2016). Electronically designed amorphous carbon and silicon. *physica status solidi (a)*.

[119] A. Pandey and D. A. Drabold (unpublished).

[120] Treacy, M. M. J., and Borisenko, K. B. (2012). The local structure of amorphous silicon. *Science, 335*(6071), 950-953.

[121] Drabold, D. A. (2011). Silicon: the gulf between crystalline and amorphous. *physica status solidi (RRL)-Rapid Research Letters, 5*(1011), 359-360.

[122] Dong, J., and Drabold, D. A. (1998). Atomistic structure of band-tail states in amorphous silicon. *Physical review letters, 80*(9), 1928.

[123] Prasai, K., Biswas, P., and Drabold, D. A. (2016). Electrons and phonons in amorphous semiconductors. *Semiconductor Science and Technology, 31*(7), 73002-73015.

[124] Bhattarai, B., and Drabold, D. A. (2016). Vibrations in amorphous silica. *Journal of Non-Crystalline Solids, 439*, 6-14.

[125] Nakhmanson, S. M., and Drabold, D. A. (2000). Computer simulation of low-energy excitations in amorphous silicon with voids. *Journal of non-crystalline solids, 266*, 156-160.

[126] Nakhmanson, S. M., and Drabold, D. A. (1998). Approximate ab initio calculation of vibrational properties of hydrogenated amorphous silicon with inner voids. *Physical Review B, 58*(23), 15325.

[127] Kamitakahara, W. A., Soukoulis, C. M., Shanks, H. R., Buchenau, U., and Grest, G. S. (1987). Vibrational spectrum of amorphous silicon: Experiment and computer simulation. *Physical Review B, 36*(12), 6539.

[128] Maradudin, A. A. (1971). *Theory of lattice dynamics in the harmonic approximation* (No. 3). Academic Pr.

[129] Nakhmanson, S. M., and Drabold, D. A. (1998). Approximate ab initio calculation of vibrational properties of hydrogenated amorphous silicon with inner voids. *Physical Review B, 58*(23), 15325.

[130] Zink, B. L., Pietri, R., and Hellman, F. (2006). Thermal conductivity and specific heat of thin-film amorphous silicon. *Physical review letters, 96*(5), 055902.

[131] Khoshman, J. M., and Kordesch, M. E. (2007). Optical constants and band edge of amorphous zinc oxide thin films. *Thin Solid Films, 515*(18), 7393-7399.

[132] Lin, K. H., Sun, S. J., Ju, S. P., Tsai, J. Y., Chen, H. T., and Hsieh, J. Y. (2013). Observation of the amorphous zinc oxide recrystalline process by molecular dynamics simulation. *Journal of applied physics, 113*(7), 073512.

[133] Nomura, K., Ohta, H., Takagi, A., Kamiya, T., Hirano, M., and Hosono, H. (2004). Room-temperature fabrication of transparent flexible thin-film transistors using amorphous oxide semiconductors. *Nature, 432*(7016), 488-492.

[134] Robertson, J. (2008). Physics of amorphous conducting oxides. *Journal of Non-Crystalline Solids, 354*(19), 2791-2795.

[135] Hayamizu, S., Tabata, H., Tanaka, H., and Kawai, T. (1996). Preparation of crystallized zinc oxide films on amorphous glass substrates by pulsed laser deposition. *Journal of applied physics, 80*(2), 787-791.

[136] Bagnall, D. M., Chen, Y. F., Zhu, Z., Yao, T., Koyama, S., Shen, M. Y., and Goto, T. (1997). Optically pumped lasing of ZnO at room temperature. *Applied Physics Letters, 70*(17), 2230-2232.

[137] Xingwen, Z., Yongqiang, L., Ye, L., Yingwei, L., and Yiben, X. (2006). Study on ZnO thin films deposited on solgel grown ZnO buffer by RF magnetron sputtering. *Vacuum, 81*(4), 502-506.

[138] Hosono, H. (2006). Ionic amorphous oxide semiconductors: Material design, carrier transport, and device application. *Journal of Non-Crystalline Solids, 352*(9), 851-858.

[139] Sans, J. A., Sanchez-Royo, J. F., Segura, A., Tobias, G., and Canadell, E. (2009). Chemical effects on the optical band-gap of heavily doped ZnO: M III (M= Al, Ga, In): An investigation by means of photoelectron spectroscopy, optical measurements under pressure, and band structure calculations. *Physical Review B, 79*(19), 195105.

[140] Atta-Fynn, R., Biswas, P., and Drabold, D. A. (2004). Electronphonon coupling is large for localized states. *Physical Review B, 69*(24), 245204.

[141] Stumm, P., and Drabold, D. A. (1997). Can amorphous GaN serve as a useful electronic material?. *Physical review letters, 79*(4), 677.

[142] Heyd, J., Scuseria, G. E., and Ernzerhof, M. (2003). Hybrid functionals based on a screened Coulomb potential. *The Journal of Chemical Physics, 118*(18), 8207-8215.

[143] Aryasetiawan, F., and Gunnarsson, O. (1998). The GW method. *Reports on Progress in Physics, 61*(3), 237.

[144] Schmeiber, D., Haeberle, J., Barquinha, P., Gaspar, D., Pereira, L., Martins, R., and Fortunato, E. (2014). Electronic structure of amorphous ZnO films. *physica status solidi (c), 11*(910), 1476-1480.

[145] Ramo, D. M., Chroneos, A., Rushton, M. J. D., and Bristowe, P. D. (2014). Effect of trivalent dopants on local coordination and electronic structure in crystalline and amorphous ZnO. *Thin Solid Films, 555*, 117-121.

[146] Eguchi, T., Inoue, H., Masuno, A., Kita, K., and Utsuno, F. (2010). Oxygen Close-Packed Structure in Amorphous Indium Zinc Oxide Thin Films. *Inorganic chemistry, 49*(18), 8298-8304.

APPENDIX: A BRIEF DESCRIPTION ON HOW TO USE FEAR

In this appendix, a scheme to use FEAR employing the **RMCProfile** code and a density functional theory code (**VASP** or **SIESTA**) is presented. As described in the algorithm in Chapter 4, FEAR simulation with *ab initio* interactions is carried out in an iterative loop of RMC and *ab initio* calculations. Therefore, the first thing that a user should know is to apply these programs separately.

RMCProfile is freely available software that can be downloaded on : *www.rmcprofile.org*. It is highly recommended to go through the manual and work on the tutorials. One should be careful in choosing a data type to fit (see DATA_TYPE tag in .dat main file of RMCProfile). The various functions (structure data forms) are provided in the section "Using Experimental DATA" of the manual and their implementations are summarized in the section "Implementation with RMCProfile". As an example: for fitting the radial distribution function g(r), the correct data type is *G'(r) normalized* and for the neutrons structure factor S(Q) the data type is *S (Q) normalized*, etc. Recently, fitting EXAFS data has also been introduced in RMCProfile (see manual).

RMCProfile requires three files: *filename.rmc6f*, *filename.dat* and *data.dat*. The .rmc6f is an input coordinate file, *filename.dat* is a main file with all the important tags and input parameters and *data.dat* is an input data file. Likewise, SIESTA requires two files: *filename.fdf* (main file including the coordinates) and *pp.psf* (pseudopotential file). Optionally, coordinates can be put in a separate file *coordinates.dat* which is recommended. VASP requires four files, namely *INCAR, POSCAR, POTCAR and KPOINTS*.

In addition, three driver programs are also essential:

- **mrmc.f90** : This file reads outputs of RMCProfile (*filename.rmc6f* and *out.dat*), mainly the coordinates and chi-square values, etc. The output of this program is the coordinate file for SIESTA/VASP (*coordinates.dat/POSCAR*).
- **msiesta.f90/mvasp.f90** : This file reads outputs of SIESTA/VASP, mainly the coordinates (config_out.dat/CONTCAR) and energies. It gives coordinates file for RMCProfile as an output (*filename.rmc6f*)
- **main.sh** : This shell script is written according to the FEAR algorithm. It contains iterative calls for RMCProfile, reading RMC output (mrmc), SIESTA/VASP and reading the SIESTA/VASP outputs (msiesta/mvasp).

For future application of the method, it might be worthy to use ”SIESTA as a subroutine” (see SIESTA as a subroutine in the manual). This feature enables to call SIESTA as a subroutine in any other program (code) and provides energy and forces which can be utilized for optimizations. This has been applied in FEAR using a different code for RMC.

Tutorials for using DFT codes can be found on the web for both VASP and SIESTA.

Thesis and Dissertation Services